

SANDIA REPORT

SAND2014-18069

Unlimited Release

Printed September 2014

Fundamental studies on initiation and evolution of multi-channel discharges and their application to next generation pulsed power machines

Jens Schwarz, Mark Savage, Joe Woodworth, Diego Lucero, Deanna Jaramillo, Kelly Seals, Todd Pitts, Brenna Hautzenroeder, Mark Laine, David Karelitz, Carsten Thoma, David Rose, Dale Welch, William Zimmermann, Craig Miller, Robert Clark, and John Porter

Prepared by
Sandia National Laboratories
Albuquerque, New Mexico 87185 and Livermore, California 94550

Sandia National Laboratories is a multi-program laboratory managed and operated by Sandia Corporation, a wholly owned subsidiary of Lockheed Martin Corporation, for the U.S. Department of Energys National Nuclear Security Administration under contract DE-AC04-94AL85000.

Approved for public release; further dissemination unlimited.



Sandia National Laboratories

Issued by Sandia National Laboratories, operated for the United States Department of Energy by Sandia Corporation.

NOTICE: This report was prepared as an account of work sponsored by an agency of the United States Government. Neither the United States Government, nor any agency thereof, nor any of their employees, nor any of their contractors, subcontractors, or their employees, make any warranty, express or implied, or assume any legal liability or responsibility for the accuracy, completeness, or usefulness of any information, apparatus, product, or process disclosed, or represent that its use would not infringe privately owned rights. Reference herein to any specific commercial product, process, or service by trade name, trademark, manufacturer, or otherwise, does not necessarily constitute or imply its endorsement, recommendation, or favoring by the United States Government, any agency thereof, or any of their contractors or subcontractors. The views and opinions expressed herein do not necessarily state or reflect those of the United States Government, any agency thereof, or any of their contractors.

Printed in the United States of America. This report has been reproduced directly from the best available copy.

Available to DOE and DOE contractors from
U.S. Department of Energy
Office of Scientific and Technical Information
P.O. Box 62
Oak Ridge, TN 37831

Telephone: (865) 576-8401
Facsimile: (865) 576-5728
E-Mail: reports@adonis.osti.gov
Online ordering: <http://www.osti.gov/bridge>

Available to the public from
U.S. Department of Commerce
National Technical Information Service
5285 Port Royal Rd
Springfield, VA 22161

Telephone: (800) 553-6847
Facsimile: (703) 605-6900
E-Mail: orders@ntis.fedworld.gov
Online ordering: <http://www.ntis.gov/help/ordermethods.asp?loc=7-4-0#online>



Fundamental studies on initiation and evolution of multi-channel discharges and their application to next generation pulsed power machines

Jens Schwarz, Mark Savage, Joe Woodworth, Diego Lucero, Deanna Jaramillo, Kelly Seals, Todd Pitts, Brenna Hautzenroeder, Mark Laine, David Karelitz, Carsten Thoma, David Rose, Dale Welch, William Zimmermann, Craig Miller, Robert Clark, and John Porter

Abstract

Future pulsed power systems may rely on linear transformer driver (LTD) technology. The LTD's will be the building blocks for a driver that can deliver higher current than the Z-Machine. The LTD's would require tens of thousands of low inductance ($< 85\text{nH}$), high voltage (200 kV DC) switches with high reliability and long lifetime ($\gg 10^4$ shots). Sandia's Z-Machine employs 36 megavolt class switches that are laser triggered by a single channel discharge. This is feasible for tens of switches but the high inductance and short switch lifetime associated with the single channel discharge are undesirable for future machines. Thus the fundamental problem is how to lower inductance and losses while increasing switch lifetime and reliability. These goals can be achieved by increasing the number of current-carrying channels. The rail gap switch is ideal for this purpose.

Although those switches have been extensively studied during the past decades, each effort has only characterized a particular switch. There is no comprehensive understanding of the underlying physics that would allow predictive capability for arbitrary switch geometry. We have studied rail gap switches via an extensive suite of advanced diagnostics in synergy with theoretical physics and advanced modeling capability. Design and topology of multichannel switches as they relate to discharge dynamics are investigated. This involves electrically and optically triggered rail gaps, as well as discrete multi-site switch concepts.

Acknowledgment

I would like to thank Briggs Atherton who supported us during the early stages of this LDRD. A very special “Thanks” goes to Dawn Flicker and Gordon Leifeste who kindly offered us their Bldg. 961 lab space when we were desperate for a new temporary “home” for the test stand. A big “Thank you” also to Randy Hickman who fully supported our Bldg. 961 work. This work was funded under LDRD Project Number 158858 and Title “Fundamental Studies on Initiation and Evolution of Multi Channel Discharges and their Application to Next Generation Pulsed Power Machines”.

Contents

Nomenclature	10
1 Introduction	11
2 High Voltage Test Stand	13
2.1 The High Voltage Switch Test Bed Design Requirements	13
2.2 Final Design Implementation	14
3 Rail Gap Switch	19
3.1 Rail Gap Switch Design Requirements	19
3.2 Rail Gap Switch Design Considerations	20
3.3 Diagnostics	24
3.4 Railgap Switch Performance	24
4 Laser Triggered Railgap Switch	37
4.1 Visual plasma plume measurement	38
4.2 Electrical plasma plume measurement	42
4.3 Laser Switch Triggering Design	45
5 Laser Beam Modeling	51
5.1 Introduction	51
5.2 Physical Model	51
5.3 Modeling Codes	53
5.4 Validation	55
5.5 Symbols	63
6 Railgap Switch Modeling	65
6.1 Simulated Circuit Model	65
6.2 2D Simulations of 85% SF ₆ and 15% Ar mixture	69
6.3 Particle Based Chemistry Model for Air	73
6.4 Air Railgap in 2D	76
6.5 Filamentation in 2D/3D Cartesian Switch Tests	86
6.6 Air railgap in 3D	91
6.7 Summary	95
References	97

Figures

1	3D rendering of the final High Voltage Test Stand design.	15
2	The actual High Voltage Test Stand in HighBay 961.	15
3	Charge/dump circuit diagram.	16
4	Conceptual realization of the charge/dump tank.	17
5	Physical realization of the charge/dump tank.	17
6	Control rack for HVTs.	18
7	Cross-sectional view of the railgap switch, including its connection to the capacitors.	20
8	Cross-sectional view of the switch electrode housing with its electric field distribution.	21
9	Some important electric fields inside the switch with 1 cm gap and ± 100 kV applied to the electrodes: on the electrode surfaces, along the housing between the electrodes, and along the housing above the electrodes.	22
10	Overall switch inductance as a function of number of discharge channels.	23
11	Low inductance railgap switch developed by this LDRD project.	25
12	Top-down view of the inside of the switch housing.	25
13	Multi-channel arc discharge for a 1.5 cm gap at 40 psi and ± 48 kV.	26
14	Multi-channel arc discharge for a 1.5 cm gap at 180 psi and ± 90 kV.	27
15	(a) Side-on image of trigger and switch electrodes prior to the arc discharge. (b) Time integrated image of the multi-channel arc discharge (same field of view as in a)	28
16	Plot of average visually observed discharge channel count versus self-breakdown voltage.	29
17	Plot of average visually observed discharge channel count versus gap separation. ...	30
18	Load current vs. time for 180 kV switch voltage, $2\ \Omega$ total resistance, 40 nF capacitance, and 85 nH inductance. The black curve shows the measured current and the red curve depicts the calculated current based on a circuit model using fixed component values. No amplitude adjustment was applied for this shot.	31
19	Typical waveform for load current and trigger pulse for 180 kV DC on the switch and an electrode gap of 1.5 cm.	31
20	Switch runtime versus percent of self-breakdown voltage with an electrode gap of 1.5 cm. As expected, the graph shows that the switch runtime should approach infinity at low fractions of self-breakdown, and approach zero at 100% self-breakdown.	32
21	Load current versus the number of discharge channels for 180 kV (black), 145 kV (green), and 96 kV (red) DC voltage on the switch.	32
22	Typical arc-discharge emission spectrum of dry air at 120 psi at a switch voltage of 168 kV DC.	33
23	Arc discharge spectrum in dry air at 96 kV DC for various switch pressures.	34
24	Arc discharge spectrum in dry air at 200 psi for two different switch voltages.	34
25	Stainless steel switch electrodes and trigger bar after about 50 shots.	35

26	1:4 large core fiber splitter based on 100 individual 100 μm core fibers that are fused in silica at the input and output face. The ns laser pulse is launched into the fused fiber end of a high power Amphenol SMA connector (A) after which it is transported close to the rail gap switch. At that point, the beam is split four ways and the outputs are focused into the HV switch. Drawing courtesy of CeramOptec Industries Inc.	39
27	Near field image of de-magnified fiber output for: (a) a straight through 1 mm diameter fused silica core fiber, (b) a single 1:4 split fiber line, showing the 25 fibers fused in silica surface, (c) end-face of the individual 100 μm diameter fiber just before they are fused in silica.	40
28	Time integrated plasma plume created by laser light impinging on a titanium target irradiated by 17 mJ of laser light from a straight through fiber focused to a spot size of 560 μm diameter. The resulting nearly hemispherical plasma plume has a diameter of 2.6 mm and a radius of 1.0 mm.	41
29	Visual extent of plasma plume radius (a) and diameter (b) versus fiber output energy for a de-magnified spot size of 560 μm out of a 1 mm solid fused silica fiber. Note that no substantial plasma plume could be detected for the graphite material. .	42
30	Comparison of plasma plume size between a large solid core fiber and a single 1:4 split beam. The beam shape on target corresponds to the near fields depicted in Fig. 27(a) and Fig. 27(b-c) respectively.	43
31	Apparatus used to measure the capacitance change directly by recording the voltage change due to the laser beam striking one electrode of a biased capacitor. As the laser strikes the target electrode, a plasma is created, the capacitance of the system changes, and the corresponding voltage change is recorded on a digitizer. (a) shows the capacitor setup in detail and (b) depicts the corresponding circuit diagram used to measure the displacement current. The target disc is 25 mm in diameter and the separation between the electrodes can be varied between 5 and 10 mm. A +50 V bias voltage is applied to the electrode facing the incoming beam whereas the target electrode is held at ground potential.	44
32	(a) Normalized laser temporal diode trace with respect to derivative of capacitance change. (b) Change in capacitance versus time.	45
33	10%-90% temporal rise time of the probe voltage for a single 1:4 fiber splitter line versus laser energy and target material.	46
34	Calculated and visually measured plasma plume radius/diameter versus laser intensity/energy for two different beam intensity ranges corresponding to focal spot diameters of (a) 240 μm and (b) 470 μm	47
35	Cross-sectional view of the switch housing with the electric field distribution. A 25 mm diameter asphere is placed 25 mm away from the switch electrode at a laser incident angle of 55°.	48
36	Image de-magnification (black) and object distance (red) as a function of focal distance.	49
37	Initial design for the laser triggering concept. The electrical trigger bar has been replaced by a lens focusing bar.	50
38	Detailed view of the laser triggering concept.	50
39	Diffraction and Dispersion Lengths	56

40	Critical Power	57
41	Ionization	58
42	Ionization	59
43	Raman and Shock	60
44	Raman	61
45	Raman	62
46	Simplified circuit model for railgap simulations. The grid connection to the anode and cathode are shown on the top and bottom, respectively. The positions of the grid connections are shown in Fig. 47.	66
47	Connection of circuits to simulation domain. Purple box denotes area of conducting volume model used for the simulation results shown in Fig. 50. The thick black arrows show the current path when the switch is closed.	66
48	The trigger circuit used for railgap simulations. The positions of the grid connections are shown in Fig. 47.	67
49	Voltages on the anode V_{AG} , cathode V_{KG} , and trigger V_{TG} (all with respect to ground) for the open-circuited railgap.	68
50	Discharge of capacitor by $1/12\ \Omega$ resistor placed between cathode and anode in 2D Cartesian railgap simulation.	68
51	Normalized effective ionization coefficient for 85% SF_6 and 15% Ar mixture obtained from swarm simulations.	69
52	History plots for a 2D railgap simulation with 85% SF_6 and 15% Ar mixture.	70
53	2D railgap simulation for SF_6/Ar mixture. Electron density contours. Avalanche and early streamer propagation.	71
54	2D railgap simulation for SF_6/Ar mixture. Electron density contours. Streamer propagation and connection from trigger to anode.	71
55	2D railgap simulation for SF_6/Ar mixture. Electron density contours. Evolution of current channel.	71
56	2D railgap simulation for SF_6/Ar mixture. Electron density and current amplitude contours illustrate the time evolution of the current channel.	72
57	Electron-impact cross-sections for O_2 [1].	74
58	Results from LSP electron swarm simulation in air.	75
59	Electron drift velocity and normalized ionization rate as a function of E/n_n . for electron swarms in air. LSP results are compared to experimental data.	75
60	Normalized ionization rate for dry air as a function of n_n , for a fixed electric field of 125 kV/cm. Some variation with timestep is exhibited in the results.	77
61	Electron density contours from initial 2D air railgap simulation. Note formation of spurious streamer from right hand side of cathode. This streamer was seeded by a numerical field enhancement due to a stair-stepped conducting boundary.	78
62	History plots for initial 2D air railgap simulation.	79
63	Slight modification of cathode geometry to avoid spurious streamer propagation from stair-stepped conducting corners. The anode shape is unaltered.	80
64	Restriction of ionization volume in modified railgap geometry for air.	80
65	Snapshots of electron density 2D Air streamer simulation results. A streamer propagates from the trigger to the anode.	81

66	Snapshots of electron density for 2D Air streamer simulation. A streamer propagates from the cathode to the trigger to form a full current path from A to K.	82
67	2D-rz cylindrical switch simulation using pure N_2 at 1/2 atm. Snapshots of electron density contours.	83
68	Driving circuit for cylindrical switch simulation. $Z_{grid} = 17.25 \Omega$, and $Z_0 = R_0 = 0.5 \Omega$ and $V_{in} = 3.125$ kV.	84
69	History plots of voltage, current, resistance, and rms radius for 2D-rz switch test. .	85
70	Snapshots of electron density contours for 2D Cartesian switch test with pure N_2 at 1 atm.	86
71	Driving circuit attached to both the left and right input ports of the simulation space shown in Fig. 70. $Z_{grid} = 732 \Omega$, and $Z_0 = R_0 = 5 \Omega$	86
72	History plots of voltage, current, resistance, and total electron charge for 2D Cartesian switch test with pure N_2 at 1 atm.	87
73	Initial electron density iso-contour of 10^{14} cm^{-3} for 3D Cartesian switch test in pure N_2 at 1 atm.	88
74	History plots of voltage, current, resistance, and total electron charge for 2D (black) and 3D (red) Cartesian switch test with pure N_2 at 1 atm.	89
75	Electron density contours in the midplane of the switch for the 3D Cartesian simulation. The development of ≈ 1 mm wide filamentary structures along the cathode surface is observed.	90
76	Geometry for full railgap switch field calculation.	91
77	Vector plots of electric field from 3D railgap field solution in the xy plane at several fixed z positions. The color map shows the field magnitude in kV/cm.	92
78	Vector plot of electric field from 3D railgap field solution in $x = 0$ plane. Some field enhancement is evident at the end of the railgap. Note: $z = 0$ is a symmetry plane. The color map shows the field magnitude in kV/cm.	93
79	Electron density iso-contour ($n_e = 2.2 \times 10^{14} \text{ cm}^{-3}$) of 3D railgap simulation at $t = 16.2$ ns.	94
80	Electron density contours ($t = 21$ ns) along the rails show filamentary structure. . .	94

Tables

1	Emission spectrum from an arc discharge in dry air at 120 psi and 168 kV DC voltage. 33
---	---

Nomenclature

AK anode cathode

atm standard atmosphere (101325 Pa)

CCD charged coupled device

DC direct current

HV high voltage

HVST high voltage test stand

ICF Inertial Confinement Fusion

LSP Large Scale Plasma

LTD Linear Transformer Driver

PIC Particle In Cell

psi pounds per square inch

STP standard temperature and pressure

UV ultraviolet

1 Introduction

Future pulsed power systems may rely on linear transformer driver (LTD) [2, 3] technology. These LTDs convert energy stored in DC-charged capacitors directly into ≈ 100 ns voltage pulses, thus eliminating the multiple stages for pulse compression used in the Z system. The 100 ns pulses are then inductively added to produce the desired currents and voltages at the load. The basic LTD “brick” architecture consists of two capacitors. Each is charged with opposite polarities with a triggered switch between them. In order to generate short pulses with high peak currents the “brick” must have as low an inductance as possible. The total inductance in most present LTD systems is dominated by the relatively high inductance of the high voltage switch. . The present state of the art switching technology for these systems is high-pressure gas spark gaps. Solid-state switches are not viable at this time because of the high voltage DC hold-off required, and because of the high current rise rate impressed on each switch (≈ 2 kA/ns) that exceeds the capabilities of presently available devices.

It is desirable to improve the spark gap switching technology as much as is practical. The fundamental problem is how to lower inductance and increase switch lifetime for these systems. These goals can be achieved by increasing the number of current-carrying channels. It may be desirable to replace the more common cylindrical gas switches with rectangular rail electrode switches. These switches may reduce the switch inductance by a factor of 4 or more. Rail gap switches have been used for other applications [4, 5, 6, 7], but have never been proposed or used for any LTD systems. Since the capacitor connections are an inherently rectangular geometry, maintaining the rectangular geometry in the gas switch allows a large decrease in overall system inductance, with the added benefit of exploiting the natural LTD geometry. Straight rod electrodes have the disadvantage of possible field enhancements at the ends of the electrodes and are generally more complicated to fabricate and assemble. However, the rail gap switch has the possibility of multiple breakdown discharges across the gap, lowering the inductance and increasing switch lifetime. These rail switches can be triggered electrically by placing a HV pulsed knife edge electrode near one of the switch electrodes [8, 9] or via a UV pre-ionized channel that runs closely along one of the electrodes [5, 6, 7].

While multichannel spark gap switches are of considerable interest, it should be noted that in general, spark gap behavior does not favor multiple parallel channels without some form of isolation [10]. While multiple streamers may exist during triggering, current tends to coalesce into a single channel. Channels carrying less current eventually decay away. Operation with multiple channels requires rapid formation and initial heating of many channels with a large and fast trigger pulse. In addition, a system with low impedance is necessary so that considerable voltage would exist across the switch if only a single channel closed. A major part of this study was understanding the effectiveness of initiating and maintaining multiple channels within a single switch.

Although rail gap switches have been extensively studied during the past decades each effort has only characterized a particular switch. There is no comprehensive understanding of the underlying physics that would allow predictive capability for arbitrary switch geometry. Hence, we have pursued a synergy between experiment and theory to gain a basic understanding of the underlying discharge dynamics in rail gap triggered switches.

2 High Voltage Test Stand

In order to study multi-channel switching characteristics in a rail gap configuration, we have designed and operated a Switch Test-Bed, which is a portable high-voltage test facility designed primarily for testing high voltage (HV) rail gap switches that may be used in future LTDs. During operation of the rail switch (or any other suitable switch), series capacitor pairs of up to 160 nF are charged to voltages of up to ± 100 kV for a total 200 kV voltage across the rail switch. The capacitor energy is then discharged by the rail gap switch into a liquid resistive load, generating peak currents of up to ≈ 70 kA in ≈ 130 ns FWHM pulses. The region between the rail switch electrodes is insulated with up to 250 psi of an insulating gas such as dry air, Sulfur Hexafluoride (SF_6), or a mixture of SF_6 and Argon. We have used dry air for our studies.

2.1 The High Voltage Switch Test Bed Design Requirements

The high voltage test bed was designed to run fully automated and stand alone and be able to accept a wide range of specifications. In our case, the system was geared toward the following requirements.

Electrical Requirements

- Use off the shelf components to the extent possible
- Provide a low inductance (≈ 50 nH) capacitive store for kJ energy
- Provide accurate measurements of total system current and current distribution
- Provide accurate measurement of switch voltage after closure
- Accommodate a low inductance switch (≤ 50 nH)
- Provide 200 kV DC voltage at a repetition rate of up to 0.2 Hz
- Have a recirculating resistive matched load at 160 W average, 100 kV and up to 50 kA peak current
- Provide fast-rising (10 ns) electrical trigger pulses up to 250 kV in peak amplitude
- Switch jitter ≤ 10 ns

Mechanical Requirements

- Fully enclosed high voltage
- Automated oil processing and filtering system

- Complete secondary containment
- Easy maintenance, i.e. easy access to all HV components in oil tank
- Self-contained and mobile, i.e. no requirement for cranes or hoists for routine maintenance

Diagnostic Requirements

- Full electrical diagnostic suite: flux loops to measure current, displacement current monitors to measure voltage, etc.
- Electrical diagnostics must be adequate and accurate to allow evaluation of each test by numerical routines to detect failures or changes in behavior- 1% changes in signals are easily detectable with eight-bit digitizers
- Switch needs to be located in ambient air to allow for:
 - Easy access to switch in order to change configuration, i.e. electrode material, shape, length, and separation
 - Optical diagnostics, i.e. CCD camera, streak camera, optical schlieren or interferometry probe beams
 - Easy access for external free space laser (or fiber) switch triggering
- In case no diagnostic access is needed, the switch can be located *inside* the oil tank

Machine and Personnel Safety

- Positive locking on lift columns: Protects user while working on dump tank components
- Fail safe design: Disables hazard sources (e.g. HV or high pressure) and puts machine into safe mode in case of unforeseen power outage
- Continuous monitoring of system state: Assures safe and even unattended operation
- Handrails and removable steps

2.2 Final Design Implementation

Figures 1 and 2 show how the above design requirements were realized in the actual system. Some of the notable features are: the tank sight glasses that allow for easy visual checks of oil tank components, the air-bearing system that allows the system to float to any location, the single electrical disconnect switch, and the reconfigurable diagnostic ports.

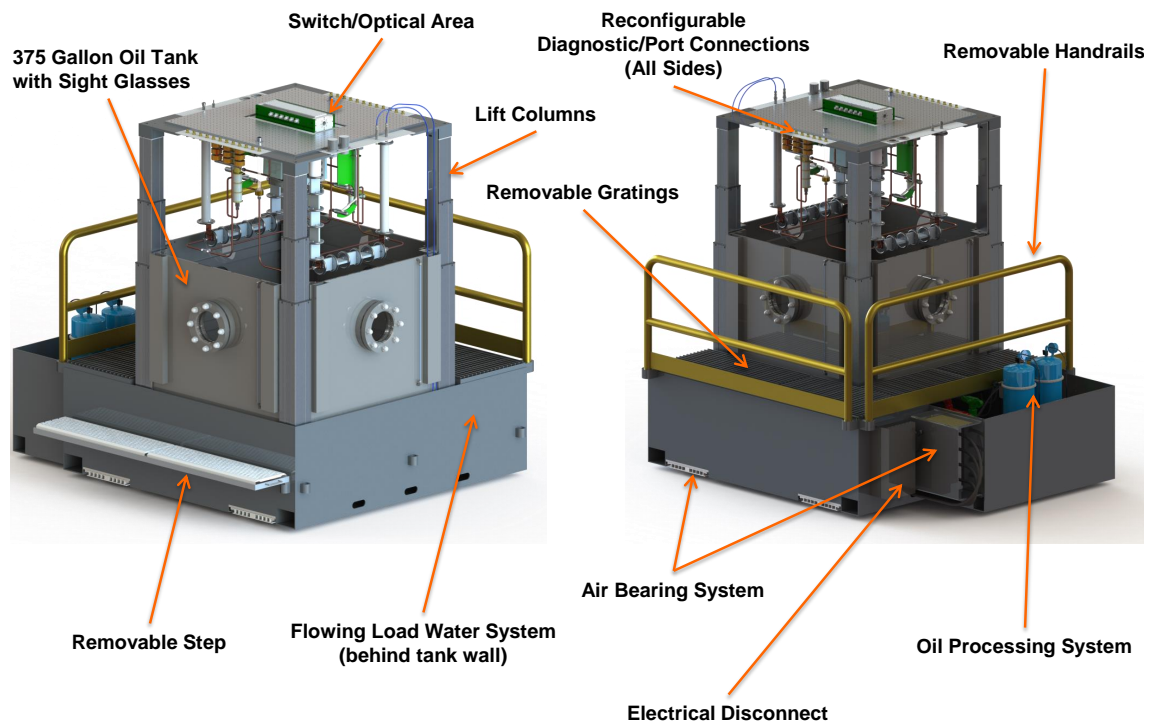


Figure 1. 3D rendering of the final High Voltage Test Stand design.



Figure 2. The actual High Voltage Test Stand in HighBay 961.

Charge/dump Tank

Figure 3 depicts the circuit diagram of the charge/dump system. It is designed to charge up to ± 100 kV DC in 1.5 s and contains active/passive filtering as well as voltage reversal and over-voltage protection.

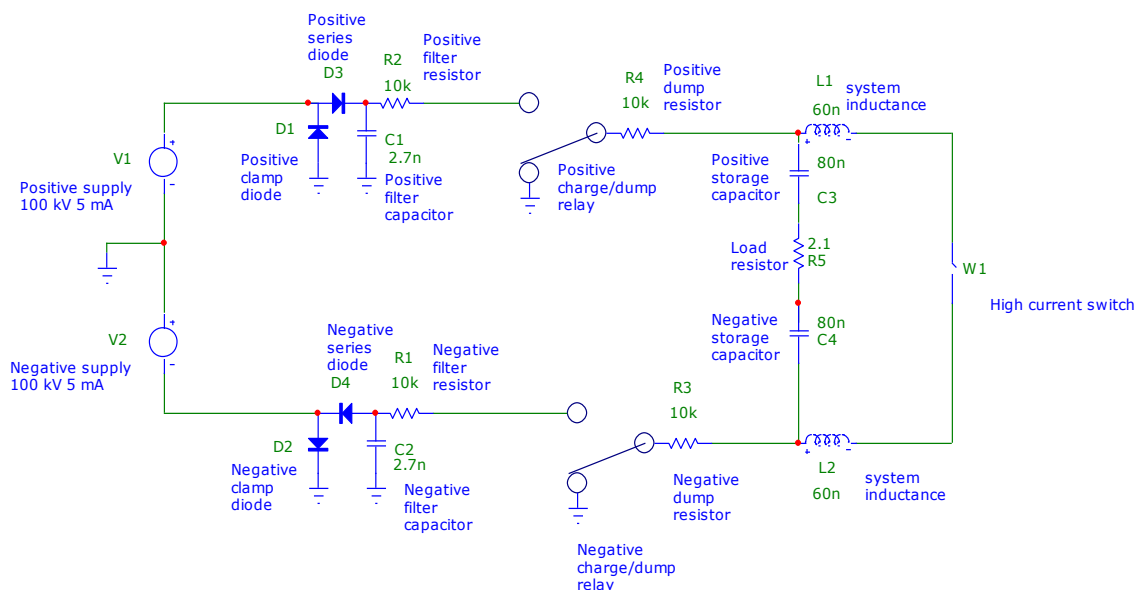


Figure 3. Charge/dump circuit diagram.

Figures 4 and 5 show the actual physical components used. Note that all connections are rigid large diameter copper tubing with plenty of stand-off distance between high voltage components.

The Oil Processing System

The transformer oil-processing system is fully integrated into the high voltage test stand. It maintains a $0.3 \mu\text{m}$ filtration level by using a modular filter design with convenient bypass capability. In addition, the unit is equipped with a built in “bubbler” to handle dehydration of free water as well as dissolved water. In preparation for transport of the test stand, the system is also capable of handling oil transfer to and from external storage barrels.

System Control Infrastructure

Figure 6 depicts the HVTS system control rack. The top unit controls charge/dump relays as well as oil flow and other components. The mid section houses the two 100 kV DC power supplies and the bottom unit contains a custom gas handling system. The system hardware was designed

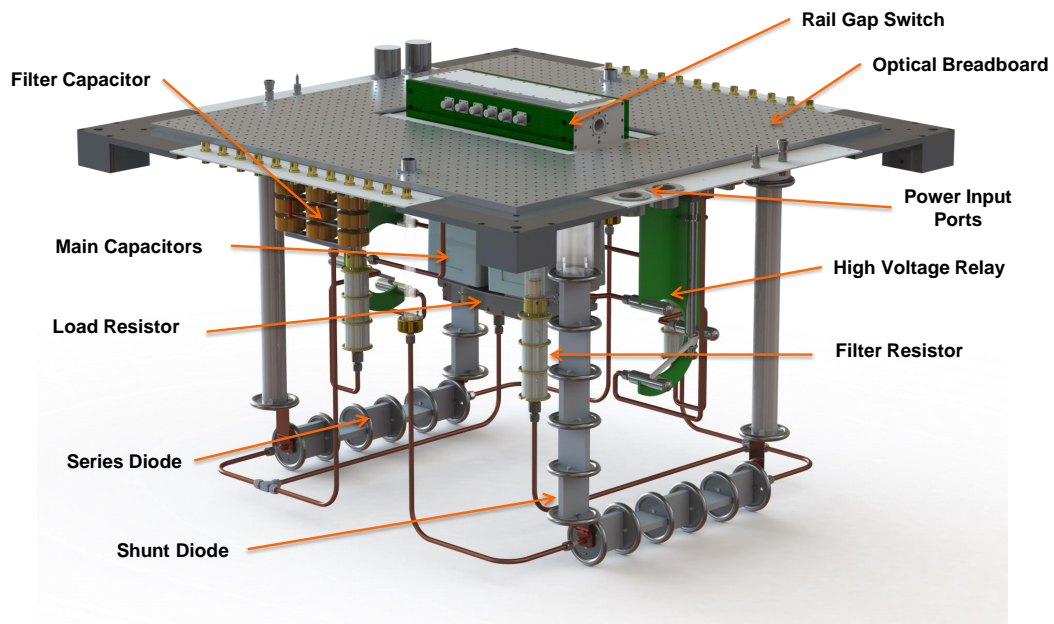


Figure 4. Conceptual realization of the charge/dump tank.

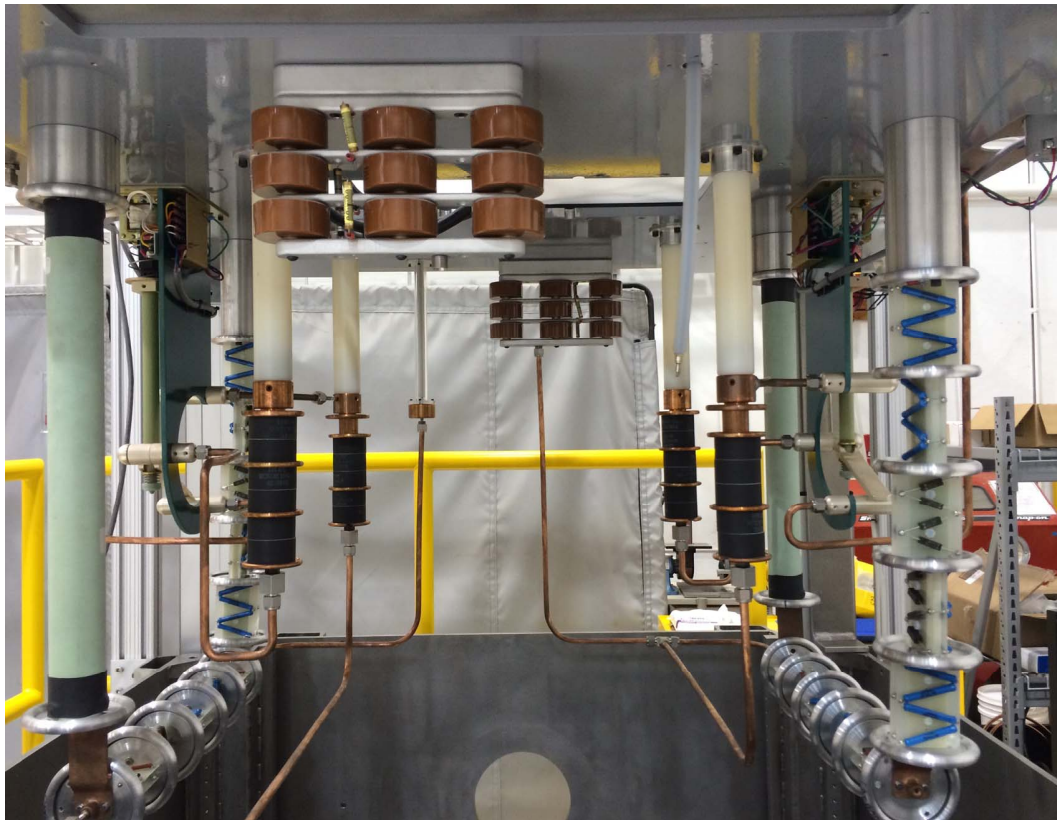


Figure 5. Physical realization of the charge/dump tank.

from the ground up to allow for fully automated and autonomous operation. However, due to some software shortcomings, the system is currently operated in manual mode.



Figure 6. Control rack for HVTS.

3 Rail Gap Switch

3.1 Rail Gap Switch Design Requirements

Electrical Requirements

- Multi-channel switching (≥ 4 channels)
- Long switch lifetime ($\gg 10^4$ shots)
- Fast temporal rise-time, i.e. low inductance ($< 50\text{nH}$)
- Low switch jitter ($< 10\text{ ns}$)
- Operate at $\pm 100\text{ kV}$ with $> 50\text{ kA}$ peak current
- Electrical and laser triggering capable
- Interchangeable electrodes, including variable electrode spacing

Mechanical and Diagnostic Requirements

- Capable of 250 psi pressure loading
- Non conductive material
- Flowing resistive load
- Full electric diagnostic capability, i.e. voltage, current, and B-dot probes
- Integrate with standard General Atomics capacitors
- In-air placement to allow for optical diagnostics and focal tube

3.2 Rail Gap Switch Design Considerations

We have designed the rail switch in this test-bed to optimize our ability to study the physics of rail switching. Hence our switch is designed with much more flexibility and better optical access than a typical “point-design” switch in a real LTD system. Figures 7 and 8 show two cross-sectional

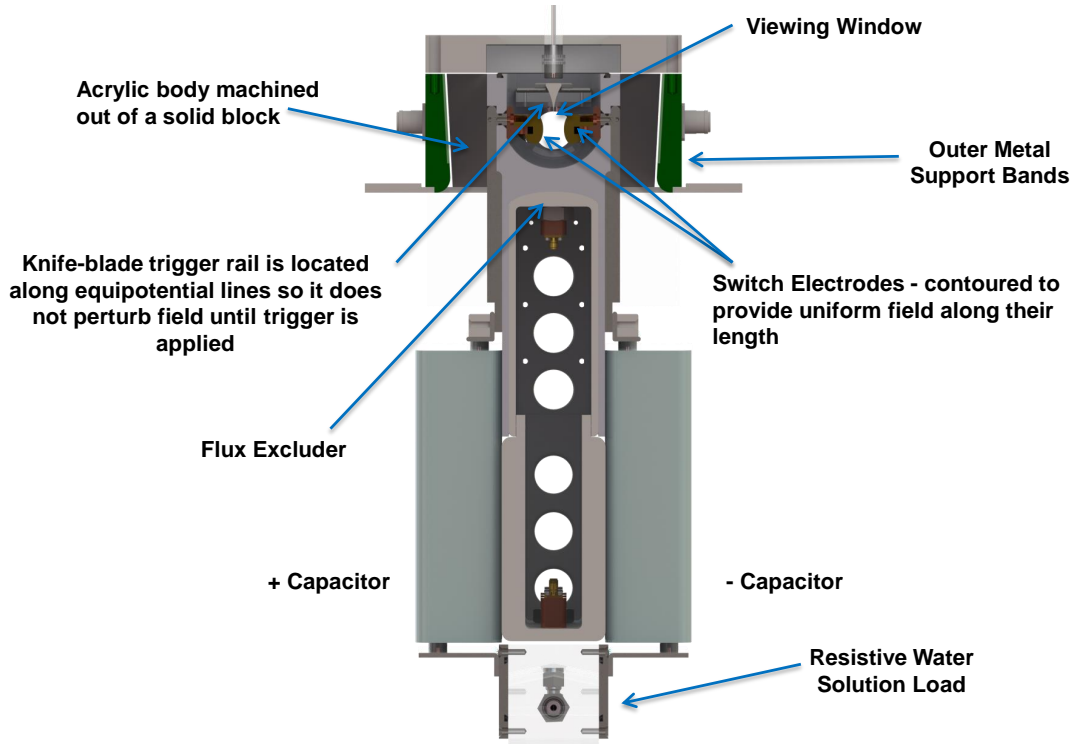


Figure 7. Cross-sectional view of the railgap switch, including its connection to the capacitors.

views of our switch. The switch housing is about 40 cm long and can contain electrodes that are up to 24 cm long. The electrode spacing can be varied from 0.0 cm to 2.0 cm. Since the electrodes are removable, electrodes of different shapes and lengths can be tested. Figure 8 shows the electrical field distribution between the electrodes as well as the trigger electrode mounted above. This trigger electrode is longer than the main electrodes in order to produce the most uniform field geometry. This trigger bar will normally be located 1/3 the-way between the two main electrodes and biased at an intermediate voltage that does not distort the E-fields between the main electrodes. During operation, the trigger electrode will be pulsed negative/positive by a 300 kV pulse from a micro-Marx with a 1.8 ns rise-time.

The gas inlet and outlet port are at opposite ends of the switch next to the end window. The insulating parts of the switch housing are made of Lucite™ acrylic since Lucite has shown better resistance against surface tracking than polycarbonate in previous experiments.

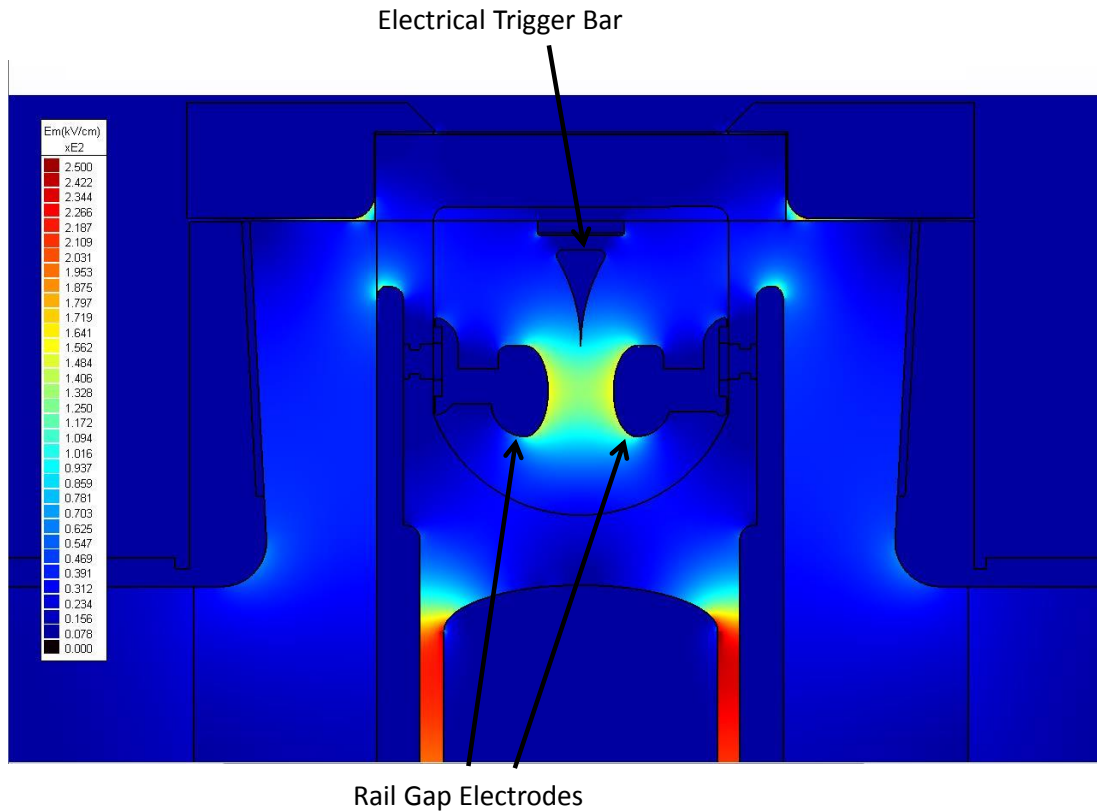


Figure 8. Cross-sectional view of the switch electrode housing with its electric field distribution.

As mentioned above, both the switch end windows and top window are directly exposed to laboratory air for best diagnostic access. In order to prevent high voltage breakdowns, all the high-voltage hardware on the exterior of the switch has been vacuum-impregnated in epoxy from the top of the switch down to a level below the oil level in the charge/dump tank. The outer epoxy-encapsulated surfaces of the switch are further wrapped in a grounded metal case to assure personnel safety while the switch is in use.

In an LTD system, the capacitors would be located close together and as close as possible to the switch, in order to minimize overall system inductance. We have inserted a flux excluder between the “plus” and “minus” current busses and between the capacitors to allow us to keep overall system inductance low while at the same time separating the capacitors from the switch. Switch reliability in general is strongly affected by the electric field along the solid interior surfaces of the switch. Flashover along the insulator surface behaves like a switch closure, but typically permanently damages the switch housing surface. We have paid careful attention therefore, to the surface electric fields in this switch. Figure 9 shows a plot of E-field along the lower surface of the switch, from one electrode to the other. Both the insulator and electrode surfaces have been designed to keep the fields as smooth as possible along this critical surface and below 10 kV/cm when the voltage between the switch electrodes is 200 kV. Uniform fields along the length of the switch electrodes are also important for achieving multi-channeling in rail switches. Figure 9 also

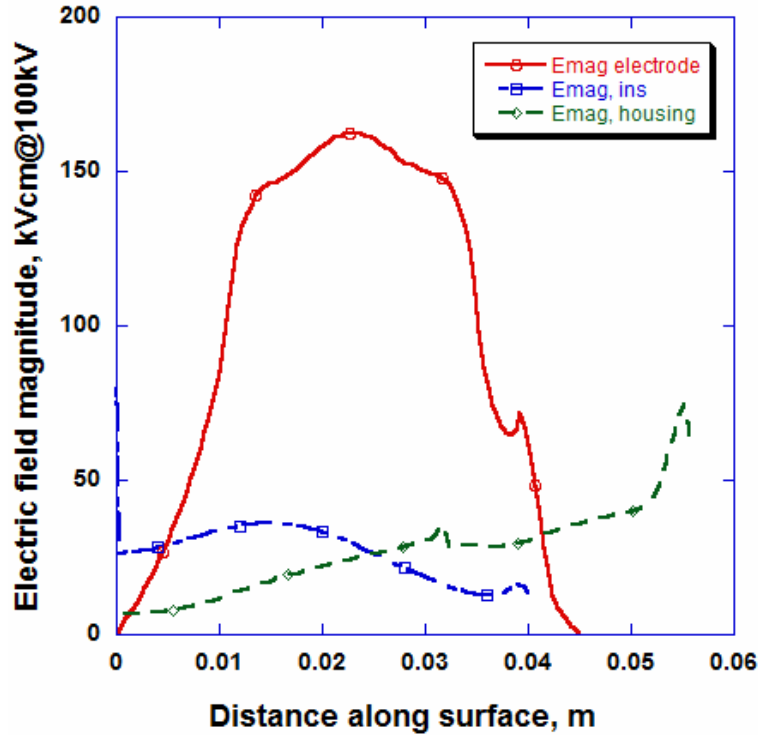


Figure 9. Some important electric fields inside the switch with 1 cm gap and ± 100 kV applied to the electrodes: on the electrode surfaces, along the housing between the electrodes, and along the housing above the electrodes

shows a plot of electric field between the switch electrodes from one end of the switch to another.

In a large LTD Inertial Confinement Fusion (ICF) accelerator, each LTD “brick” will probably consist of a switch and two 80 nF capacitors, with the capacitors charged to ± 100 kV. Two sets of parallel 40 nF capacitors were used to reduce the system inductance, making the switch inductance more readily calculated, and reduce the current in each capacitor. In this system two 40 nF capacitors in parallel are charged to +100 kV and two more on the other side of the switch are charged to -100 kV. Each of these “double-ended caps” has one terminal at each end allowing lower inductance system design. A flowing resistive load at the bottom of the capacitors completes the circuit and dissipates the power pulse developed when the switch fires.

This rail switch can only achieve a ≤ 50 nH overall inductance if the switch shares current over multiple arc channels. Figure 10 shows the switch inductance, composed of both loop inductance and arc channel inductance, as a function of the number of arc channels in the switch. About 4 arc channels are enough to lower the switch inductance to ≤ 50 nH.

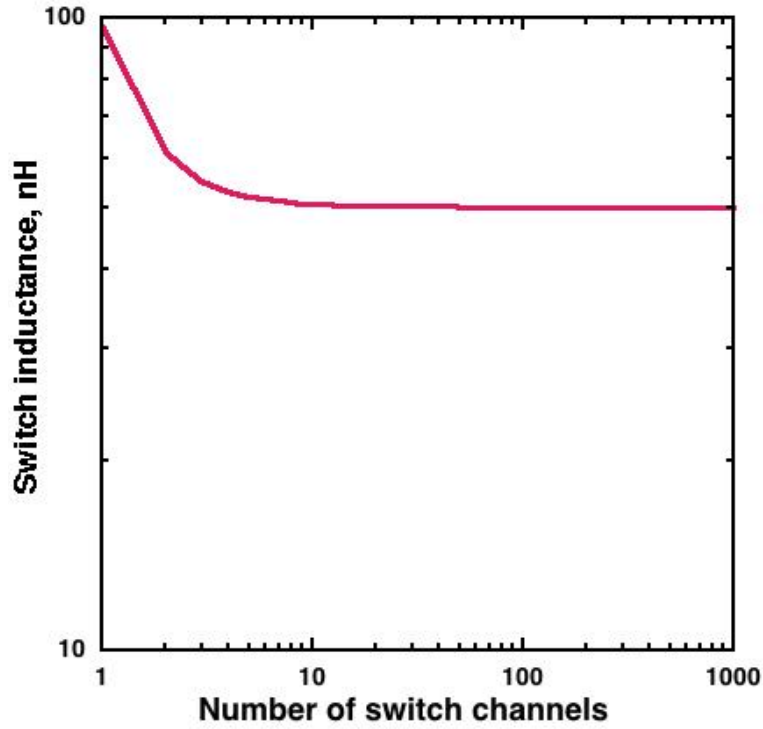


Figure 10. Overall switch inductance as a function of number of discharge channels.

Switch Inductance

The total inductance of the system depends upon the number of switch channels carrying current and their spatial distribution. Even multiple channels, if close together, will not allow significant inductance reductions compared to single channel operation. The full width of the switch electrodes is 24.79 cm. With completely uniform current flow, the inductance of the switch itself would be 15.9 nH, the switch feedlines would be 8.5 nH, and the load inductance would be 10.6 nH. This gives a total of 35 nH. The four capacitor (two series, two parallel) energy storage configuration gives the same capacitor inductance as a single unit. Measuring inductance of these capacitors is not trivial, and results vary. It is felt that 25 nH is a reasonable estimate for this capacitor. This gives a total inductance of 60 nH. The deficit is 25 nH compared to the inductance computed by fitting the measured current to a circuit simulation (85 nH), concentrating on the initial part of the current rise, when inductance is most important. Most of this excess inductance likely comes from discrete channels and non-uniform current flow.

3.3 Diagnostics

Electrical Diagnostics

Arrays of B-dot and V-dot monitors are used to make current and voltage measurements on the rail switch. One array of B-dots is located in the top of the flux excluder and looks at current between the switch electrodes. The array of six monitors allows us to look for current asymmetries due to changes in arc locations from shot to shot. A second array of B-dots, located at the bottom of the flux excluder measure current in the resistive load. An array of 6 V-dots is located on each side of the switch. These allow us to measure voltage on the electrodes during the breakdown of the switch. These voltage measurements, coupled with switch current measurements, allow us to calculate switch impedance during the switch breakdown process. All of these diagnostics are calibrated in situ by applying a known current and voltage pulse between the switch electrodes and observing the response compared to known reference standards at more manageable voltages and currents (≈ 6 kV and 5 kA).

Optical Diagnostics

In addition to a still camera for taking time-integrated photos of the spark channels, one can also use both a streak and a framing camera to study the switch. The discharge channels can be observed through the top lid or side-on through the windows on the end-plate. The side window also allows for time integrated visual spectrum measurements.

3.4 Railgap Switch Performance

Figure 11 depicts the actual as built switch as used in our experiments. One can clearly see the side diagnostic window with the gas flow lines attached. This window is removable and can be exchanged for a long laser focal tube for creating a homogeneous ionized plasma channel along the switch electrodes via a short pulse laser. Along the side of the switch one can see the electrical diagnostic ports. Two posts on top of the lid make the electrical connection from the trigger generator to the trigger electrode inside the switch. The switch lid is transparent in order to allow for optical diagnostics. Figure 12 shows a top-down view of the inside of the railgap switch housing. One can see the removable electrodes on the top and bottom and the trigger bar in the center between the electrodes. Note that the trigger bar and electrode mountings are slotted so that their position can be varied as needed.

Experiments were performed in dry air as an insulating gas at charge voltages of ± 48 kV to ± 90 kV at pressures ranging from 40 psi to 220 psi and gap separations of 1-2 cm.

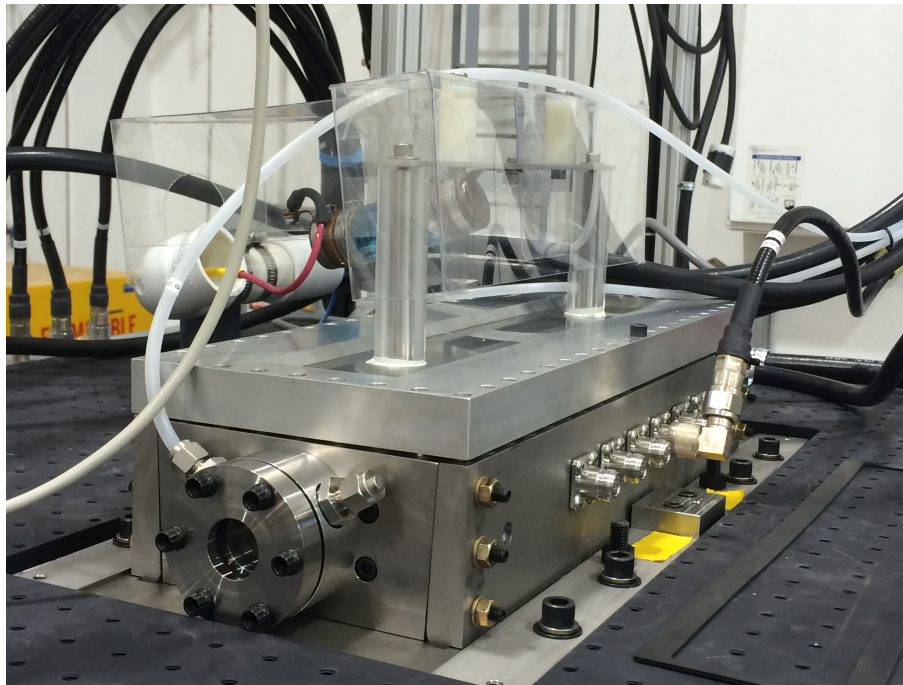


Figure 11. Low inductance railgap switch developed by this LDRD project.

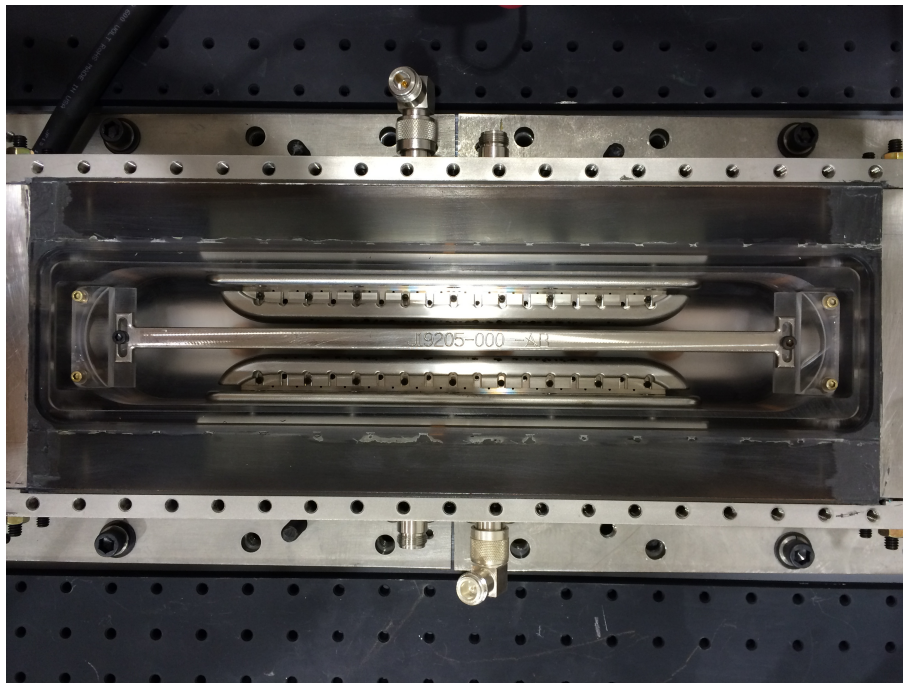


Figure 12. Top-down view of the inside of the switch housing.

Optical Diagnostics

Figures 13 and 14 show some representative multi-channel discharges for a 1.5 cm gap separation and ± 48 kV and ± 90 kV switch voltages. Overall, we took more than 260 shots and almost all shots show more than three discharge channels which is sufficient for low inductance operation (see Fig. 10).

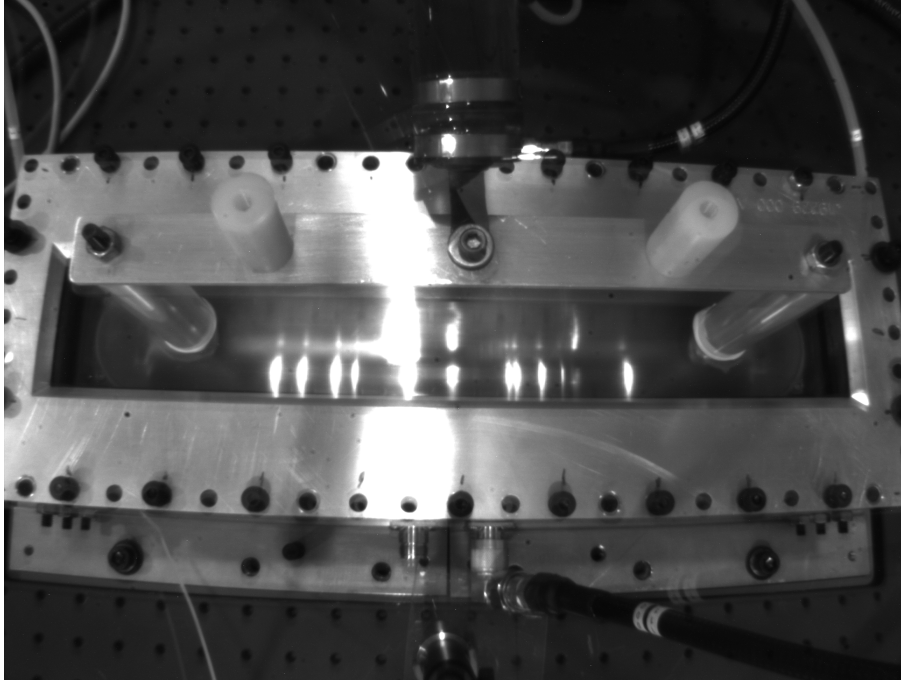


Figure 13. Multi-channel arc discharge for a 1.5 cm gap at 40 psi and ± 48 kV.

Figure 15 depicts an arc channel discharge as observed by the optical side-on diagnostic. As the trigger electrode charges to -300 kV in 2 ns the air breaks down between the trigger electrode and the positive electrode first. Once those channels are formed, the trigger bar has the same potential as the positive electrode and subsequently breaks down the gas going toward the negative electrode. Note that there is no direct discharge channel between the two electrodes. This discharge dynamic was also corroborated by our numerical modeling (see section 6).

Figure 16 shows the average number of visually observed discharge channels versus percent of self-breakdown for a 1.5 cm electrode separation. As expected, one can see that the number of discharge channels increases as one approaches 100% of the self-breakdown voltage. Figure 17 depicts the average number of visually observed discharge channels versus electrode gap separation. Again, the switch behaves as expected, showing a significant increase in channel count toward smaller gap separations. Most of our shots were performed at a gap separation of 1.5 cm for the following reasons: 1) At 1 cm gap separation the required gas pressure would be higher than desired for the highest applied voltages. 2) At 2 cm separation the channel count was occasion-

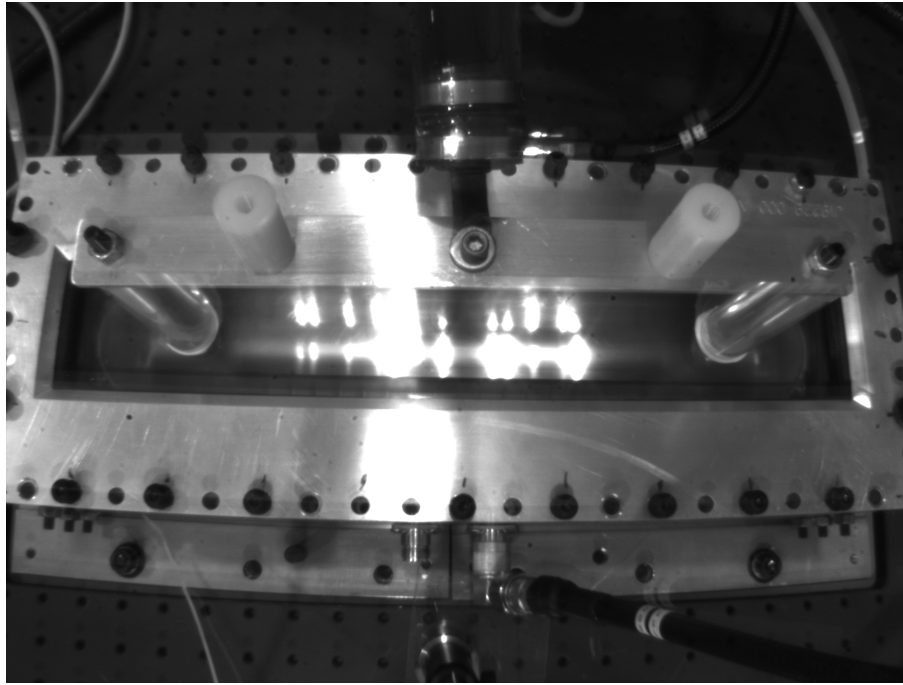


Figure 14. Multi-channel arc discharge for a 1.5 cm gap at 180 psi and ± 90 kV.

ally marginal and the likelihood increases that the switch may discharge along the switch housing rather than through the gas. Furthermore, the average number of six discharge channels at 1.5 cm separation seems to be an ideal number for optimal load current (see below).

Electrical Diagnostics

Figure 18 depicts the load current as a function of time for 180 kV switch voltage, $2\ \Omega$ load resistance, 40 nF capacitance, and 85 nH inductance. One can see that there is a good match between the observed data and the predictions based on the static circuit model. The 10% - 90% current rise time is 39 ns, consistent with an overall system inductance of 85 nH. This is the combined “brick” inductance and includes the switch and the remaining circuitry. This constitutes the lowest “brick” inductance ever measured for such a system.

Figure 19 shows a typical waveform for load current and trigger pulse for 180 kV DC on the switch and an electrode gap of 1.5 cm. One can see that the load current starts rising within 20 ns of the trigger pulse. This time delay is called “switch runtime” and corresponds to the time it takes for the arc discharge to fully form before the switch closes and full current can be conducted. Note that the trigger open circuit voltage is 300 kV with a rise-time of 1.8 ns. This very powerful trigger pulse is the reason why we consistently observe multi-channeling on every single shot.

Switch runtime versus percent of self-breakdown voltage is shown in Fig. 20 for 96 kV DC

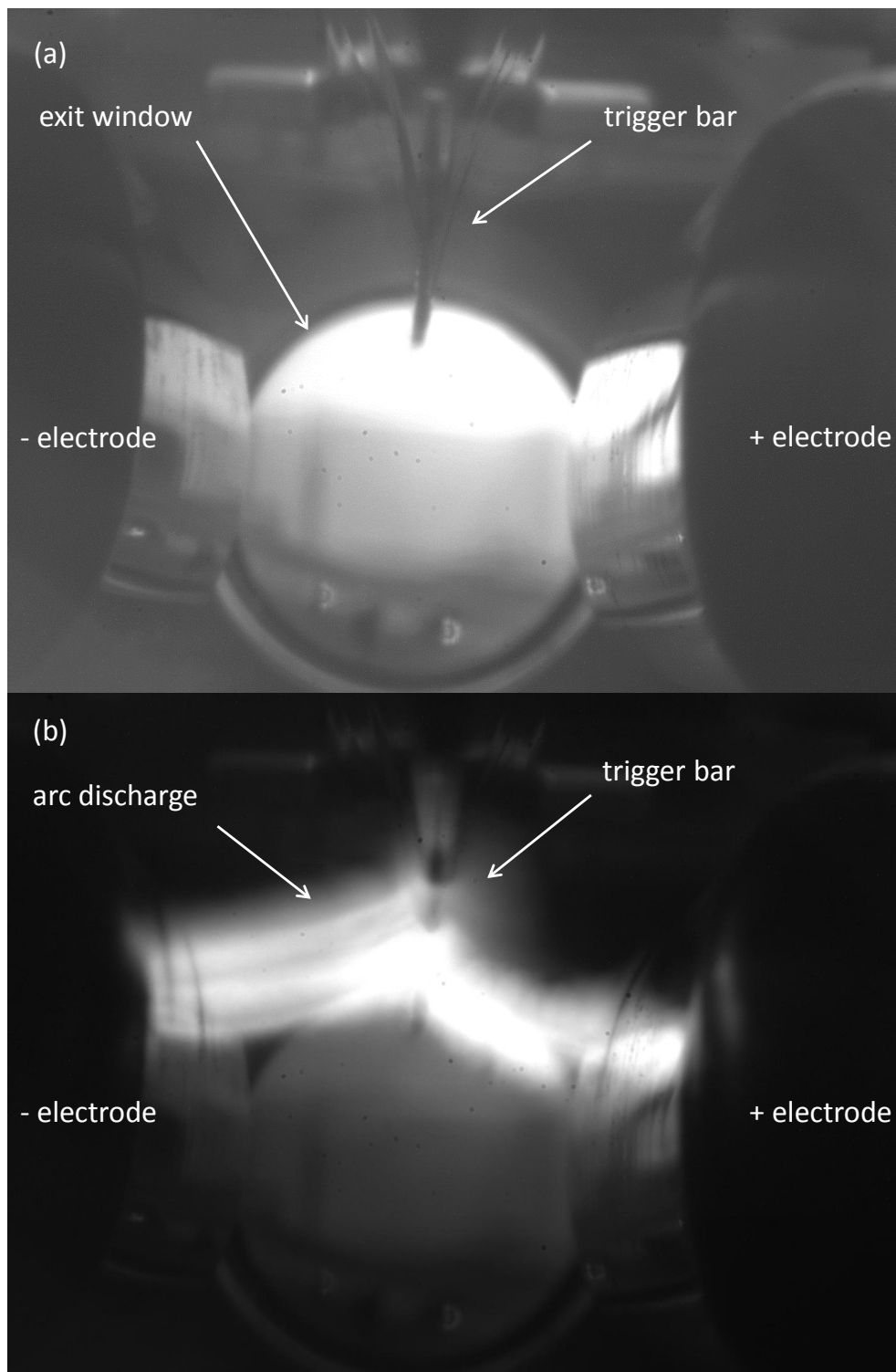


Figure 15. (a) Side-on image of trigger and switch electrodes prior to the arc discharge. (b) Time integrated image of the multi-channel arc discharge (same field of view as in a)

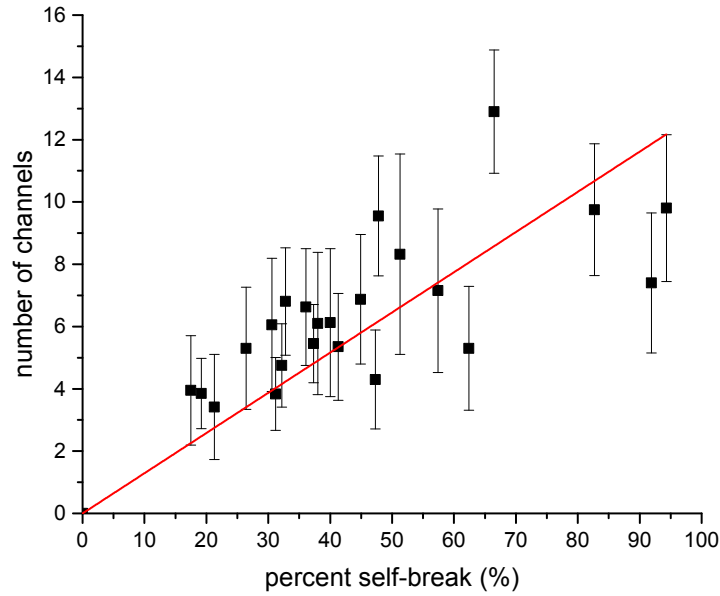


Figure 16. Plot of average visually observed discharge channel count versus self-breakdown voltage.

on the switch and an electrode gap of 1.5 cm. It can be seen that the runtime and jitter decrease with self-breakdown percentage as one would expect. It should be noted that the switch can still be reliably triggered (and multi-channel) at only 20% of self-breakdown voltage. The switch also performs quite well in the high reliability (meaning no self-breakdown occurring) regime of 40% self-breakdown voltage where the runtime is only 15 ns with a jitter of ± 1 ns.

Peak load current versus number of discharge channels is depicted in Fig. 21 for three different switch voltages. One can see that there is only a very weak dependence on the number of arc channels. This is surprising since one would expect the load current to rise as the number of channels increases, i.e. the switch inductance decreases. One could speculate that the benefit of decreasing inductance may be offset by an equally increasing effect of arc channel resistance. Alternatively, it may be possible that most current is only conducted by a small number of channels, or channels close together, in which case the additional channels would not reduce inductance and the peak current would not increase as a result. The weak dependence of peak current on number of channels has an advantage in terms of system reliability and predictability. Since the peak current does not depend on channel number one can always expect the same performance over a wide range of discharge scenarios.

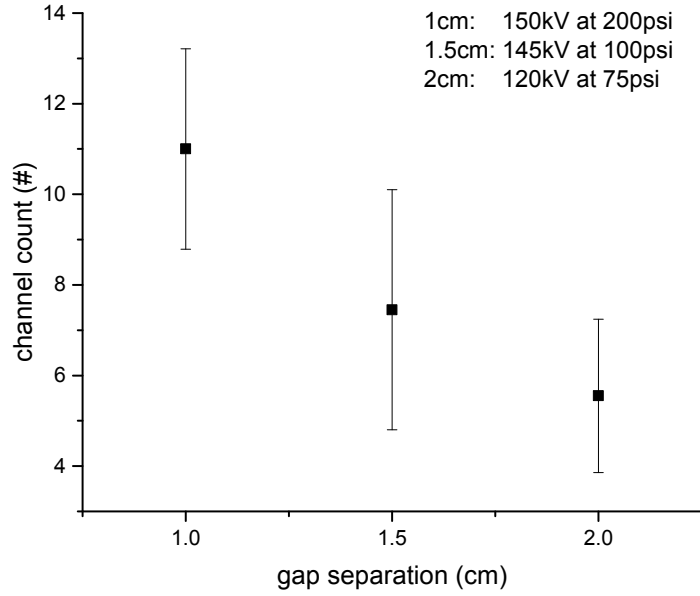


Figure 17. Plot of average visually observed discharge channel count versus gap separation.

Spectral Diagnostics

Spectral diagnostics were performed with a fiber coupled spectrometer (not using the fiber) from Avantes with a resolution of 0.5 nm. The spectrometer was placed 2 m away from the arc discharge so that no filters were required for attenuation. Any minor background signals (e.g. overhead lighting) were subtracted from the data. Figure 22 shows an arc discharge spectrum for dry air at 168 kV switch voltage and 120 psi of pressure. Table 1 shows the elements associated with the observed line emissions. As expected one can identify a number of lines stemming from oxygen, nitrogen, (possibly argon) and iron (part of stainless steel electrode). Please note that the subscript “I” denotes a neutral state. In principle one could calculate the plasma temperature by using the Boltzmann plot method. However, we did not have enough time to complete this work and it was not clear if the spectrometer was absolutely calibrated. If one assumes a Planck spectrum (which is not entirely accurate), one can deduce a temperature of about 4500 K based on the spectral location of the plasma continuum. Figure 23 shows the self-emission spectrum from the arc discharge as a function of pressure. It can be seen that the center wavelength of the continuum emission remains constant and that the relative intensity of the emission lines does not change. The same behavior can be observed in Fig. 24 where we have compared spectra at different discharge voltages. One can then conclude, that the plasma temperature does not change significantly for the pressure and voltage ranges at which we operated.

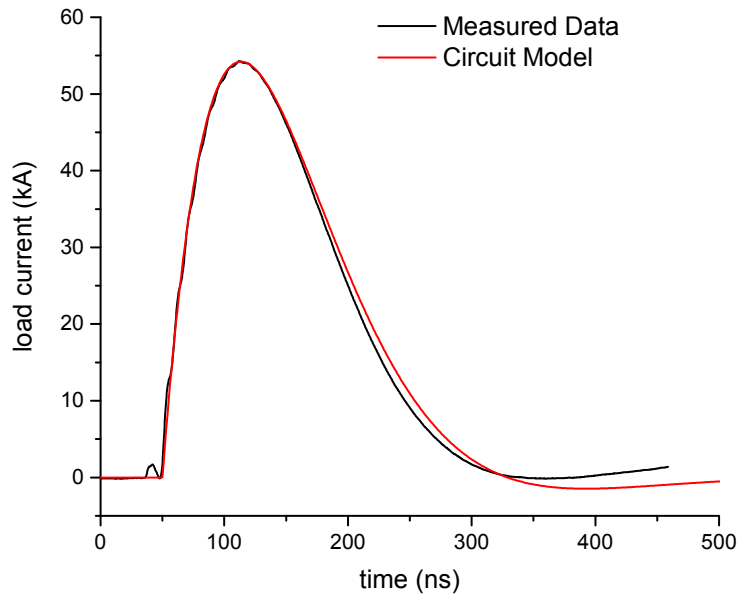


Figure 18. Load current vs. time for 180 kV switch voltage, $2\ \Omega$ total resistance, 40 nF capacitance, and 85 nH inductance. The black curve shows the measured current and the red curve depicts the calculated current based on a circuit model using fixed component values. No amplitude adjustment was applied for this shot.

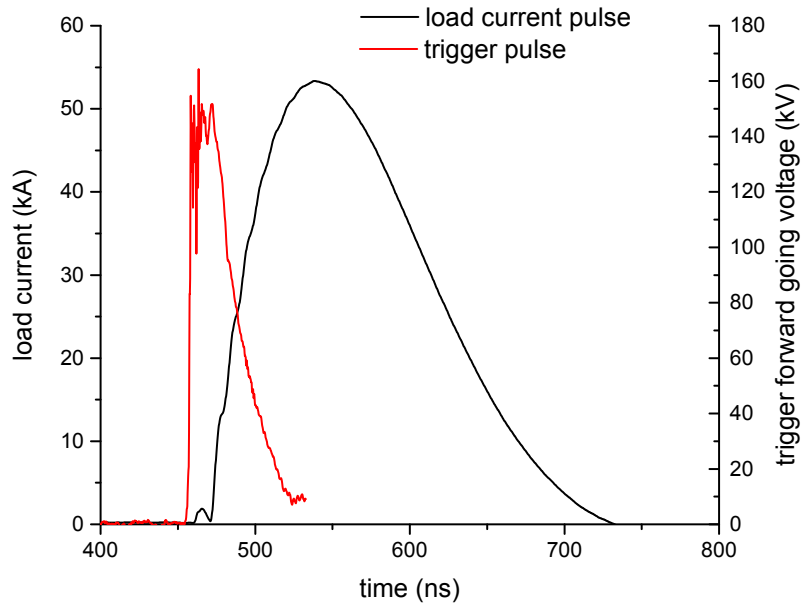


Figure 19. Typical waveform for load current and trigger pulse for 180 kV DC on the switch and an electrode gap of 1.5 cm.

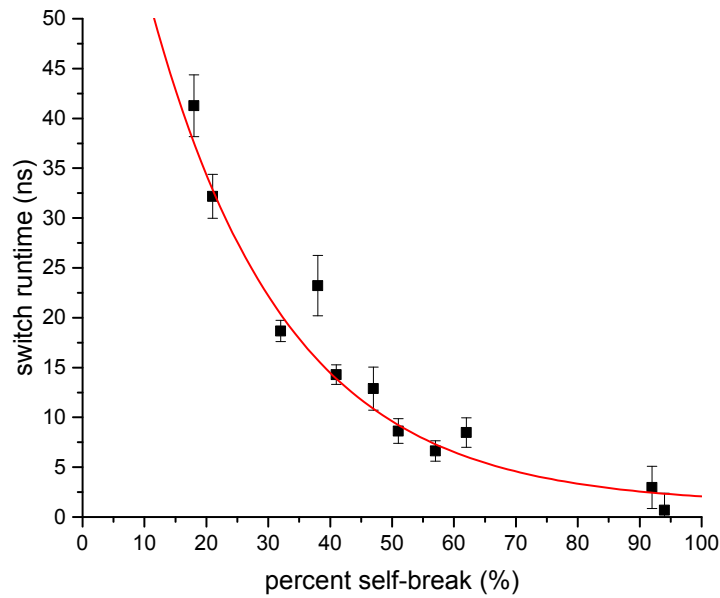


Figure 20. Switch runtime versus percent of self-breakdown voltage with an electrode gap of 1.5 cm. As expected, the graph shows that the switch runtime should approach infinity at low fractions of self-breakdown, and approach zero at 100% self-breakdown.

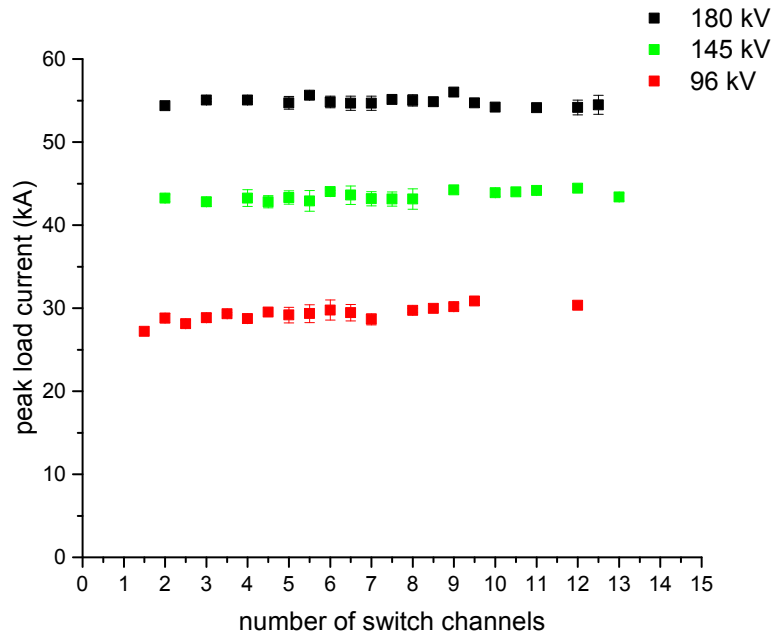


Figure 21. Load current versus the number of discharge channels for 180 kV (black), 145 kV (green), and 96 kV (red) DC voltage on the switch.

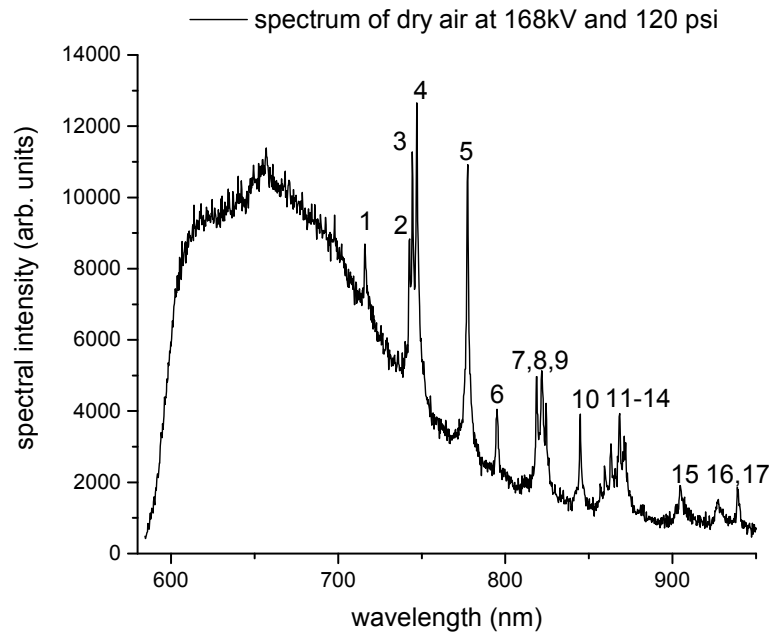


Figure 22. Typical arc-discharge emission spectrum of dry air at 120 psi at a switch voltage of 168 kV DC.

Table 1. Emission spectrum from an arc discharge in dry air at 120 psi and 168 kV DC voltage.

Line #	Wavelength (nm)	Element
1	715.8	O _I
2	742.3	Ar _I , N _I
3	744.1	N _I
4	747.2	O _I
5	777.6	O _I
6	795.2	O _I
7	819.1	N _I
8	822.0	N _I , O _I
9	824.7	Fe _I
10	844.9	O _I
11	856.9	N _I
12	859.5	N _I
13	863.2	N _I
14	868.4	N _I
15	904.4	N
16	927.3	O _I
17	938.8	Fe _I , N _I

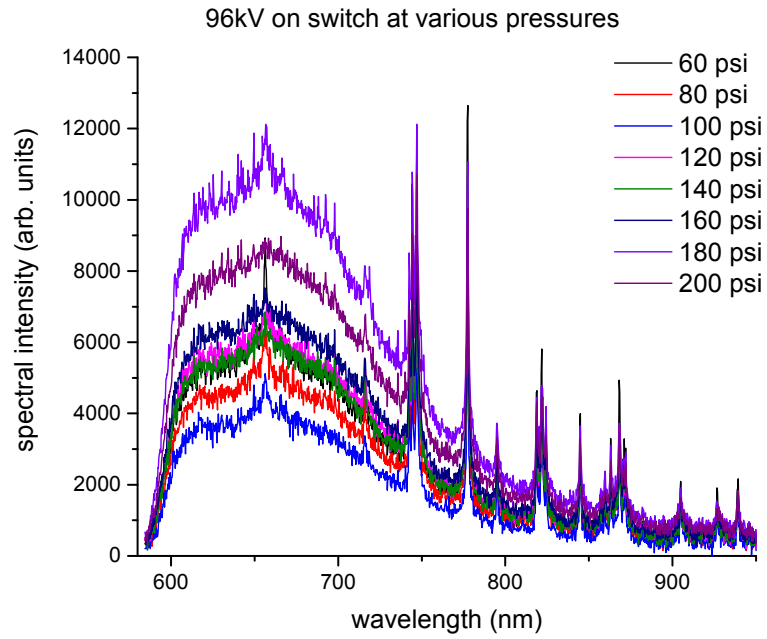


Figure 23. Arc discharge spectrum in dry air at 96 kV DC for various switch pressures.

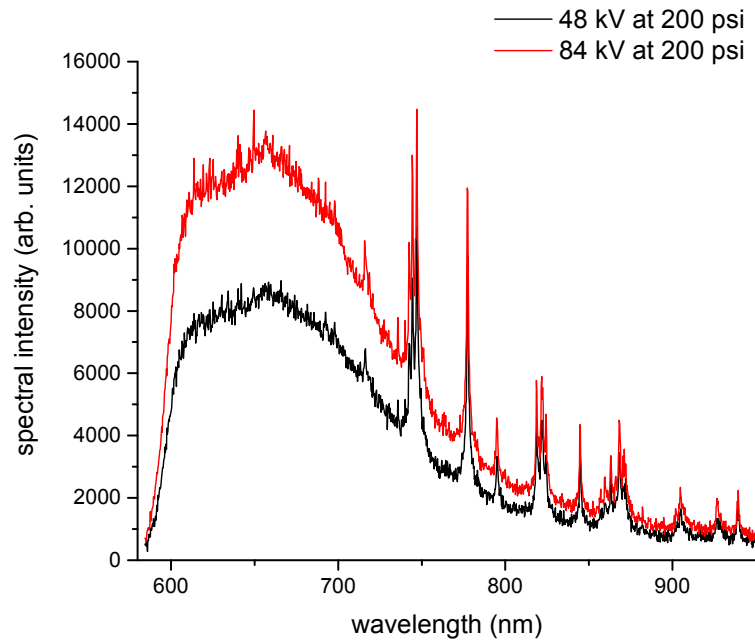


Figure 24. Arc discharge spectrum in dry air at 200 psi for two different switch voltages.

Lifetime Considerations

Unfortunately, we were not able to run this test setup fully automated due to shortcomings in the automation software. However, we took the switch electrodes and trigger bar out of the switch to observe the discharge sites. Figure 25 shows the stainless steel switch electrodes and trigger bar after about 50 shots. One can see the randomly spaced discharge sites on the electrodes and trigger bar which is paramount for long lifetime operation. The discharge sites appear to be oxidized (as expected) but no pitting or rough surface can be detected at first glance.

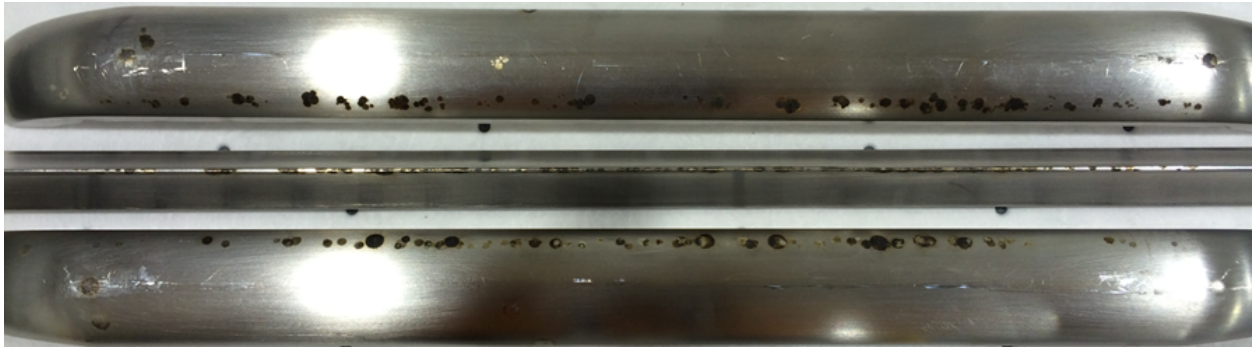


Figure 25. Stainless steel switch electrodes and trigger bar after about 50 shots.

4 Laser Triggered Railgap Switch

Historically, railgap switches have been triggered using a fast rise-time HV supply that is connected to a knife edge trigger bar near one of the switch electrodes, or via a UV pre-ionized channel that runs closely along one of the electrodes [5, 6, 7]. This is feasible for a “handful” of switches but becomes cost and space prohibitive once one considers on the order of 10^5 switches as would be needed in next generation LTD based pulsed power machines [11]. We have therefore started to study the feasibility of laser fiber triggering railgap switches. Such a system would also be more compact by comparison. Two scenarios were supposed to be investigated.

1. Creation of a pre-ionized channel along the switch electrodes: Based on previous work [5, 6, 7], this option may be the best choice as it can create numerous discharge channels along the railgap switch. The drawback is that it takes a high $f/\#$, long focal length lens for focusing in order to create a large depth of focus that can span the length of the railgap electrodes. Furthermore, energy requirements are quite high (many mJ in an order ps long pulsed beam) since a 10+ cm long channel needs to be ionized. This power density cannot currently be handled by any fiber. However, one may imagine that future fibers can handle more power and so we designed our switch with an option to attach a meter long focusing tube at the end of the railgap switch. We would then use free space beam propagation in order to deliver the required power which would give important insight on switch performance when being triggered in this fashion. With this in mind, we started theoretical modeling efforts to understand beam propagation and focusing of high power laser beams in gases. The results from this modeling effort (together with the experiment) would then become an initial electron seed condition for the switch modeling which is detailed in section 6. In the end we made good progress on the laser beam modeling (see section 5) but we never had the time to focus a short pulse beam along the switch electrodes.
2. Focusing multiple laser beams directly onto the switch electrodes: In this scenario one creates multiple seed discharge channels in the railgap switch by hitting the switch electrodes with a focused laser beam. Laser damage threshold for metals is orders of magnitude below that of a gas and hence the energy requirements to ionize the electrode surface are drastically reduced. This in turn allows one to fiber deliver the required energy which we have demonstrated below. The switch housing was designed to be modular so that it could accept an electrical trigger or a laser triggered option. Electrical triggering was demonstrated in the previous section 3 and we finished the design work for a modified switch lid to allow for laser triggering. However, scheduling and budget constraints prevented us from trying this option for the time period of this LDRD.

In this section we will focus on experimental work performed in preparation for laser triggering of a railgap switch using approach number two described above. As such we have built a test setup that would allow us to optimize the fiber focusing onto a switch electrode. Furthermore, we studied the size of the laser generated plasma plume versus laser energy and electrode material. In addition we built a “test capacitor” where we could measure the temporal change in capacitance as the laser

hits one of its plates. This can be used as an indicator of switch jitter in a full railgap switch: the faster the capacitance (plasma current) changes, the less jitter one expects.

4.1 Visual plasma plume measurement

Fiber setup and subsequent fiber output focusing

Our goal is to fiber trigger a rail gap switch. The main advantage of those switches is the fact that they can have multiple discharge channels which lowers the switch inductance. As such, we aim for a minimum of four laser generated plasma sparks along the HV electrode. In order to keep the system simple and compact we launch the laser beam into a single large core 1 mm diameter fiber which is then split four ways (we also have options available for five and seven way split). However, at fiber core sizes of 1 mm one cannot build a fiber splitter in the traditional sense. To overcome this limitation, CeramOptec developed a large area fiber splitter based on smaller fiber bundles. Figure 26 shows how 100 individual 100 μm diameter fibers are fused at the input/output face (to yield a 1 mm diameter solid core) and later split into four fiber bundles with 25 fibers each. Input and output faces are connectorized with an Amphenol 905 high power SMA connector that plugs straight into our fiber launcher. The fiber injected laser energy stems from a Quantel Ultra 50 flashlamp pumped Nd:YAG laser operating at 1064 nm wavelength, 50 mJ of energy, a temporal pulsewidth of 7 ns FWHM, and a repetition rate of 20 Hz. The system is equipped with a custom fiber launcher that can safely inject 45 mJ into the fiber core.

The output from our fiber bundle is a combination of 25 individually randomly polarized beams with a numerical aperture of $\text{NA}=0.22$. As such, it does not resemble a Gaussian beam at all and cannot be focused in the same way as one would expect from a TEM00 laser mode. The laser fluence on the electrode can only be increased by de-magnifying the fiber bundle output surface. Based on the thin lens equation:

$$\frac{1}{f} = \frac{1}{I} + \frac{1}{O} \quad \text{and} \quad M = \frac{I}{O}, \quad (1)$$

one can see that large de-magnification M at image distance I can only be achieved by having a large object distance O and/or a short focal length f lens. A large object distance is not feasible due to the large $\text{NA}=0.22$ (12° half angle) of the fiber, i.e. an object distance of only 10 cm would result into a 4 cm diameter beam at the focusing lens. This is clearly not possible for the rail gap design that has four (or more) trigger points along a 10-20 cm rail gap switch. After an extensive search we picked an aspheric $f/\# = 0.8$, 25 mm diameter AL2520 lens from Thorlabs with an effective focal length of 20 mm. At an object distance of 55 mm, the fiber output will fill the complete lens surface and will de-magnify the output surface by a factor of 1.9. Experiments were also performed with a single straight through 1 mm core fused silica fiber in order to reach higher fluences on target and to compare its performance to a fiber bundle at similar fluence levels. Figure 27(a) shows a de-magnified image of the end face of the straight through 1 mm diameter fused silica fiber core, (b) depicts the fused in silica fiber end face of one of the 1:4 split lines, and (c) is a near field image of the individual 100 μm fiber ends before they are fused in silica.

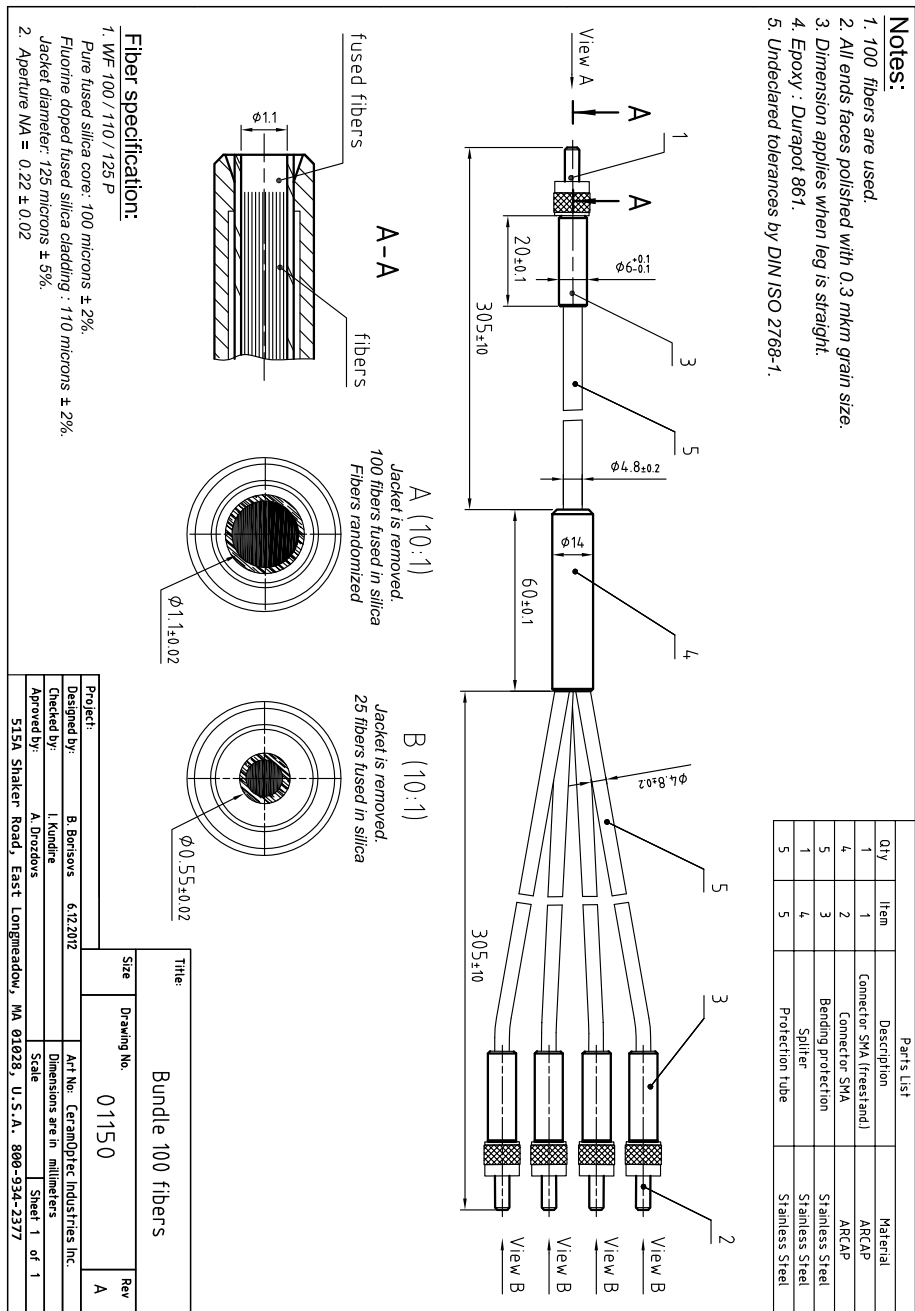


Figure 26. 1:4 large core fiber splitter based on 100 individual 100 μm core fibers that are fused in silica at the input and output face. The ns laser pulse is launched into the fused fiber end of a high power Amphenol SMA connector (A) after which it is transported close to the rail gap switch. At that point, the beam is split four ways and the outputs are focused into the HV switch. Drawing courtesy of CeramOptec Industries Inc.

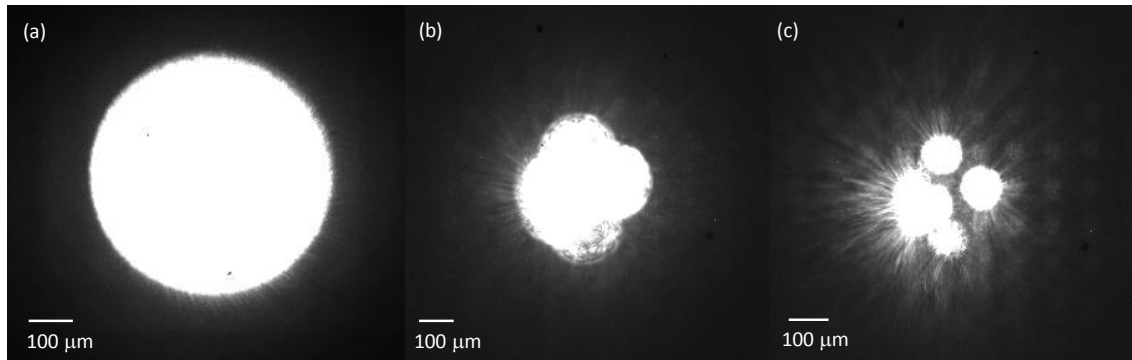


Figure 27. Near field image of de-magnified fiber output for: (a) a straight through 1 mm diameter fused silica core fiber, (b) a single 1:4 split fiber line, showing the 25 fibers fused in silica surface, (c) end-face of the individual 100 μm diameter fiber just before they are fused in silica.

Visual measurement of plasma size

Aluminum, Brass, Graphite, and Titanium were chosen as possible candidates for HV rail gap electrodes. Visual measurements of laser generated plasma plume size were performed as follows: A triggered CCTV camera with a $f/\# = 16$ objective was placed at a side on view with respect to the 25 mm diameter, 2 mm thick material target disc. Plasma images were recorded at 10 Hz for various laser energies and fiber configurations. Figure 28 depicts a laser generated plasma plume for a straight through fiber output energy of 17 mJ and a laser beam diameter of 560 μm FWHM on a titanium target. The image is saturated in order to show the maximum extent of the plasma. One can see that the plume is hemispherical and that particulates are ejected beyond the plasma boundary. Figure 29 plots the measured plasma plume radius (a) and diameter (b) versus laser energy for the large core fiber case having a de-magnified laser spot diameters of 560 μm FWHM. The large, solid core fiber was used in order to collect data over a broader energy range as would be available for a 1:4 splitter option. For the rail gap switch trigger however, we will use a 1:4 fiber splitter. Figure 30 depicts a comparison of plasma plume size between a large solid core fiber and a single 1:4 split beam for an aluminum target. The large core fiber had a spot size of 560 μm diameter (corresponding to Fig. 27(a)) and the single split fiber had a spot size shaped as depicted in Fig. 27(b-c). For the single split fiber, the distance from the imaging asphere to the target was optimized for maximum plasma plume size. Since the image distance corresponding to the near field images of Fig. 27(b-c) are almost the same, it is not quite clear what image yielded the best performance. For our trigger application however, this makes no difference. One can see from Fig. 30 that the single split beam performs much better at lower fiber output energies. This is expected due to its smaller beam size on target. For our application, this is the desired behavior.

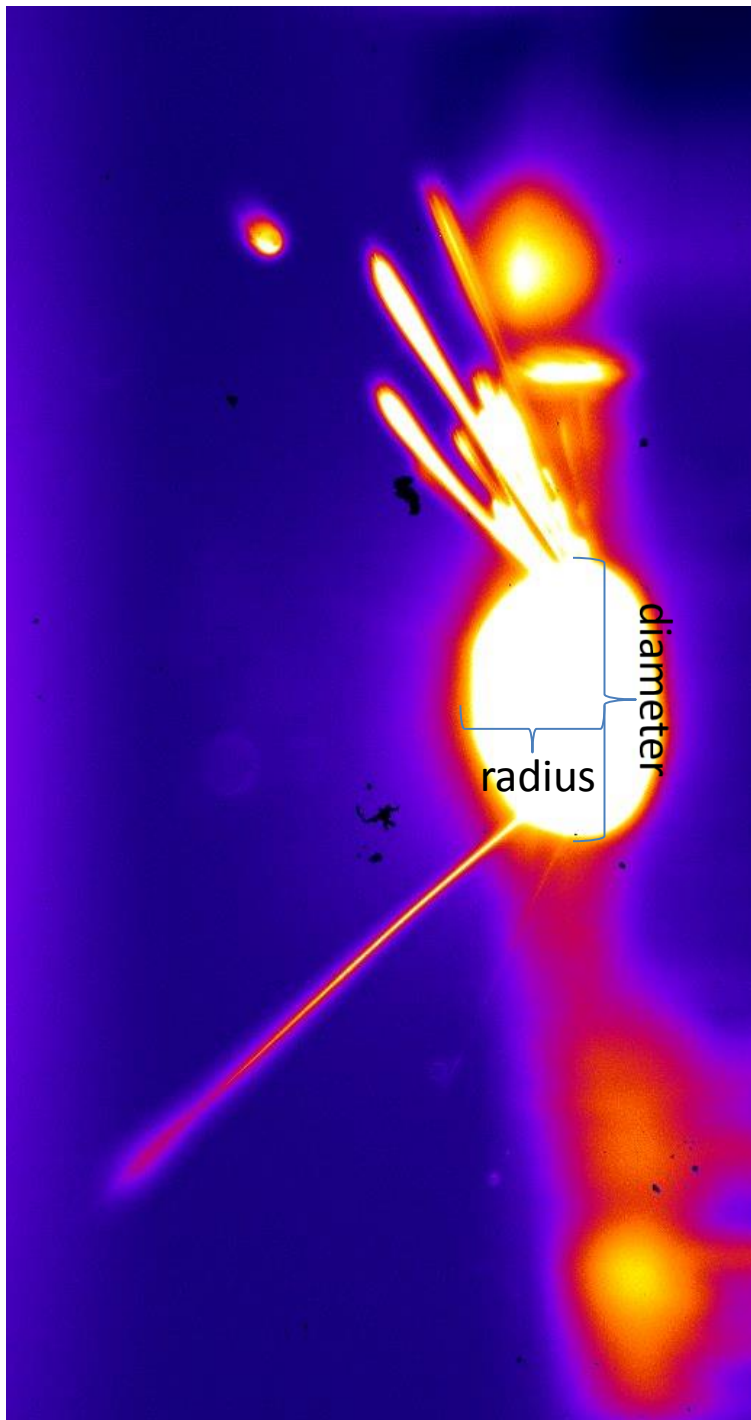


Figure 28. Time integrated plasma plume created by laser light impinging on a titanium target irradiated by 17 mJ of laser light from a straight through fiber focused to a spot size of $560\text{ }\mu\text{m}$ diameter. The resulting nearly hemispherical plasma plume has a diameter of 2.6 mm and a radius of 1.0 mm.

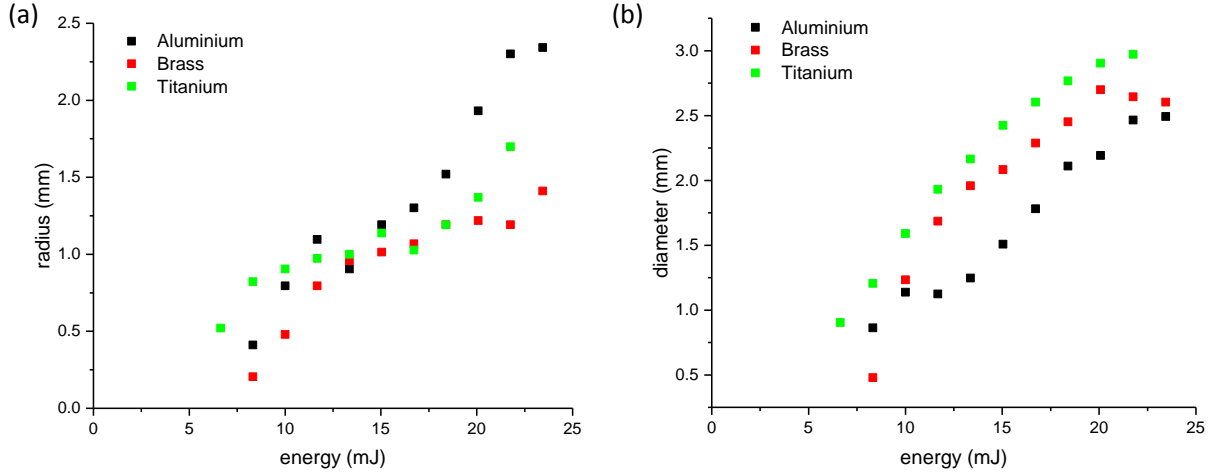


Figure 29. Visual extent of plasma plume radius (a) and diameter (b) versus fiber output energy for a de-magnified spot size of $560\ \mu\text{m}$ out of a 1 mm solid fused silica fiber. Note that no substantial plasma plume could be detected for the graphite material.

4.2 Electrical plasma plume measurement

Although visual measurements are a good indicator of plasma size, it is not the most relevant parameter in determining switch closure behavior. The initial dynamics of switch closure are governed by the electric field enhancement due to the creation of the laser plasma on the electrode surface. The time-integrated images do not give any information as to the expansion velocity of the plasma.

Capacitive change experiment

Prior work has been done using displacement current measurement of laser-created plasma in bulk gas [12, 13]. Perhaps more commonly used is fast photography and interferometry, but those methods require calibration of the system response and possibly more elaborate setups and equipment. A purely electrical measurement could be considerably simpler. In addition, capacitance measurements record directly the distortion of the electric field lines, which is the same mechanism that would cause triggering of a switch. Consider the geometry shown in Fig. 31(a). A 50 V bias is applied between the aperture plate and the target. As the laser hits the target and forms a plasma, one might expect that the expanding plasma would be a zero work function particle emitter causing switch closure. However, at the fields and pressures used, ($\approx 100\ \text{V/cm}$ and 600 Torr) the electron transit time across the diagnostic is many microseconds [14, 15]. This is a result of operating the gap at fields about 1% of the breakdown field in atmospheric air. For this reason we neglect conduction current and calculate the response based solely on displacement current. This is demonstrated by the fact that reversing bias polarity showed no difference in system response,

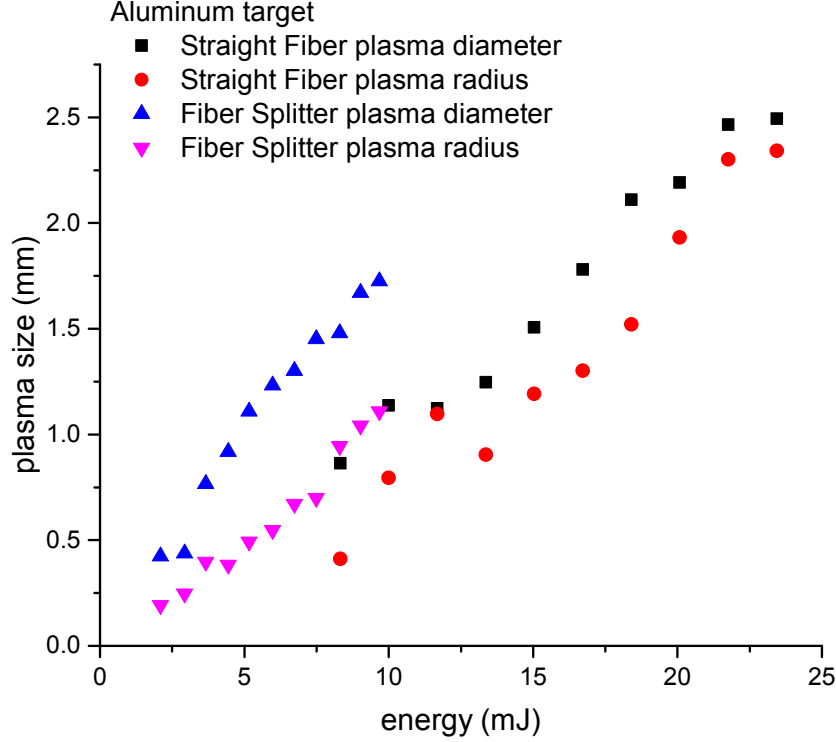


Figure 30. Comparison of plasma plume size between a large solid core fiber and a single 1:4 split beam. The beam shape on target corresponds to the near fields depicted in Fig. 27(a) and Fig. 27(b-c) respectively.

confirming the supposition that electron flow from the plasma is negligible.

Plasma created by the laser beam impact expands towards the aperture, effectively reducing the separation d between the capacitor plates. This causes an increase in the capacitance C between the aperture and the target according to $C = A/d$ (where A is the area of the capacitor plates). The charge q stored in the capacitance C is unchangeable on a nanosecond time scale because of the large bias resistance. Increasing capacitance causes a voltage V magnitude reduction based on the relation: $q = C \times V$. The dimensions of the device are much smaller than electromagnetic transit times for the multi-nanosecond plasma formation times, so a lumped-element circuit approximation is valid. When the capacitance increases, the voltage on the capacitance falls and (necessarily) capacitive energy E is lost ($E = \frac{1}{2}CV^2$). The energy goes entirely into heating the expanding plasma. This energy, bounded by the initially charged capacitance is of order a few nJ at 50 V bias, is much smaller than the incoming laser energy (order of 10 mJ) and is neglected here. Such energy would not affect the diagnostic, but the energy added to the plasma could affect the expansion. Note that in a high voltage device, this capacitive energy can be significant and can play a part in the plasma behavior. For this experiment, we were purely interested in the laser-surface interaction for different laser energies and different materials. Based on the circuit model

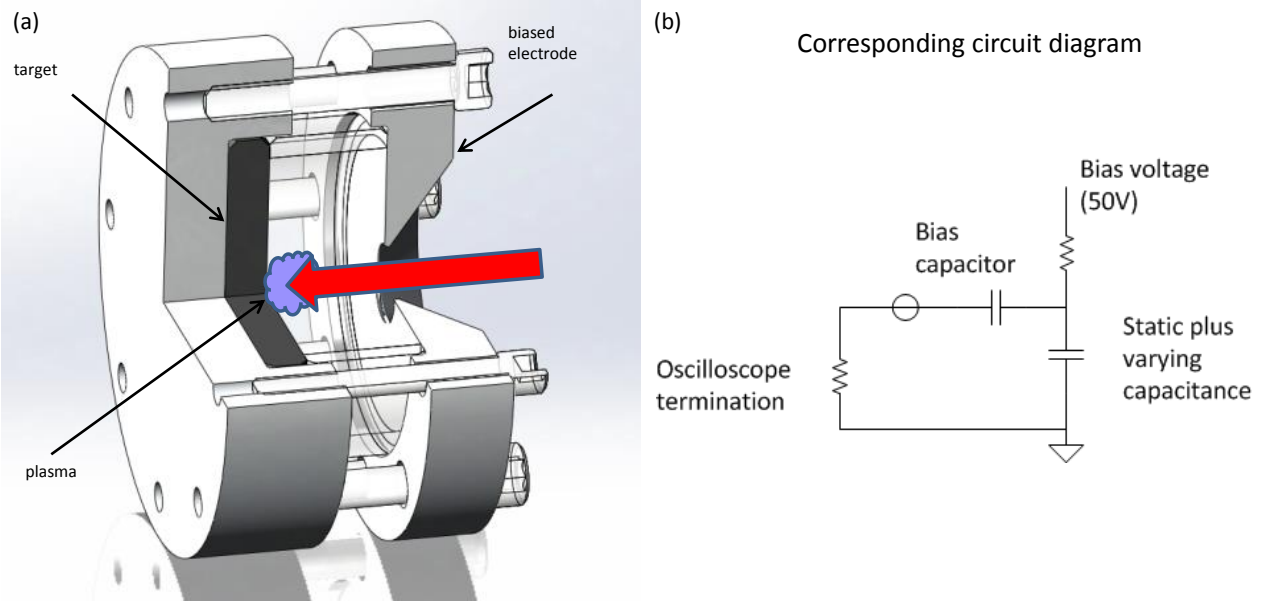


Figure 31. Apparatus used to measure the capacitance change directly by recording the voltage change due to the laser beam striking one electrode of a biased capacitor. As the laser strikes the target electrode, a plasma is created, the capacitance of the system changes, and the corresponding voltage change is recorded on a digitizer. (a) shows the capacitor setup in detail and (b) depicts the corresponding circuit diagram used to measure the displacement current. The target disc is 25 mm in diameter and the separation between the electrodes can be varied between 5 and 10 mm. A +50 V bias voltage is applied to the electrode facing the incoming beam whereas the target electrode is held at ground potential.

in Fig. 31(b), the capacitance change ΔC can be calculated as follows:

$$\Delta C = \frac{1}{Z_0(V_{\text{scope}} + V_{\text{bias}})} \int_{-\infty}^t V_{\text{scope}} dt \quad , \quad (2)$$

where $Z_0 = 50 \Omega$ is the cable termination impedance, $V_{\text{bias}} = 50 \text{ V}$ is the DC voltage on the dynamic capacitor, and V_{scope} is the recorded signal. It is assumed that the bias capacitor (see circuit model Fig. 31(b)) is much larger than the final value of the dynamic capacitance.

Figure 32a shows a voltage trace (red) with respect to the laser pulse (black) for an energy of 10 mJ and a spot size of $470 \mu\text{m}$ FWHM on target. One can see that the capacitance change occurs precisely at the peak amplitude of the laser pulse and has an average rise-time (10%-90%) of about 15 ns regardless of laser spot size and experimental setup (see Fig. 33). Figure 32(b) implies that the plasma starts expanding at peak laser power, but the ultimate expansion does not conclude for about 150 ns. If jitter is a fraction of the trigger evolution time, this method of triggering could have more jitter than a fast rise electrical trigger.

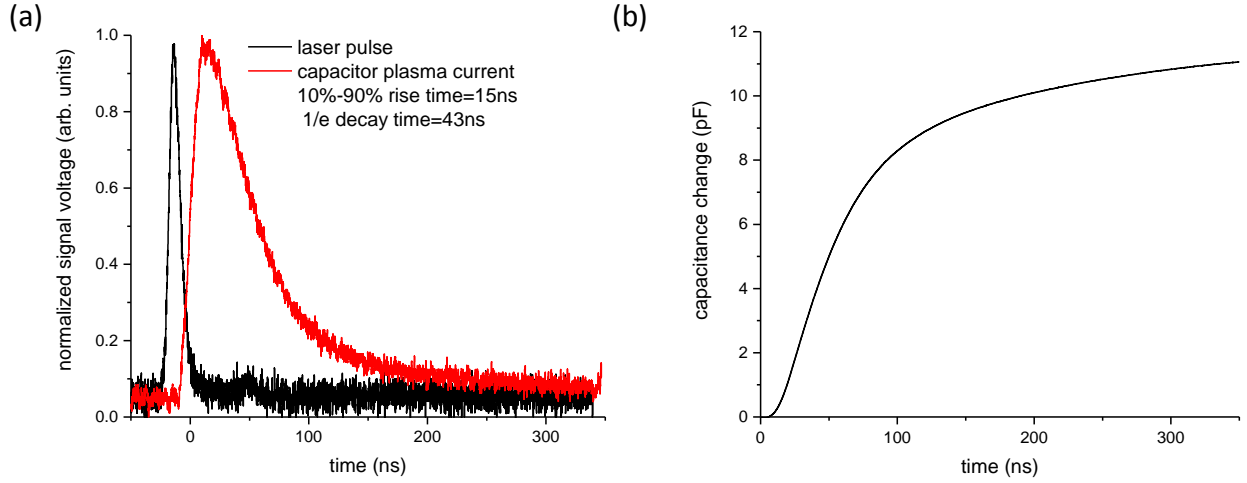


Figure 32. (a) Normalized laser temporal diode trace with respect to derivative of capacitance change. (b) Change in capacitance versus time.

Comparison with visual results

To demonstrate the validity of this method, we focused the laser output from the 1 mm diameter straight through fiber into a capacitor setup with an aluminum target. Figure 34 shows the calculated and visually measured plasma plume radius/diameter versus laser intensity/energy for two different beam intensity ranges corresponding to focal spot diameters of (a) $240\ \mu\text{m}$ and (b) $470\ \mu\text{m}$ respectively. One can see that there is good agreement between the calculated and visually observed plasma diameter over a large range of beam intensities (Fig. 34(a)). For larger focal spot sizes (see Fig. 34(b)) there is slight disagreement in that the visual results seem to overestimate the beam diameter and do not indicate saturation as early as predicted by the circuit model. Overall, it appears that the circuit model based calculation of plasma plume size is a valid method which has the advantage that one does not rely on a rather subjective visual interpretation of plasma plume sizes. Figure 32 shows the plasma reaches nearly maximum size in about 150 ns (the integral of V_{scope}) and then stays nearly constant, growing very slowly. This seems reasonable for hydrodynamic expansion. This also is quite different than electrical triggering, which happens in less than 2 ns. For this reason, one may question if laser triggering can be as good as electrical triggering.

4.3 Laser Switch Triggering Design

Even though we did not succeed in demonstrating a laser triggered switch, we did complete a design of a modified switch housing based on the focusing scheme shown in Fig. 35. Based on the fiber focusing consideration in section 4.1 we have chosen a commercial asphere from Thorlabs (AL2520) with an $f/\# = 0.8$. One can see that the lens placement avoids high electric field areas while preserving a short focal distance and beam clearance with the switch housing. In this

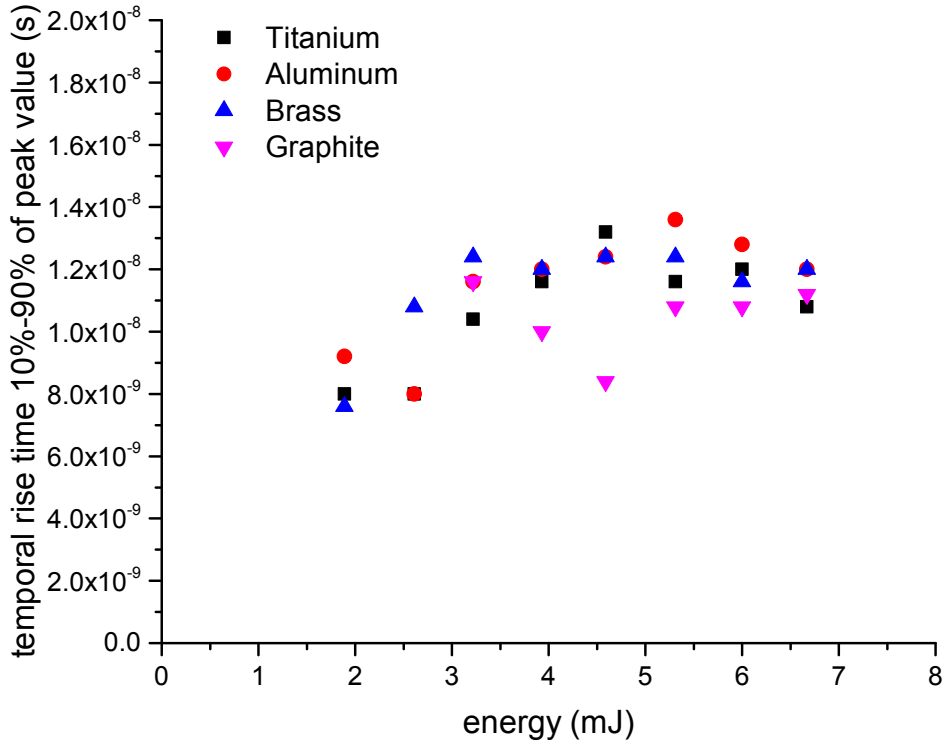


Figure 33. 10%-90% temporal rise time of the probe voltage for a single 1:4 fiber splitter line versus laser energy and target material.

configuration, the fiber output is placed 54.5 mm (object distance) away from the lens. At that distance, the beam will fill the whole aperture of the lens and will focus 25 mm from the lens at an angle of 55° with respect to the electrode surface normal. For a 1:4 fiber split beam this demagnification of 2 will yield a focal spot diameter of $550 \mu\text{m}/2 = 225 \mu\text{m}$ in one dimension and $550 \mu\text{m}/(2 * \cos 55) = 390 \mu\text{m}$ in the other dimension. At an expected output energy of 10 mJ and a laser temporal FWHM of 7 ns, this will yield a focus intensity of $2 \text{ GW}/\text{cm}^2$. According to Fig. 34, this is enough to generate strong plasma plumes.

The design implementation of this focusing scheme is driven by the fact that the low $f/\#$ focal length lens causes a high sensitivity of magnification and object distance with respect to focal distance (see Fig. 36). For that reason, the design needs to allow for enough flexibility to “dial in” the correct distance and enough strength to hold everything in place shot after shot.

Figure 37 depicts the concept for the laser triggered design. The trigger bar has been replaced by metal cross-bar that holds the lens array for beam focusing. As a result, the switch lid has to be modified in order to accommodate the cross-bar as well as laser entry windows. Figure 38 shows this new design in more detail. One can see that the lenses are equally spaced along the length of the switch electrode in order to provide a maximum benefit for switch inductance reduction.

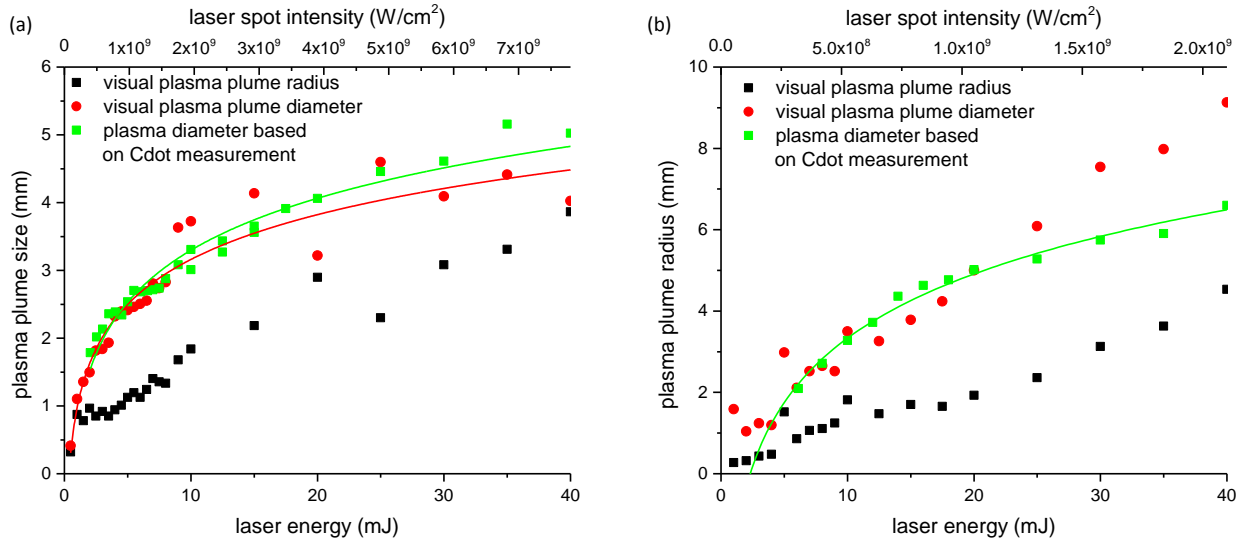


Figure 34. Calculated and visually measured plasma plume radius/diameter versus laser intensity/energy for two different beam intensity ranges corresponding to focal spot diameters of (a) 240 μm and (b) 470 μm

The lens holder bar has been designed with tip/tilt capability and variable focal distance in order to provide optimal beam focus capability. The relatively shallow depth of focus will make focus adjustments somewhat critical.

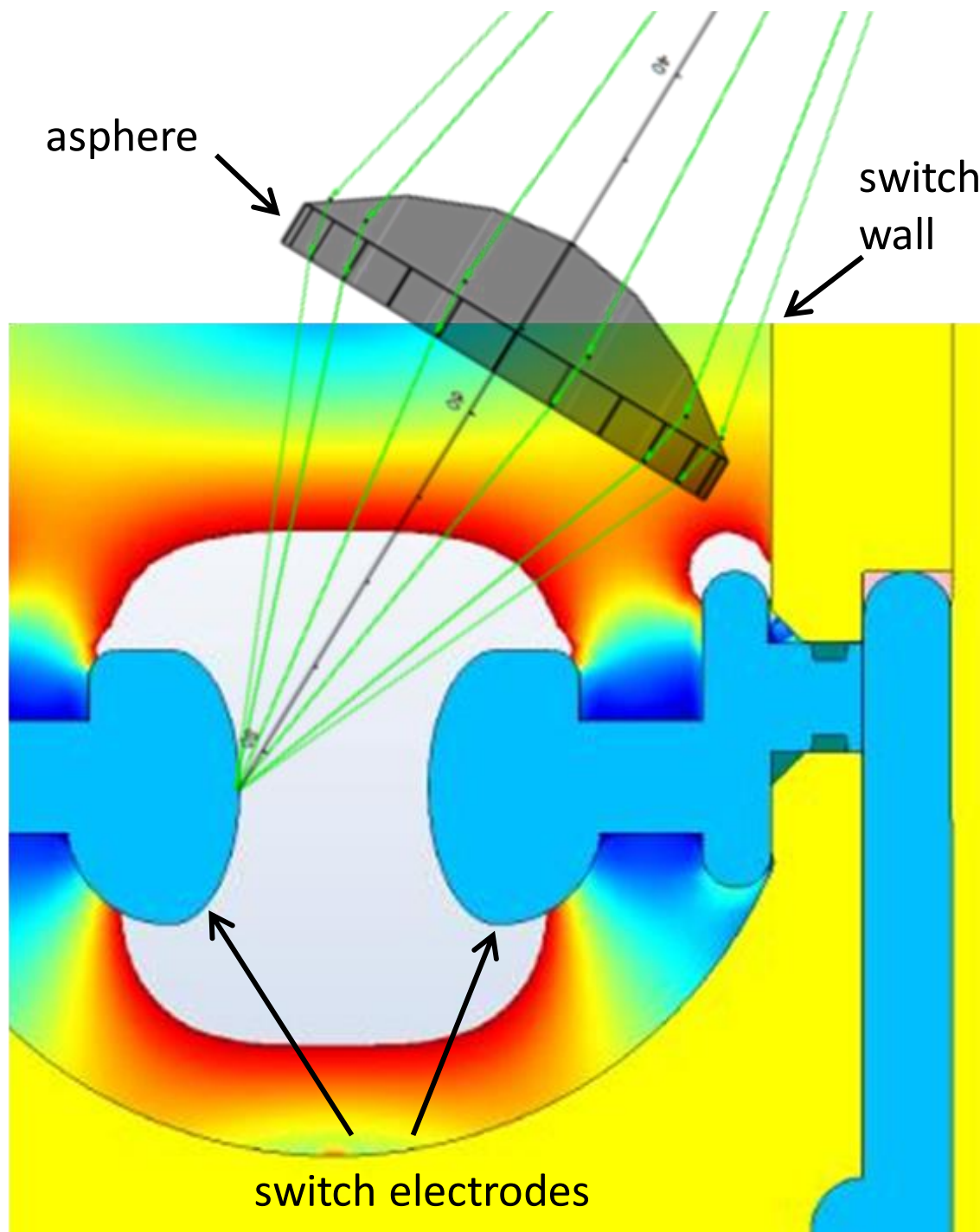


Figure 35. Cross-sectional view of the switch housing with the electric field distribution. A 25 mm diameter asphere is placed 25 mm away from the switch electrode at a laser incident angle of 55° .

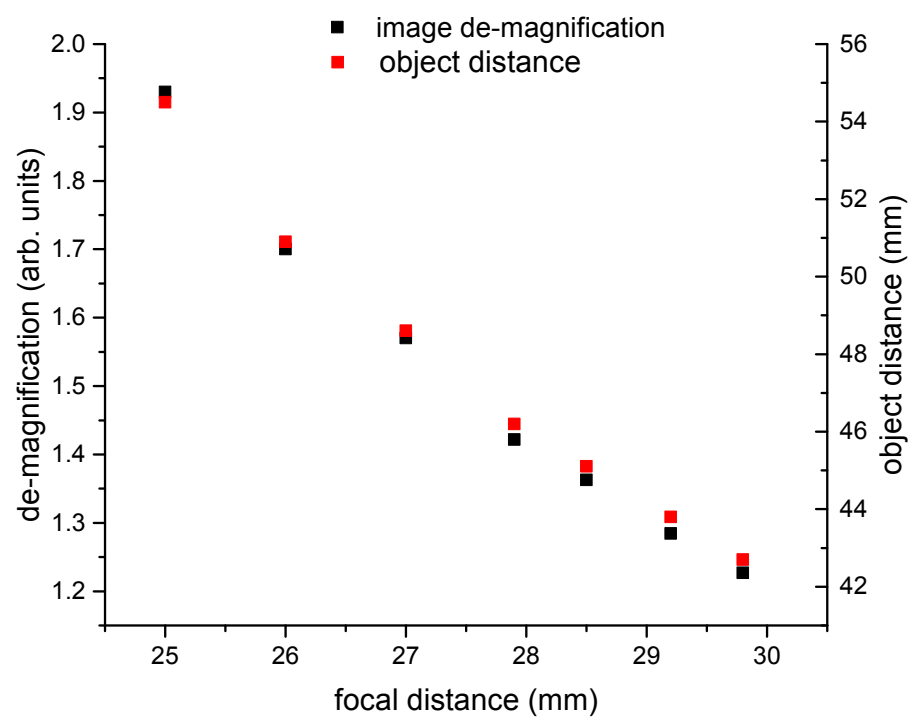


Figure 36. Image de-magnification (black) and object distance (red) as a function of focal distance.

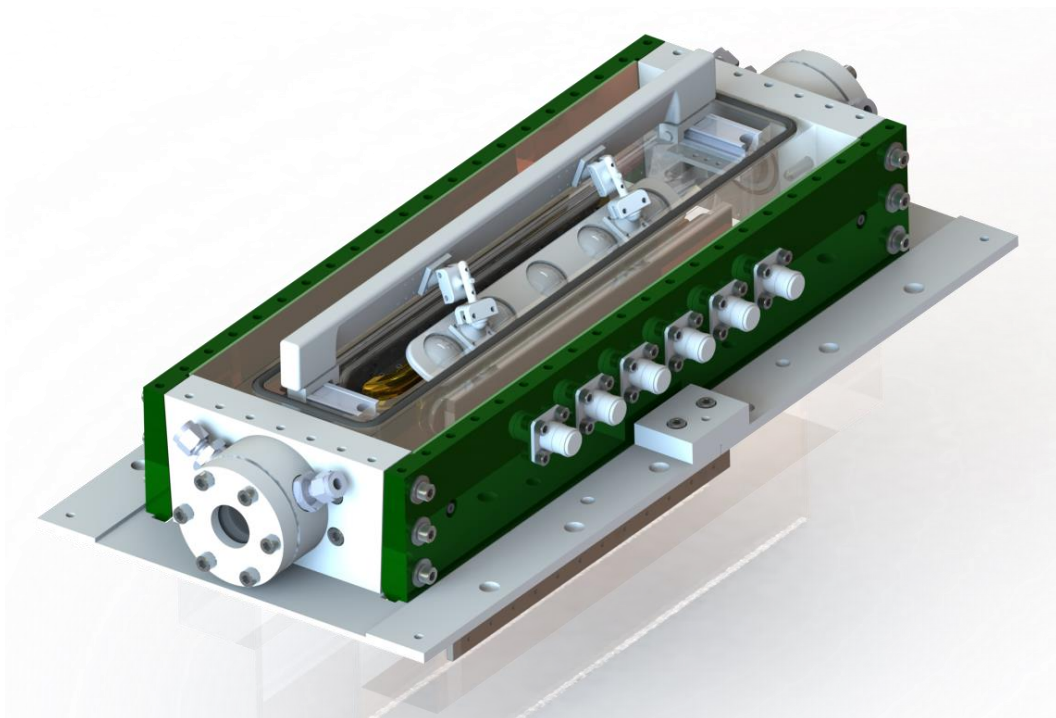


Figure 37. Initial design for the laser triggering concept. The electrical trigger bar has been replaced by a lens focusing bar.

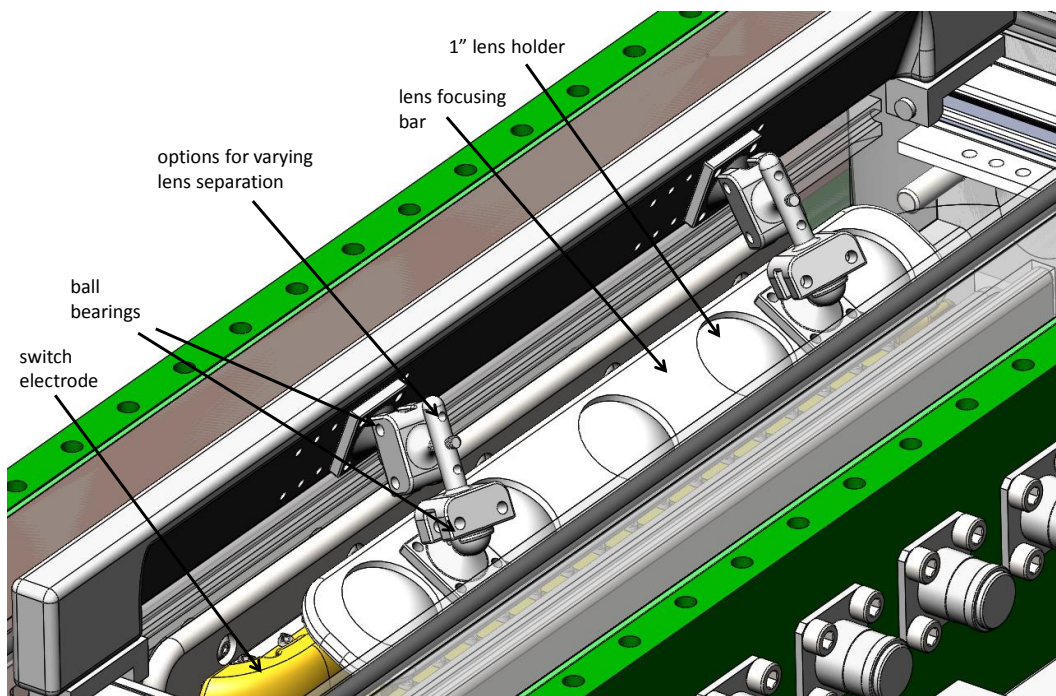


Figure 38. Detailed view of the laser triggering concept.

5 Laser Beam Modeling

5.1 Introduction

We provide a summary of the laser beam propagation model (section 5.2) and discuss the modeling codes developed to simulate it (see section 5.3). We also go over validation of the codes through comparison via some simple known solutions to propagation problems (section 5.4) and comparison with published solutions (section 5.4). Finally, we conclude with a discussion of advances in our understanding of modeling nonlinear optical propagation resulting from the research conducted during this and the previous LDRD.

A general development of the mathematical physics underpinning the optical propagation and material interaction models may be found in the paper titled “Numerical Modeling Considerations for an Applied Nonlinear Schrödinger Equation,” recently submitted for review and publication in Applied Optics. The numerical development is also detailed in the paper.

5.2 Physical Model

This section summarizes the physical models for optical laser beam propagation and material interaction. A table of symbols can be found in section 5.5. The model includes paraxial diffraction, group velocity and third-order dispersion, linear and nonlinear shock, ionization and Kerr and Raman effects. Similar models for nonlinear optical propagation are found in the literature [16, 17, 18, 19, 20, 21, 22, 23, 24]. However, our method of including the impedance effects in the plasma defocusing term leads to a difference in the number of shock terms from some of the common models. See, for example, Couairon [18]. Our paper (currently in review) discusses this development in detail [25].

The following describes the physical model used in our modeling effort. The electric field envelope \mathcal{E} evolves according to the propagation equation

$$\partial_\zeta \mathcal{E} = \frac{i}{2k} T^{-1} \nabla_\perp^2 \mathcal{E} + iD\mathcal{E} + T\mathcal{N}\mathcal{E}, \quad (3)$$

with wavenumber $k = 2\pi/\lambda$ and wavelength λ . Dispersion and shock operators are given by

$$D \equiv -\frac{k''}{2} \partial_\tau^2 - i\frac{k'''}{6} \partial_\tau^3 \quad \text{and} \quad T \equiv \left(1 + \frac{i}{\omega_o} \partial_\tau\right) \quad (4)$$

respectively. The nonlinear operator \mathcal{N} is written as

$$\mathcal{N} = \mathcal{N}_{\text{kr}} + T^{-1} \mathcal{N}_{\text{pls}} + T^{-1} \mathcal{N}_{\text{MPA}}. \quad (5)$$

We now specify the material interaction models for instantaneous nonlinear polarization (Kerr effect), Raman scattering and ionization. Kerr and Raman effects are both functions of the third power of the electric field envelope. As such they may be modeled with similar terms via

$$\mathcal{N}_{\text{kr}} = ik_o n_2 [(1 - \alpha) \mathcal{I} + \alpha \mathcal{Q}_R]. \quad (6)$$

The fractional contributions of Raman and Kerr are given by the term α . The relationship between the intensity and electric field envelopes \mathcal{I} and \mathcal{E} is *approximately* time-harmonic and is given as

$$\mathcal{I} \approx \frac{cn_o\epsilon_o}{2}|\mathcal{E}|^2. \quad (7)$$

The Raman response is assumed to follow a simple delay equation given as

$$\mathcal{Q}_R(\mathbf{r}, t, z) = \int_{-\infty}^t R(\tau) \mathcal{I}(\mathbf{r}, t - \tau, z) d\tau, \quad (8)$$

where

$$R(t) = \frac{\gamma^2 + \omega_R^2}{\omega_R} \exp(-\gamma t) \sin(\omega_R t). \quad (9)$$

The characteristic frequency and attenuation constants for the molecular species interacting with the pulse are respectively ω_R and γ .

Description of the ionization physics requires the following definitions:

- τ_c = Electron collision or relaxation time
- m_e = Mass of an electron
- ω_o = Laser pulse center frequency
- k_o = Pulse center wavenumber
- n_o = Background refractive index
- K = Photons required to free single electron
- U_i = Energy required to free single electron
- ρ_{nt} = Neutral atom number density
- α_r = Electron-positive ion recombination loss
- σ_k = Ionization cross-section.

The plasma created through ionization of material by the pulse lowers the effective local refractive index. The resulting nonlinear effect causes defocusing of the pulse and is described by the operator

$$\mathcal{N}_{\text{pls}} \mathcal{E} = -\frac{ik_o}{2n_o\rho_c} T^{-1}(\rho \mathcal{E}). \quad (10)$$

If we desire to include the effects of collisions between electrons and the heavier positive ions via the Drude model we may use

$$\mathcal{N}_{\text{pls}} \equiv -\frac{\sigma}{2}(1 + i\omega_o\tau_c)\rho. \quad (11)$$

In either case we define

$$\rho_c \equiv \epsilon_o m_e \omega_o^2 / e^2, \quad \text{and} \quad \sigma \equiv \frac{k_o}{n_o \rho_c} \frac{\omega_o \tau_c}{1 + \omega_o^2 \tau_c^2}. \quad (12)$$

We must account for energy loss in the pulse due to multiphoton absorption. We do so via

$$\mathcal{N}_{\text{MPA}} = -\frac{\beta_K}{2} \mathcal{I}^{K-1}, \quad (13)$$

with

$$\beta_K = \sigma_k \rho_{\text{nt}} K \hbar \omega_o. \quad (14)$$

Finally, we need an auxiliary equation to describe the evolution of the electron density as the pulse propagates through a region of the material. If we know the neutral atom or molecule density we may use

$$\frac{d\rho}{dt} = \frac{\sigma}{n_o^2 U_i} \rho \mathcal{I} + \mathcal{I}^K \sigma_k (\rho_{\text{nt}} - \rho) - \alpha_r \rho^2, \quad (15)$$

which accounts for saturation effects. If we don't have access to the neutral species density or saturation effects are not present then we use

$$\frac{d\rho}{dt} = \frac{\sigma}{n_o^2 U_i} \rho \mathcal{I} + \frac{\beta_K}{K \hbar \omega_o} \mathcal{I}^K - \alpha_r \rho^2. \quad (16)$$

Equations (3) through (16) are sufficient to describe the evolution of a pulse from its initial condition as it propagates through a material accounting for diffraction, dispersion, shock, Raman and Kerr effects as well as ionization. The ionization model itself includes multiphoton ionization, saturation, recombination (second-order), as well as avalanche and tunneling ionization. Currently the distinction between cascade or tunneling ionization is based on the value of the ionization cross-section σ_k . It is possible to include the roll-off from one to the other by making this parameter a function of intensity.

5.3 Modeling Codes

Here we describe the numerical model briefly and then discuss the two codes which implement it. The model itself is derived in detail in our paper [25].

The model describes the evolution of a radially symmetric pulse through a plane over the temporal coordinate at successively increasing z -locations. The numerical grid has transverse spatial coordinate r and a retarded temporal coordinate τ (the grid is traveling at the pulse group velocity). This grid exists at a particular location in the primary propagation direction and describes the radial and temporal variations of the pulse envelope. At each propagation step the algorithm transforms the transverse space-time description at the current location to the distribution at the next location in the propagation direction.

The over-arching numerical method is split-step (an operator splitting technique). See G. Strang [26] for an in-depth discussion of the mathematical underpinnings. An equation of the form

$$\partial_z A = LA + N(A)A \quad (17)$$

may be approximated rigorously by alternating solution of the following two equations

$$\partial_z A = LA \quad (18)$$

$$\partial_z A = N(A)A. \quad (19)$$

Solving each of these equations requires additional numerical methods.

We begin with a description of the initial pulse and solve Eq. (18) over a short step in the z -direction (the principal direction of propagation). In our code this is accomplished in the temporal frequency domain (making the dispersion operator algebraic) with a Crank-Nicolson (CN) finite difference method for the transverse spatial operator. After advancing the pulse via Eq. (18) the resulting pulse description is used as an initial condition for Eq. (19).

During the nonlinear step we first update the free-electron density by solving Eq. (15) or Eq. (16) via a Runge-Kutta method. The result is then used while numerically solving Eq. (19). This may, in some cases, be accomplished with a simple algebraic solution depending on the nonlinear operators active in the model. In the more general case a Runge-Kutta framework is used to integrate the equation over the same short z -step. This completes a single first-order z -direction step. Higher order operator splitting methods are also possible (see G. Strang [26]). However, we have only run first (as described above) and second order.

Matlab Code

The Matlab code base implements a radially symmetric model using first-order split step. The linear temporal operators (group velocity and third order dispersion) are solved algebraically in the frequency domain. Before transforming back to the time-domain a for-loop over frequency uses a Crank-Nicolson method with *arbitrary* operator order to update the linear diffraction operator (Laplacian). Once back in the time-domain the nonlinear step takes place.

When ionization is active a standard Matlab Runge-Kutta solver for moderately stiff differential equations is used to update the free-electron density. If only Kerr and ionization are active (no Raman effect) then we have a simple nonlinear interest equation that can be updated algebraically. This is also possible with just Kerr and Raman interactions if no ionization is modeled. A more general RK numerical integrator can be used by setting a flag. This more general integrator would be necessary if we desired to model Kerr, Raman, and ionization. It is not difficult to modify the code to do this but it has not been done yet. The Kerr, Raman, and ionizations models are parallelized with the Matlab parallel programming toolbox `parfor` command.

C++ Code

The C++ code is similar to the Matlab code with a few major differences. It is parallelized via MPI using the SAMRAI library. This makes it possible to run simulations on large clusters. We also use an adaptive mesh refinement methodology in order to adjust the mesh size based on the local sampling needs. The overall result is a significantly faster code capable of handling large memory problems. The ionization model uses a moderately stiff solver from the Sundial library. No Runge-Kutta method is available for solving the nonlinear step (only the simple exponential update). Both codes have been benchmarked successfully against each other and validated as described in section 5.4.

5.4 Validation

This section described the basic validation tests of both codes. Some of this validation (especially for the Matlab code) was performed under both this LDRD and [27]. Currently these data runs can be obtained from either the Matlab or C++ codes.

Basic Physics

In this section we discuss basic validation demonstrating propagation of optical disturbances exhibiting correct dispersive, diffractive, focal and nonlinear critical power characteristics. These validations were performed for the Matlab code under both this LDRD and a previous related LDRD (see Rambo [27]). The C++ code was primarily validated under this LDRD.

The Rayleigh range is the distance at which the beam radius has increased by a factor of $\sqrt{2}$ doubling the beam area. It is calculated as [28]

$$z_R = \frac{\pi w_o^2 n}{\lambda} \quad (20)$$

where w_o is the beam radius at the beam waist (location of smallest beam radius with a flat wave front). Here we define the field radius as the distance at which the field amplitude (not the intensity) is down by a factor of e^{-1} from its on axis value. One of our automated validation tests checks the Rayleigh range of propagated pulses. The plot on the left of Fig. 39 shows a comparison between a paraxial Gaussian pulse (see Yariv [28]) and a pulse with identical initial conditions propagated in our numerical codes.

Another characteristic of linear propagation is wavelength dispersion. If the variation of the propagation constant k (or beta in some developments) with angular frequency ω is a straight line through the origin ($k = \omega/c$ where c is the speed of light in the material) then we have no material dispersion. However, for real materials this is never the case. If we consider a pulse with frequency domain support contained near some carrier or central frequency ω_o we may understand the fundamental dependence of the propagation constant on frequency via a Taylor expansion. The first four terms of such an expansion are

$$k(\omega) = k(\omega_o) + k'(\omega - \omega_o) + \frac{1}{2}k''(\omega - \omega_o)^2 + \frac{1}{6}k'''(\omega - \omega_o)^3 \quad (21)$$

Here, $k(\omega_o)$ is the propagation constant (the value of the wavenumber evaluated at the center frequency). Siegman [29] demonstrates that for a gaussian pulse the phase velocity (apparent motion of the carrier frequency waves within the pulse envelope) is given by $v_p = \omega/k(\omega_o)$. The group velocity (motion of the gaussian pulse envelope) is given by $v_g = 1/k'(\omega_o)$. The remaining terms are the *group velocity dispersion* and *third order dispersion* respectively.

The dispersion length is defined as the distance at which the temporal extent of an unchirped pulse increases by a factor of $\sqrt{2}$. Siegman (page 356) shows that this distance is given by

$$z_D = \tau_o^2 / (4 * \ln(2)) * k'' \quad (22)$$

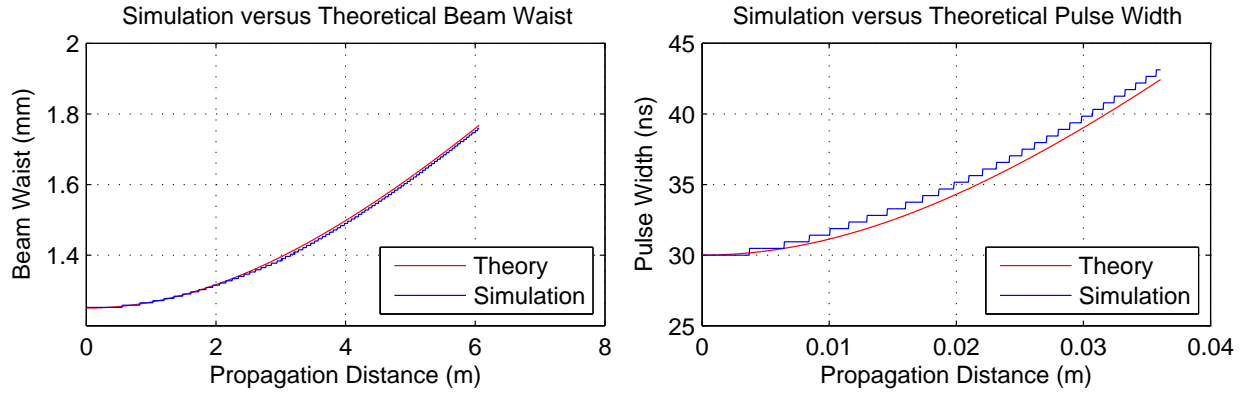


Figure 39. The plot on the left shows a comparison between the theoretically expected FWHM (full width half max) measurement of a Gaussian beam and the width of the beam as a function of propagation distance obtained in the simulation code. The e^{-1} -amplitude radius is 1.5 mm. The center wavelength is 810 nm. The plot on the right hand side shows a comparison between the theoretical and computed dispersion of a pulse with identical center wavelength and radius having a 30 ns FWHM intensity temporal extent. The stair-step effect is a result of coarse sampling in the simulation in the propagation direction. The simulation medium is air. See also [27].

where τ_o is the initial pulse width. Automated testing of the code verifies this property of the simulation. The plot on the right hand side of Fig. 39 shows a direct comparison between the temporal length of an analytical pulse (see Siegman [29] or Yariv [28]) and one propagated numerically by the codes.

The equation for critical power in a Gaussian beam may be given as

$$P_{\text{cr}} = \frac{\lambda^2}{2\pi n_o n_2}. \quad (23)$$

or

$$P_{\text{cr,M}} = \frac{3.77\lambda^2}{8\pi n_o n_2} \quad (24)$$

depending on the definition of confinement (see Diels [30] and Couairon [18] and Marburger [31]). Figure 40 shows that confinement of the beam and clamping of intensity occurs at the expected input power. We may also compute an expected collapse distance per Marburger [31]. Using the linear Rayleigh length described in Eq. (20) and the critical power defined in Eq. (24) we may compute

$$L_c = \frac{0.367z_R}{\left(\sqrt{P_{\text{in}}/P_{\text{cr}}} - 0.852\right)^2 - 0.0219} \quad (25)$$

The codes also correctly demonstrate the above described collapse distance.

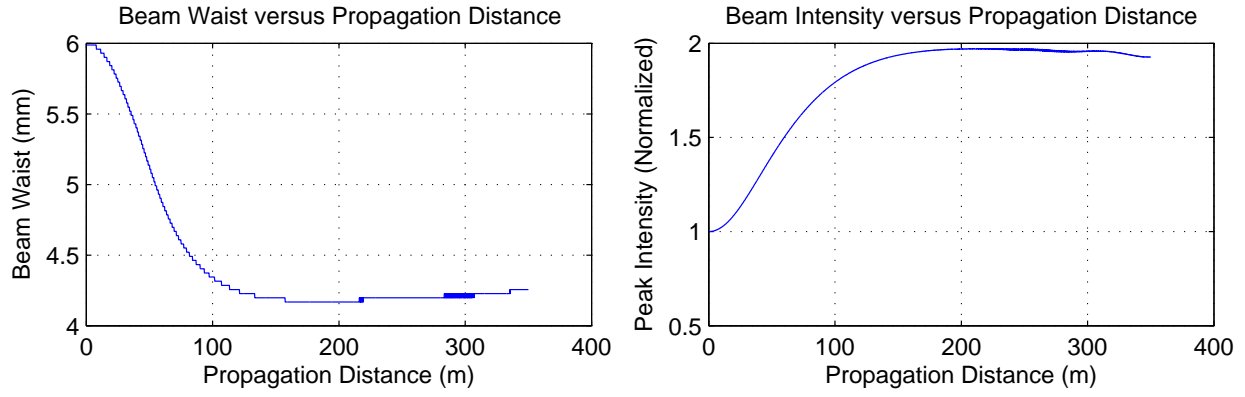


Figure 40. The left and right plots show beam radius and intensity as a function of propagation distance over approximately 300m in air. The center wavelength is 1024nm. The initial e^{-1} -amplitude radius is 6mm. The input was slightly below critical power for a Gaussian beam as given in equation (23). Here $n_2 = 4 \times 10^{-23} \text{ m}^2/\text{W}$. Clearly the beam is confined nearly indefinitely (we actually used a little less than critical power) due to the balancing of Kerr nonlinearity and diffraction. The group velocity dispersion is $9 \times 10^{-15} \text{ s}^2/\text{m}$ and the refractive index is unity. See also [27].

Literature Comparison

Here we describe comparisons made with the literature for both the Matlab and C++ codes. Again the comparisons were funded by both this LDRD and [27]. Figure 41 shows the maximum temporal (upper) and radial (lower) intensities in the pulse as a function of propagation distance obtained via our codes compared to the published results by Mlejnek [32]. Figure 42 shows a comparison between a pulse 200fs length pulse propagated with Kerr and ionization a distance of 2.5 cm by our codes and a published result for a simulation by Mlejnek in the same paper [32]. The model parameters for the data shown in Figures 41 and 42 are

$$\begin{aligned}
 \alpha &= 7.0 \times 10^{-13} \text{ m}^{-3}/\text{s} \\
 \beta_K &= 3.5 \times 10^{-123} \text{ m}^{13}/\text{W}^7 \\
 K &= 8 \\
 U_i &= 15.76 \text{ J} \\
 \tau_c &= 1.9 \times 10^{-13} \text{ s} \\
 \rho_{\text{at}} &= 2.7 \times 10^{25} \text{ m}^{-3}
 \end{aligned}$$

Figures 43 and 44 are comparisons with Zozulya[33] and their simulation results. The model

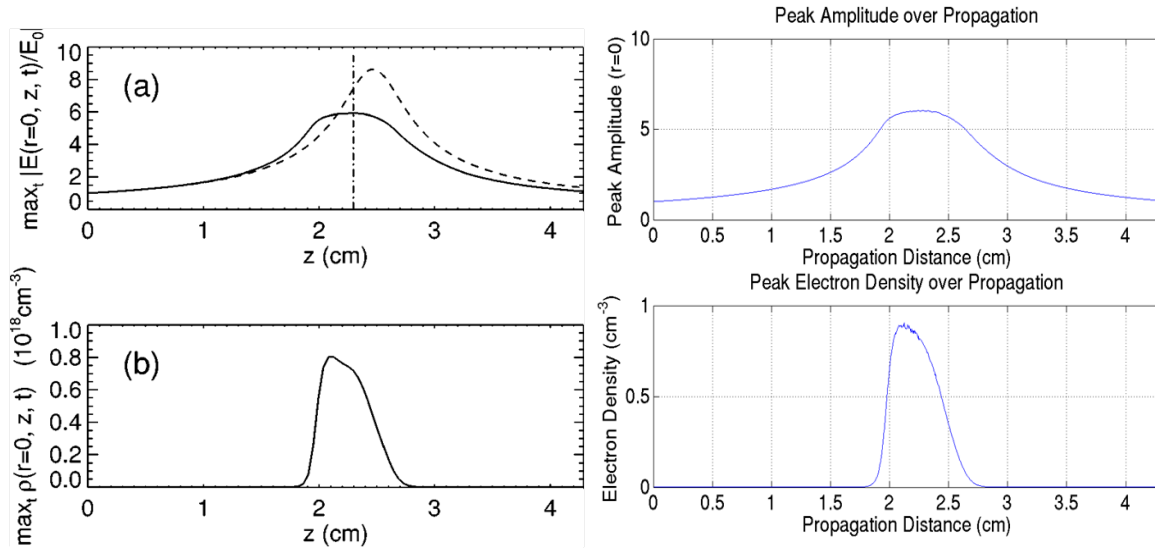


Figure 41. The left figure comes from a paper by Mlejnek[32]. Mlejnek's simulation does not include shock or Raman. It does have instantaneous Kerr and ionization, however. Our simulation using the same model is shown at right. The e^{-1} -amplitude radius is 0.2mm. The temporal FWHM intensity extent of the pulse is 200fs. The center wavelength is 586nm. The focus is at 2.5cm. Other relevant simulation parameters are $n_2 = 4.9 \times 10^{-23} \text{ m}^2/\text{W}$ and $\text{GVD} = 2.6 \times 10^{-29} \text{ s}^2/\text{m}$. Excellent agreement is observed. See also [27].

parameters for the comparisons in Figures 43, 44, and 45 are

$$\begin{aligned}
 n_o &= 1.45 \\
 n_2 &= 2.5 \times 10^{-20} \text{ m}^2/\text{W} \\
 \text{GVD} &= 3.6 \times 10^{-26} \text{ s}^2/\text{m} \\
 \gamma &= 0.15 \\
 \tau_R &= 50 \times 10^{-15} \text{ s} \\
 \omega_R &= 84 \times 10^{-12} \text{ radians/s}
 \end{aligned}$$

These figures show very good agreement between the our numerical simulation and the published simulation results. It should also be noted that Zozulya's paper [33] makes a favorable comparison with laboratory data (not shown here).

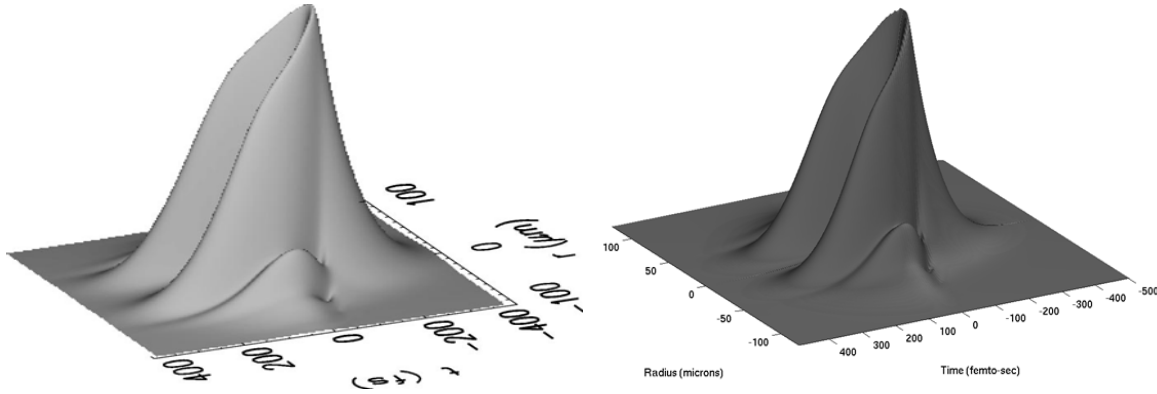


Figure 42. The left figure comes from a paper by Mlejnek[32]. Mlejnek’s simulation does not include shock or Raman. It does have instantaneous Kerr and ionization, however. Our simulation using the same model is shown at right. The e^{-1} -amplitude radius is 0.2mm. The temporal FWHM intensity extent of the pulse is 200fs. The center wavelength is 586nm. The focus is at 2.5cm. Other relevant simulation parameters are $n_2 = 4.9 \times 10^{-23} \text{ m}^2/\text{W}$ and $\text{GVD} = 2.6 \times 10^{-29} \text{ s}^2/\text{m}$. The propagation distance is 2.3 cm. Excellent agreement is observed. See also [27].

Advances in General Modeling Understanding

We used the “common” methodology for casting the physical problem described in section 5.2 into a numerical model and were able to match not only relevant papers from the literature but also basic physics calculations. The specifics of the numerical model are discussed in [25] (there is also an overview in [27]).

In conducting numerous modeling investigation of propagation we found that longer distance propagation and propagation starting with a converging beam proved more difficult. In many cases the pulse would propagate correctly until it was fairly tightly confined near the center of the coordinate system. The error then increased rapidly. This difficulty was traced to the linear (as opposed to nonlinear) operator. Wave propagation is linear and shift invariant. When we cast the problem into a radially symmetric framework the shift invariant nature is lost. We have a different operator at every radial location. Comparing the finite difference operator at a given location against the continuous (exact) operator we see that the disparity increases as the radial coordinate decreases. The error represents itself as phase error in the operator at high frequencies (larger near $r = 0$). We believe this is why the pulse begins to fall apart for tightly confined pulses. Increasing the sampling rate helps but this also increases the error due to round-off eventually. Increasing the order of the finite-difference operator helps until (for very high orders) the round-off error begins to increase. This appears to be a fundamental limitation of the finite difference method when using radially symmetric models.

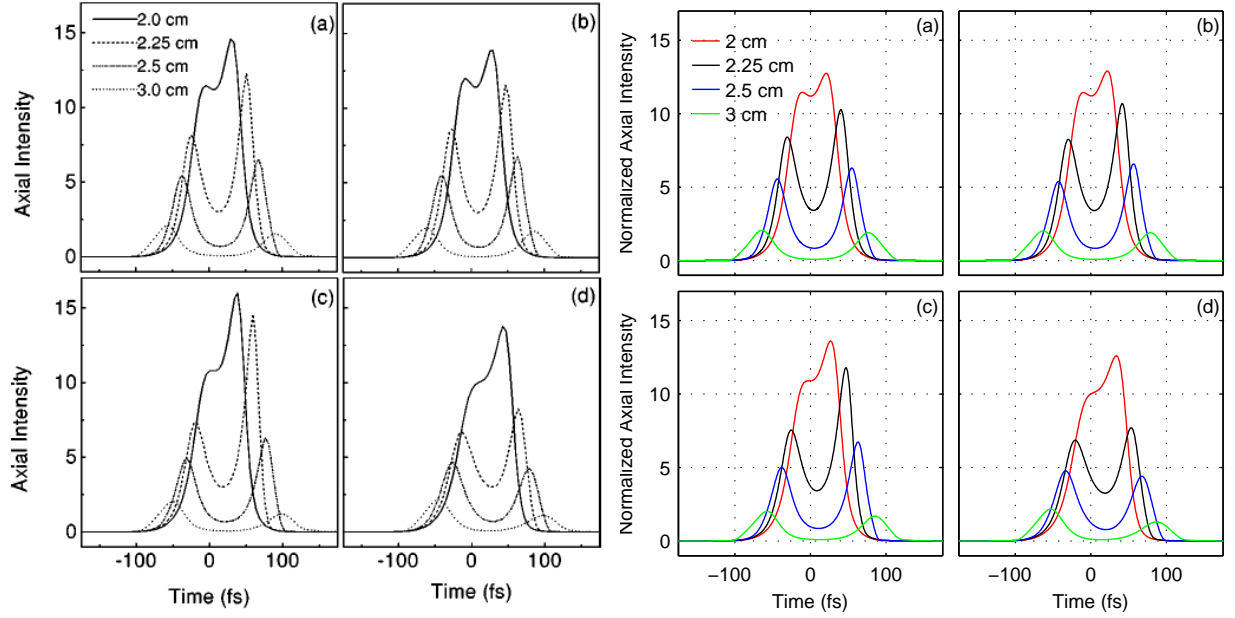


Figure 43. Calculated on-axis intensity profile (see Zozulya[33] figure 5). The propagation is in fused silica. Each plot considers the following effects (a) Non-linear shock. (b) Linear shock. (c) Both linear and non-linear shock. and (d) Both shock terms and Raman effects. The center wavelength is 800nm. The initial e^{-1} -amplitude radius is $59.45\mu\text{m}$. The temporal FWHM intensity extent of the pulse is 90fs. The input intensity is $85\text{GW}/\text{cm}^2$. Material parameters are described in the text. See also [27].

Possible solutions are moving to a $(3D + 1)$ code so that the operator becomes shift invariant again and adequate sampling and operator order are no longer a functions of spatial coordinates. Also, finite element methods may prove useful. When in $(3D + 1)$ Fourier based propagators may also be helpful (their principal drawback is that they enforce periodic boundary conditions).

Another aspect of using a radially symmetric model became apparent as well. Diffraction, self-focusing, and ionization effects can balance one another to create a *single* channeled filament. However, there is a limit on the amount of power in the pulse that diffraction and ionization defocusing can balance. Eventually, either fully $(3D + 1)$ models must be used so that multiple filaments are allowed or the pulse will collapse (this is, of course, already known). However, leaving out the actual physics of multiple filament formation presents a difficulty when trying to understand the reason for the collapse of a numerical run – it may be mathematical (a result of an inadequate number of filaments) or it may be numerical (inherent quality of the framework).

We also spent a fair amount of effort understanding the various trade-offs involved in the numerical implementation. The code itself allowed an arbitrary order for finite-difference operators to be specified at run-time. It is also capable of using different numerical methods for obtaining the

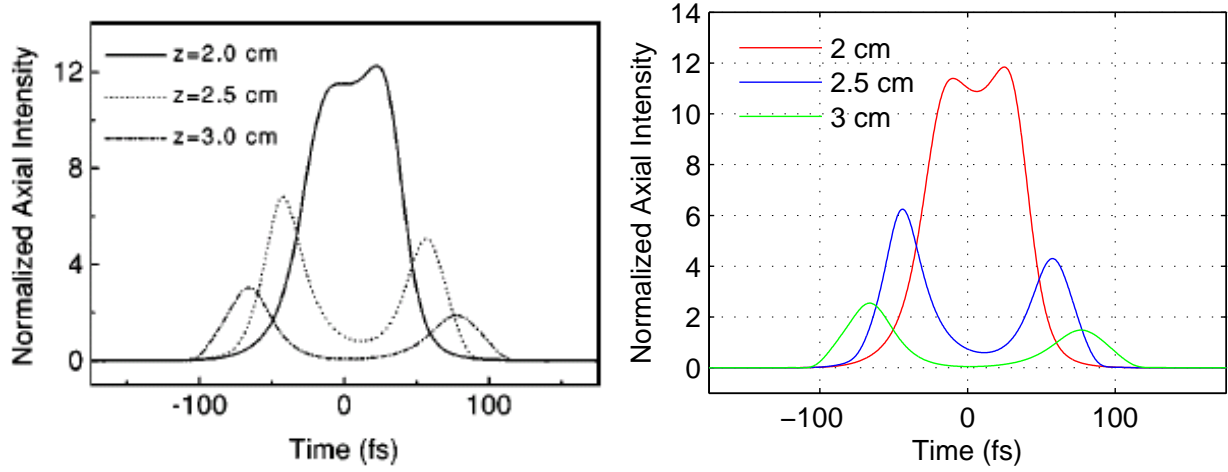


Figure 44. The figure on the left is taken from Zozulya[33] figure 3 demonstrating Raman pulse splitting effects. It shows the peak on-axis intensity normalized by the input intensity. The initial pulse parameters are as given in figure 43. Material parameters are described in the text. See also [27].

finite-difference coefficients at the beginning of the run. We were able to study the effect of altering the method of obtaining the coefficients. This is particularly important in the AMR (Adaptive Mesh Refinement) codes which necessarily solve for the coefficients during the run at each step (after mesh adjustment). The results may be found in detail in [25].

We also studied the effect of using a pre-conditioner during the linear solve on accuracy and speed of the solution. Figure 45 shows that even over short distances the pre-conditioner can change the amplitude of the pulse. Round-off and truncation in the propagator and their effect on accuracy and how they manifest themselves in the solution were also studied. These results are also discussed in [25].

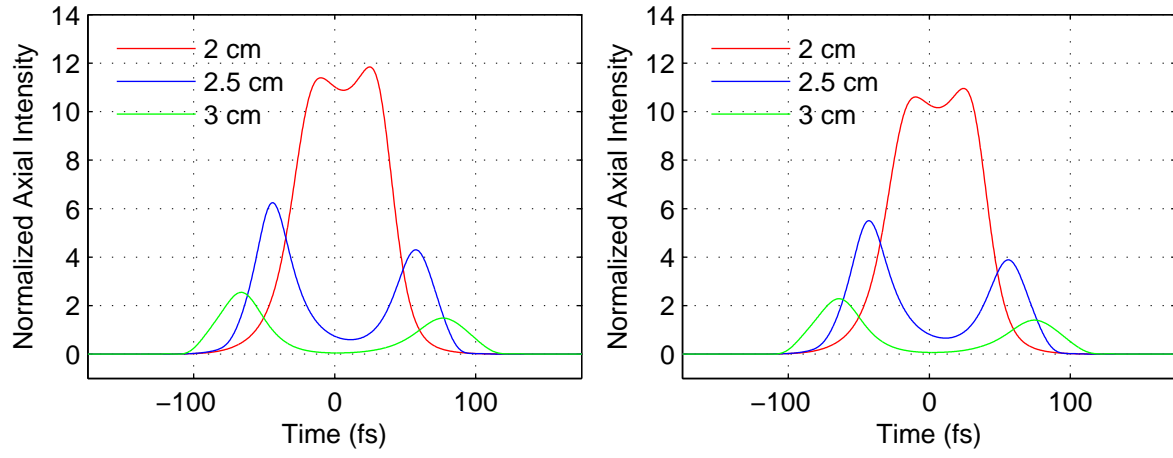


Figure 45. Compare Zozulya[33] figure 3. It shows the peak on-axis intensity normalized by the input intensity. No preconditioner was used in the linear solver for the data on the right. On the left a preconditioner was used. After only a few millimeters of propagation differences in the pulse envelope amplitudes are apparent. The initial pulse parameters are as given in figure 43. Parameters are described in the text. See also [27].

5.5 Symbols

Symbol	Units	Description
$\epsilon_o = 8.854 \times 10^{-12}$	$\text{F} \cdot \text{m}^{-1}$	Permittivity of free space
$\mu_o = 4\pi \times 10^{-7}$	$\text{H} \cdot \text{m}^{-1}$	Permeability of free space
$e = 1.60217657 \times 10^{-19}$	C	Magnitude of the charge carried by an electron
$c = 2.99792458 \times 10^8$	$\text{m} \cdot \text{s}^{-1}$	Speed of light <i>in vacuo</i>
\mathcal{E}	$\text{V} \cdot \text{m}^{-1}$	Electric field envelope
ρ	$\text{C} \cdot \text{m}^{-3}$	Electric charge density
t	s	Time coordinate variable
ω	$\text{rad} \cdot \text{s}^{-1}$	Angular frequency
$k(\omega)$	m^{-1}	Wavenumber as a function of angular frequency
\mathbf{r}	m	Coordinate vector (x, y, z)
k'	$\text{s} \cdot \text{m}^{-1}$	First order coefficient in Taylor series expansion of $k(\omega)$
k''	$\text{s}^2 \cdot \text{m}^{-1}$	Second order coefficient in Taylor series expansion of $k(\omega)$
k'''	$\text{s}^3 \cdot \text{m}^{-1}$	Third order coefficient in Taylor series expansion of $k(\omega)$
$k^{(m)}$	$\text{s}^m \cdot \text{m}^{-1}$	m th order coefficient in Taylor series expansion of $k(\omega)$
ω_o	$\text{rad} \cdot \text{s}^{-1}$	Pulse center frequency
x, y	m	Transverse spatial coordinate variables
z	m	Longitudinal spatial coordinate variable
τ	s	Retarded temporal coordinate variable
\mathcal{N}_p	$\text{C} \cdot \text{m}^{-2}$	Envelope of total nonlinear material response
T, S	—	Shock operators
n_o	—	Background refractive index of material
k_o	m^{-1}	Central wavenumber
\mathcal{I}	$\text{W} \cdot \text{m}^{-2}$	Scalar envelope intensity
n_2	$\text{m}^2 \cdot \text{W}^{-1}$	Nonlinear refractive index of material
\mathcal{N}_k	m^{-1}	Envelope Kerr operator
\mathcal{N}_{kr}	m^{-1}	Envelope Kerr-Raman operator
\mathcal{Q}_R	$\text{W} \cdot \text{m}^{-2}$	Molecular Raman response
γ	s^{-1}	Molecular damping rate (Raman)
ω_R	$\text{rad} \cdot \text{s}^{-1}$	Molecular Raman frequency
$R(t)$	—	Molecular impulse response (Raman)
α	—	Raman scattering contribution to Kerr-Raman terms
ρ	m^{-3}	Electron number density
K	—	Number of electrons required to ionize atom
α_r	$\text{m}^3 \cdot \text{s}^{-1}$	Ionization recombination loss coefficient
ρ_{nt}	m^{-3}	Number density of neutral atoms
σ_k	$\text{W}^K \cdot \text{m}^{-2K} \cdot \text{s}^{-1}$	Ionization cross-section for K -photon MPI processes
U_i	J	Energy required to free an electron (ionization energy)
\hbar	$\text{J} \cdot \text{s}$	Planck's constant (reduced)

Symbol	Units	Description
σ	m^2	Avalanche ionization rate coefficient
ρ_c	m^{-3}	Critical plasma number density (plasma is opaque for $\rho > \rho_c$)
β_K	$\text{J} \cdot \text{W}^K \cdot \text{m}^{-2K-3} \cdot \text{s}^{-1}$	Ionization rate coefficient (MPI)
\mathcal{N}_{pls}	$\text{C} \cdot \text{m}^{-2}$	Plasma current equivalent polarization operator
τ_c	s	Electron collision or relaxation time
P_{cr}	$\text{W} \cdot \text{m}^{-2}$	Critical power for filamentation ([30])
$P_{\text{cr,Z}}$	$\text{W} \cdot \text{m}^{-2}$	Critical power for filamentation ([33], [30])
$P_{\text{cr,M}}$	$\text{W} \cdot \text{m}^{-2}$	Critical power for filamentation ([31])

6 Railgap Switch Modeling

This section describes the results of simulations of the railgap switch which utilizes gases such as SF_6/Ar mixture and dry air. The triggered switch is simulated by the PIC code LSP [34] using chemistry models for SF_6 , Ar, and dry air developed by Voss Scientific. We first describe the circuit model used in the railgap simulations which is used to perform an initial static field solution to establish the fields in the simulation space. This in turn saves on runtime, as we need not wait for initial field transients to die down. After that we lay out the results of 2D Cartesian railgap simulations using an SF_6/Ar mixture, for which we find a switch impedance on the order of $1\ \Omega$ for a full-length railgap switch. We then describe the results for 2D and 3D railgap simulations using dry air. In 2D, we find a switch resistance on the order of $5\ \Omega$, and electron density not exceeding 10^{16} cm^{-3} . It is later shown, that in a full 3D simulation, pinching of the current channel will lead to filaments of similar plasma densities.

We also describe the results from some simple test problems in which we investigate the possibility of filamentary structures in 3D geometries. For a simple “railgap-like” switch using pure N_2 at a high volume (above the avalanche threshold) we obtain high plasma density and strong plasma density variations close to the cathode surface. Small filaments of width $\approx 1\text{ mm}$ and relatively uniform spacing of 1-2 mm are observed. However the plasma density along the anode surface is mostly uniform. Finally we present the results of a 3D field solution for the full railgap switch, and investigate the severity of field enhancements.

6.1 Simulated Circuit Model

The circuits attached to the anode (A) and cathode (K) are shown schematically in Fig. 46. The circuit parameters are as follows: The capacitance $C = 80\text{ nF}$, the inductance $L = 60\text{ nH}$, and the resistance $R_L = 2.1\ \Omega$. All of the transmission line segments are one time step long and are matched to the characteristic impedance of the simulation grid input ports (see Fig. 47 for the positions of the grid connections). Note that these circuit element values assume that the railgap is 12 cm long in virtual z-direction (out of the page in Fig. 47). The two capacitors are initially charged to a voltage of $\pm 100\text{ kV}$ as shown in the figure.

The circuits which are attached to the input trigger ports are shown in Fig. 48. The transmission line segments are again one time step long and matched to the impedance of the simulation ports. The second transmission segment is terminated in its own impedance and an incoming wave from an infinite source is fed into the simulation through the circuit. The lumped resistor, $R = 500\ \Omega$ (for a switch of length 12 cm in the virtual direction), is used to suppress leakage current through the trigger.

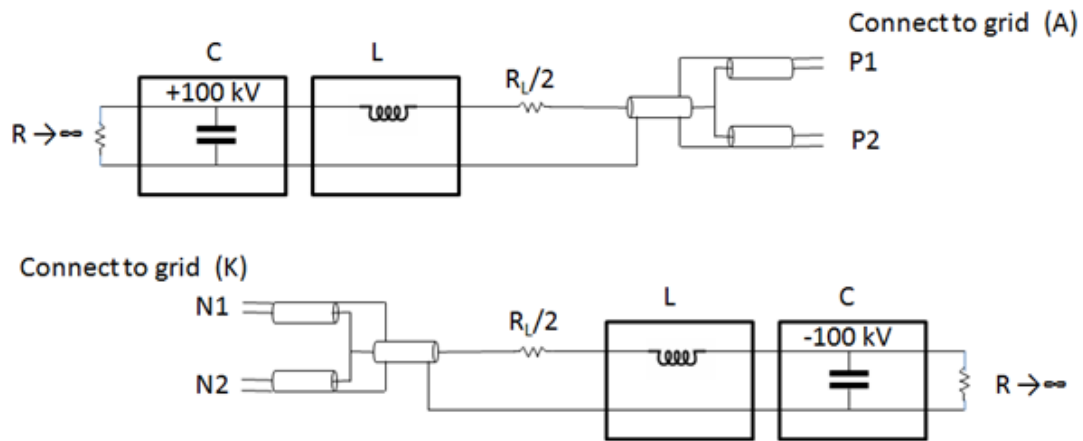


Figure 46. Simplified circuit model for railgap simulations. The grid connection to the anode and cathode are shown on the top and bottom, respectively. The positions of the grid connections are shown in Fig. 47.

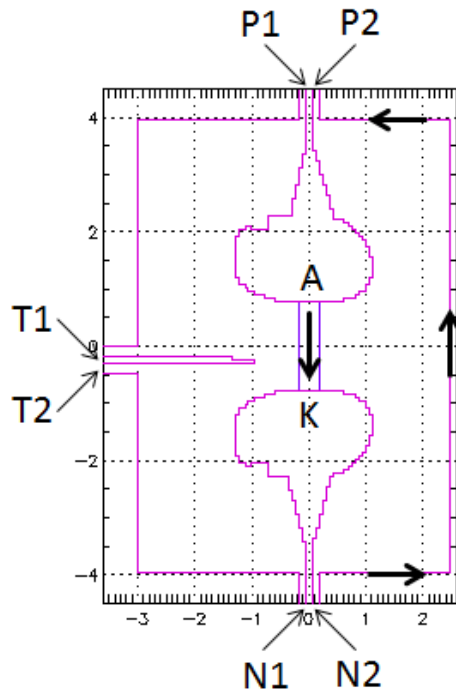


Figure 47. Connection of circuits to simulation domain. Purple box denotes area of conducting volume model used for the simulation results shown in Fig. 50. The thick black arrows show the current path when the switch is closed.

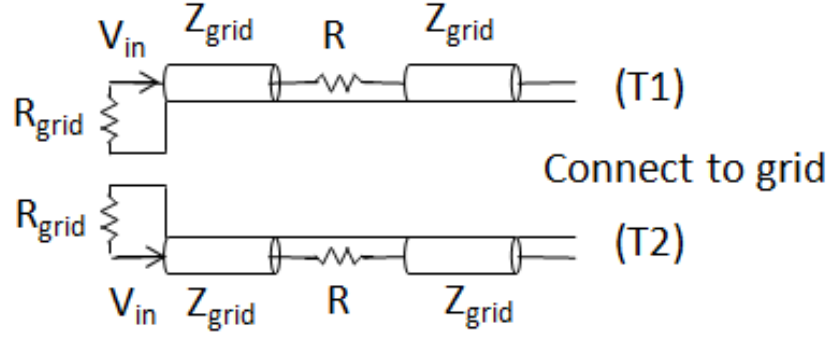


Figure 48. The trigger circuit used for railgap simulations. The positions of the grid connections are shown in Fig. 47.

Scaling of circuit parameters for an arbitrary length in the z-direction

The circuit parameters quoted above are intended for use in a switch with a fixed length in the z-direction. We now consider the scaling of the circuit parameters with the railgap length in the z direction, l . This is necessary to properly set up 2D-xy Cartesian simulations which assume a 1 cm length in z, and for 3D simulations with periodic boundaries in z, in which the full 12 cm length is not included in the simulation space.

Since the magnitude of the electric field strength needs to be the same regardless of length, all voltages are independent of l . Capacitances scale linearly with l , while resistors, inductors, and transmission line impedances (parallel-plate transmission lines in 2D and 3D periodic) all scale as l^{-1} . This scaling also preserves all the circuit timescales.

For the full 3D switch we have: $l = 12$ cm, $C = 80$ nF, $L = 60$ nH, and $R_L = 2.1 \Omega$. For a 2D simulation ($l = 1$ cm in virtual direction) the circuit parameters are adjusted as follows: $C = 80/12$ nF, $L = 60 \times 12$ nH, and $R_L = 2.1 \times 12 \Omega$, with the same scaling of the resistors in the trigger circuits. The impedance of input ports and matching (parallel-plate) transmission lines are all calculated using $l = 1$ cm.

The geometry of the 2D Cartesian railgap simulation is shown in Fig. 47. Also shown in the figure is the outline of a volumetric conducting region, which is given a finite conductivity which corresponds to a resistance of $1/12 \Omega$ (1Ω for the full 12 cm switch) between the anode and cathode. Figure 49 shows the anode, cathode, and trigger voltages (all with respect to ground) as a function of time.

We note that we have used an initial static field solve. With this technique, the initial fields are initialized into the simulation grid, and there is no need to wait for transients to die down. The initial incoming trigger pulse, $V_{in}(t)$ starts out at -15 kV. This results in a total trigger voltage of -30 kV due the open circuit configuration. This value is used as a background trigger voltage. Since the needle is closer to the cathode, by holding the needle at ≈ -30 kV, this should help to avoid field perturbations due to the presence of the trigger needle in the AK gap. The actual trigger

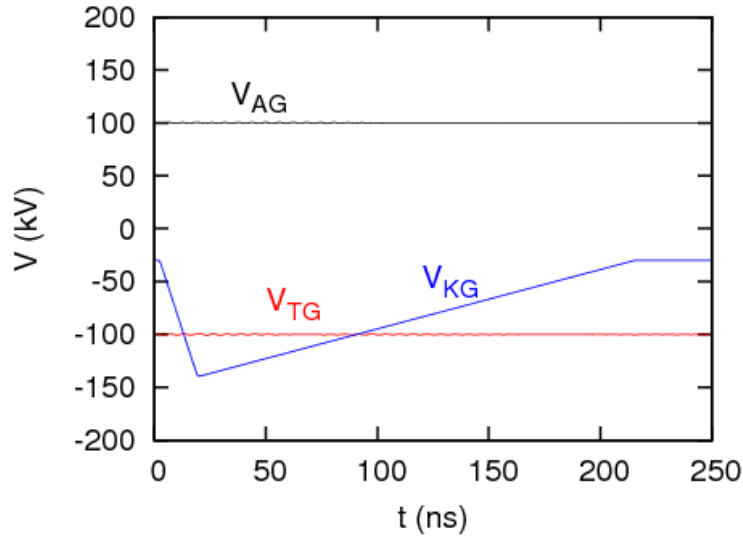


Figure 49. Voltages on the anode V_{AG} , cathode V_{KG} , and trigger V_{TG} (all with respect to ground) for the open-circuited railgap.

pulse begins at $t = 2$ ns. Over a 15 ns linear ramp, V_{in} increases in amplitude from -15 to -70 kV. After 35 ns, the trigger pulse slowly drops back to -15 kV (linearly over ≈ 200 ns). Figure 50 shows the discharge of the capacitors and the switch current when the $1/12 \Omega$ resistor is placed between the anode and cathode. There is no gas present in these initial simulations. For this imposed switch resistance, the capacitors in the pulsed power circuits discharge on a time scale of a few hundred ns.

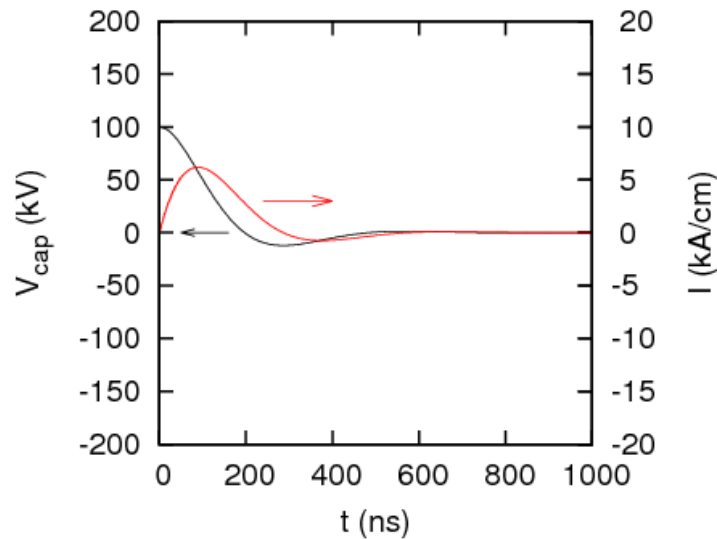


Figure 50. Discharge of capacitor by $1/12 \Omega$ resistor placed between cathode and anode in 2D Cartesian railgap simulation.

6.2 2D Simulations of 85% SF₆ and 15% Ar mixture

We now describe results from 2D Cartesian simulations of a railgap switch with a working gas of 85% SF₆ and 15% Ar (by number). The circuit parameters (i.e. voltages, capacitances, etc.) are set to the values given in the previous section (properly scaled to account for the 1 cm virtual length in the z-direction). Using a new gas mixture requires that we first determine the critical field for avalanche breakdown. The gas density must be set high enough to preclude the possibility of self-breaking by the switch.

To determine the critical field for the 85% SF₆ and 15% Ar gas mixture, we perform simple one cell swarm simulations in which an ensemble of stationary particles is allowed to avalanche in an imposed electric field. The chemistry models for SF₆ and Ar were described in great detail in a previous paper [35]. The particles are not allowed to feed back on the fields (low density approximation) and for simplicity we disable photon generation and transport. In the weakly-ionized approximation (and in the absence of any three-body processes) the transport coefficients, including normalized effective ionization rate, are functions only of E/n_n , where E is the electric field strength and n_n is the neutral gas density. The ionization rate α , is the rate of exponential electron density growth $n_e \propto e^{\alpha t}$.

For $\alpha > 0$, ionization dominates attachment and avalanche breakdown may occur in the applied field. For $\alpha < 0$ attachment dominates and electron density decays away with time. To avoid self-breaking, the fields and gas density used in the railgap switch must be chosen so that the gas is attachment dominated before the application of the trigger pulse. The normalized ionization rate given by $\alpha/(v_D n_n)$, with units of area, where v_D is the drift velocity, which is a function only of E/n_n is shown in Fig. 51 for a series of swarm simulations for 85% SF₆ and 15% Ar gas mixture.

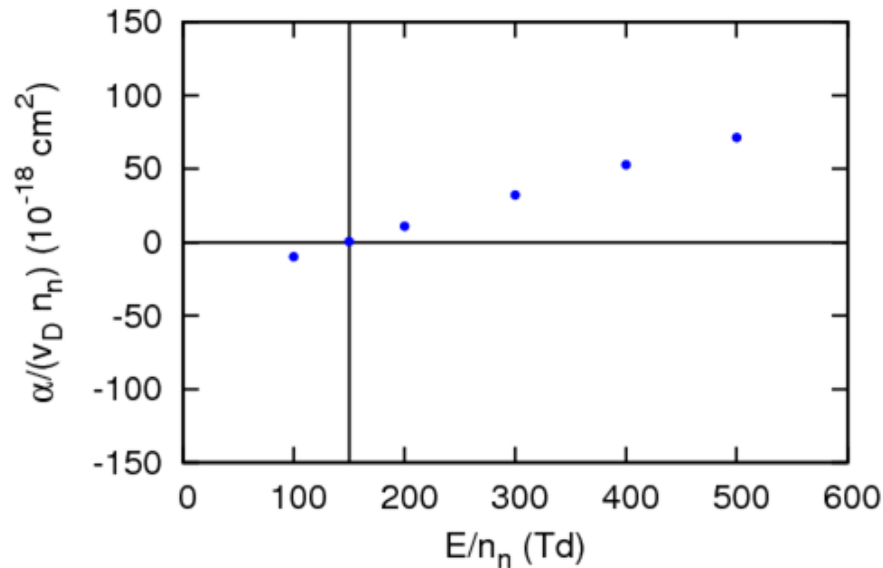


Figure 51. Normalized effective ionization coefficient for 85% SF₆ and 15% Ar mixture obtained from swarm simulations.

From Fig. 51, we see that the critical value of E/n_n , where $\alpha = 0$, for the mixture is about 150 Td (1 Td = 10^{17} Vcm²). The initial field magnitudes in the railgap, before the trigger pulse is applied, are on the order of 125 kV/cm (this is actually the field magnitude midway between the AK gap). At this field value a density of 8×10^{19} cm⁻³ (85% SF₆, 15% Ar), or a pressure of about 3 atm, is necessary to hold off avalanche ionization. So we use this as the gas density in railgap simulations for this mixture.

The geometry of the 2D railgap simulations is shown in Fig. 47. The conducting volume model shown in the figure is, of course, removed for the full simulations with gas. A uniform grid with $\Delta x = \Delta y = 0.06$ cm is used, along with a time step of $\Delta t = 5.6 \times 10^{-5}$ ns, which is set by the electron-neutral time step. Plasma is generated by allowing electron space-charge limited emission from the trigger tip and cathode surface. Emission is delayed for 5 ns, to avoid generating large numbers of particles before the conditions for electron avalanche are reached. History plots from the simulation are shown in Fig. 52. Snapshots of electron density contours are shown in Fig. 53- 55. Figure 56 shows the late time electron number density and current density. Note: In performing PIC Monte Carlo simulations a general rule of thumb is to keep the time step about $0.1\nu^{-1}$, where ν is the maximum electron-neutral collision frequency. In the interest of faster runtimes we have relaxed the time step constraint by a factor of 2 or 3 in the railgap simulations.

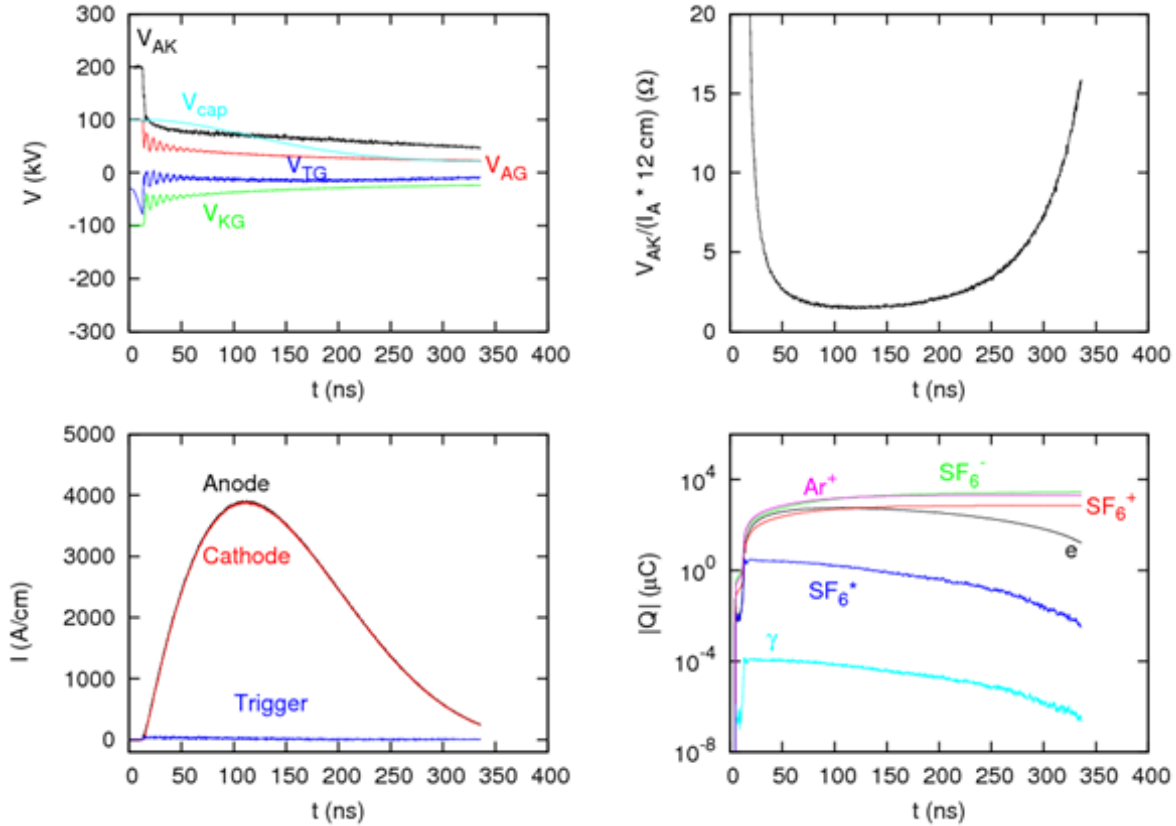


Figure 52. History plots for a 2D railgap simulation with 85% SF₆ and 15% Ar mixture.

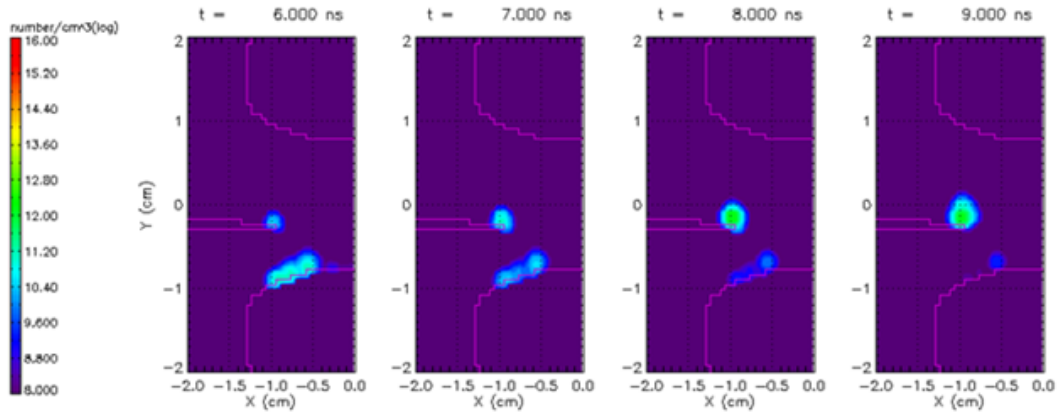


Figure 53. 2D railgap simulation for SF₆/Ar mixture. Electron density contours. Avalanche and early streamer propagation.

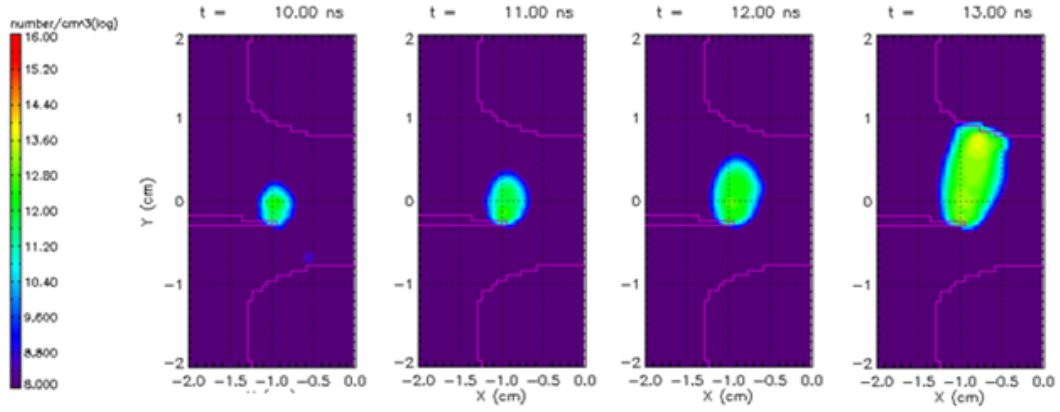


Figure 54. 2D railgap simulation for SF₆/Ar mixture. Electron density contours. Streamer propagation and connection from trigger to anode.

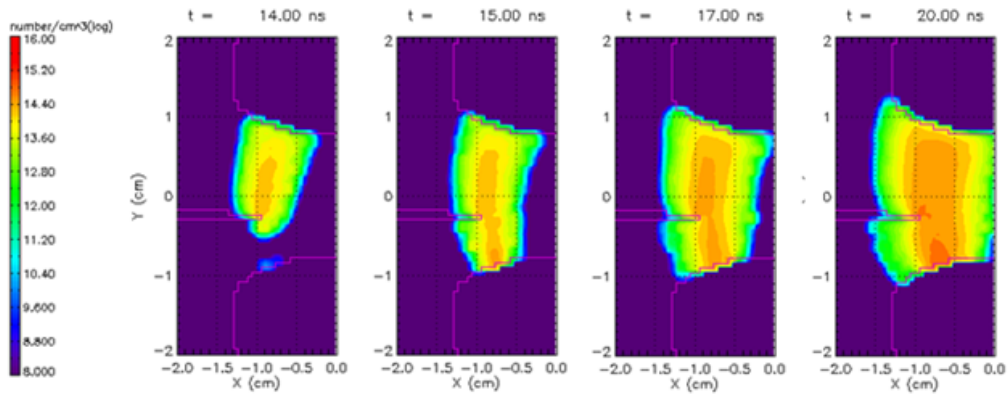


Figure 55. 2D railgap simulation for SF₆/Ar mixture. Electron density contours. Evolution of current channel.

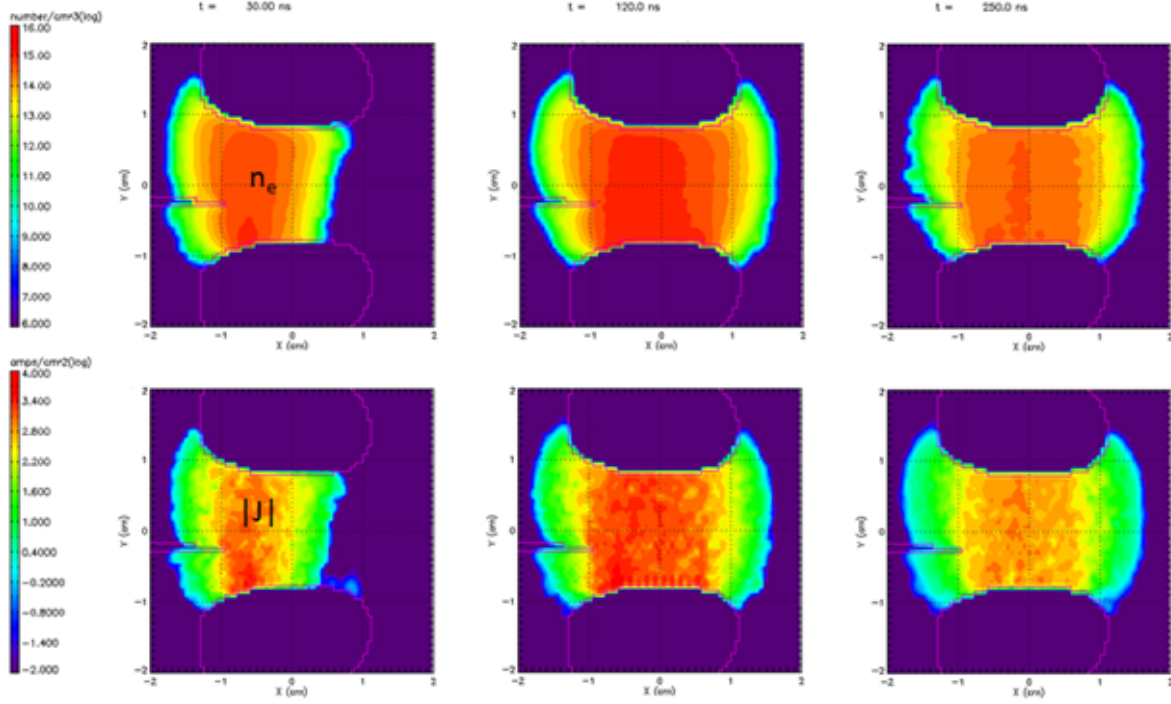


Figure 56. 2D railgap simulation for SF₆/Ar mixture. Electron density and current amplitude contours illustrate the time evolution of the current channel.

Various voltage measurements are shown as a function of time in the top left of Fig. 52. The simulation has been run out to ≈ 300 ns, at which time most of the voltage on the capacitors has been discharged. At early times the trigger voltage drops from -30 kV linearly, this causes the fields in the anode-trigger (AT) gap to increase, and the fields in the trigger-cathode (TK) gap to drop. This allows avalanche formation and streamer propagation from the tip of the trigger to the anode surface. The electron avalanche at the streamer tip, which begins at $t \approx 8$ ns, and the beginning of streamer propagation towards the anode can be seen in the electron density contours in Fig. 53. The streamer connects with the anode between 12 and 13 ns, as seen in Fig. 54. At that point the trigger potential begins to float up closer to the anode potential, which increases the fields in the TK gap and allows a streamer to propagate from the cathode to the trigger. This connection occurs at about $t \approx 15$ ns (see Fig. 55). At this point there is a full current path between the anode and cathode and current begins to flow. This can be seen in the bottom left of Fig. 52, which shows the current (per unit length in the virtual direction) flowing into the anode, and out of the cathode and trigger. There is negligible current through the trigger due to the large resistor added to the trigger circuit. The current rises up to a peak value of ≈ 4000 A/cm (corresponding to 32 kA for a full 12 cm long switch), and the capacitor is discharged on a time-scale of a few hundred ns. The approximate switch resistance is shown in the top right of Fig. 52. This trace is given by the ratio of the AK gap voltage and the anode current per unit length times the 12 cm length of the actual 3D switch, and results in a minimum resistance on the order of 1Ω . The total charge of each particle species is shown in the bottom right of Fig. 52. As expected, the switch resistance is roughly inversely proportional to the amount of electron charge. The electron charge begins to drop at late times, causing the switch resistance to increase. This can also be seen in Fig. 56 which shows the

time evolution of the electron number density and current density in the AK gap. After the initial connection through the trigger needle, the electron density spreads out to cover the entire AK gap which helps to minimize the resistance. At later times, however, as the voltage on the capacitor begins to drop. The fields in the AK gap drop as well, leading to more electron attachment and diminished resistance.

Using snapshots of electron density contours such as those shown in Fig. 53 and Fig. 54, we can estimate the streamer speed in trigger-anode gap. The distance of the shortest path from the trigger to the anode is 1.1 cm. We measure the distance of the streamer tip from the trigger needle at 1 ns increments from 8 to 12 ns and calculate approximate streamer speeds at $t = 8.5, 9.5, 10.5$, and 11.5 ns. The streamer speed varies from 0.03 cm/ns at 8.5 ns, up to 0.2 cm/ns at 11.5 ns, with the speed roughly increasing linearly in time with an acceleration of 0.04 cm/ns^2 . A uniform streamer tip acceleration in this time window is reasonable since the trigger pulse voltage increases linearly also up to $t = 17$ ns. The connection between the cathode and trigger is too rapid to allow a good estimate of the streamer velocity in this gap. Due to their lengthy runtimes, it was decided not to perform 3D simulations with the SF₆/Ar mixture. Instead we concentrated our efforts on railgap simulations using dry air as the working gas. These results are discussed in the next section.

6.3 Particle Based Chemistry Model for Air

Since dry air will be our preferred gas for switch operation we would like to explain the air chemistry model used for simulation in more detail. For the 2D and 3D switch simulations we have used the hybrid PIC code LSP [34]. Both electron and ion macro-particles are fully kinetic. Collisions and reactions between particle species are modeled using a PIC Monte Carlo treatment using an 18 species air chemistry model. The included species are: $e, N_2, O_2, Ar, N_2^+, O_2^+, Ar^+, N, N^{4+}, O^{2-}, O, O^-, O^{4+}, NO^+, N^+, O^+, \gamma$, and N_2^* , where N_2^* is a metastable excited state of N_2 .

Electron-neutral scattering including elastic and inelastic collisions (e.g. electronic and rotational excitations) are included along with electron impact ionization. We also included electron attachment channels, such as the dissociative reaction



It is the inclusion of such reactions that allows our air chemistry model to behave as an electrophilic gas at low values of E/n_n , where n_n is the neutral density. Other reactions include charge exchange, the formation and destruction of cluster ions, detachment, and ion-ion recombination.

To provide a channel for photon generation we assume that one of the N_2 excited states is a metastable state denoted by N_2^* (threshold 13 eV). This state may then radiatively relax by emitting a 13.0 eV photon. Metastable relaxation is also treated in a Monte Carlo fashion with the relaxation probability at each time step given by $\Delta t/\tau_r$, where

$$\tau_r = \frac{\tau_0}{1 + P/P_0}, \quad (27)$$

where τ_r is the relaxation time and P is the gas pressure. For N_2 , Yoshida and Tagashira suggest values of $\tau_0 = 36$ ns, and $P_0 = 60$ Torr [36]. We then allow photo-ionization to occur:

$$\gamma + X \rightarrow e + X^+ , \quad (28)$$

where $X = O_2$, and O_2^- . For photons with $E < 13$ eV, photo-ionization of N_2 is not possible.

Cross-sections for all the reactions have been obtained in the literature. In many cases the reaction rate is provided, rather than the cross-section, which is what is needed for the kinetic PIC treatment. In these cases we obtain the cross section from the reaction rate by the procedure described in [37]. Cross-sections and/or reaction rates for common air reactions can be found references [1, 38, 39, 40, 41, 42]. As an example we show the cross-sections for electron-impact reactions with O_2 in Fig. 57, which were obtained from the cross-section database of the EEDF Boltzmann code [1]. The cross-section for dissociative attachment (Eq. 26) is shown in orange.

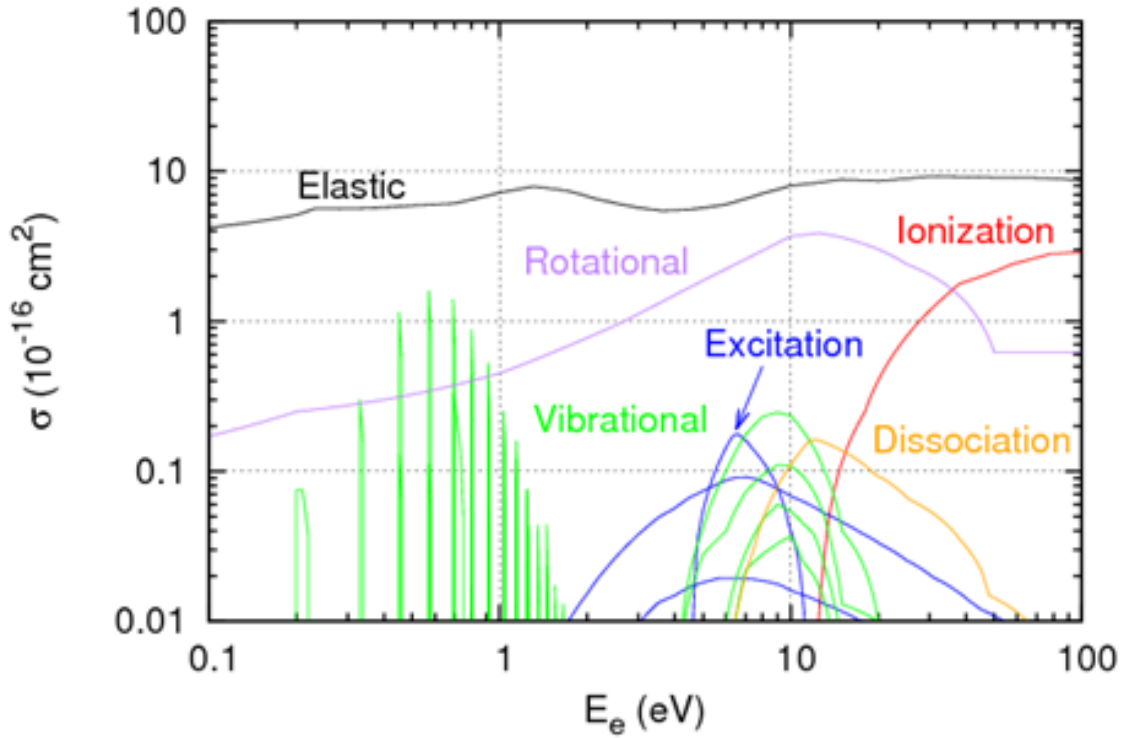


Figure 57. Electron-impact cross-sections for O_2 [1].

Electron impact reactions are all modeled by standard PIC Monte Carlo methods [43]. The photon transport algorithm in LSP is described in [35], where photo-ionization coefficients are also plotted. The remaining reactions are modeled by the binary scattering algorithms described by Nanbu and Yonemura [44, 45].

As a simple test of the air chemistry model we perform simple swarm simulations. These are one-cell PIC simulations with a fixed applied electric field. Particle momenta are advanced but not particle positions, and particle self-fields are neglected. A seed electron population starts the

avalanche. At steady-state, swarm parameters (generally functions of E/n_n for weakly-ionized plasma) can be obtained from the simulation. Results from a sample swarm simulation are shown in Fig. 58 for air (78% N_2 , 21% O_2 , 1% Ar) at STP and $E/n_n = 500$ Td (1 Td = 10^{-17} Vcm²). For simplicity photon generation is neglected. The simulation time step chosen so that $v\Delta t \approx 0.1$, where v is the total electron-neutral collision frequency. Figure 59 shows the results of a series

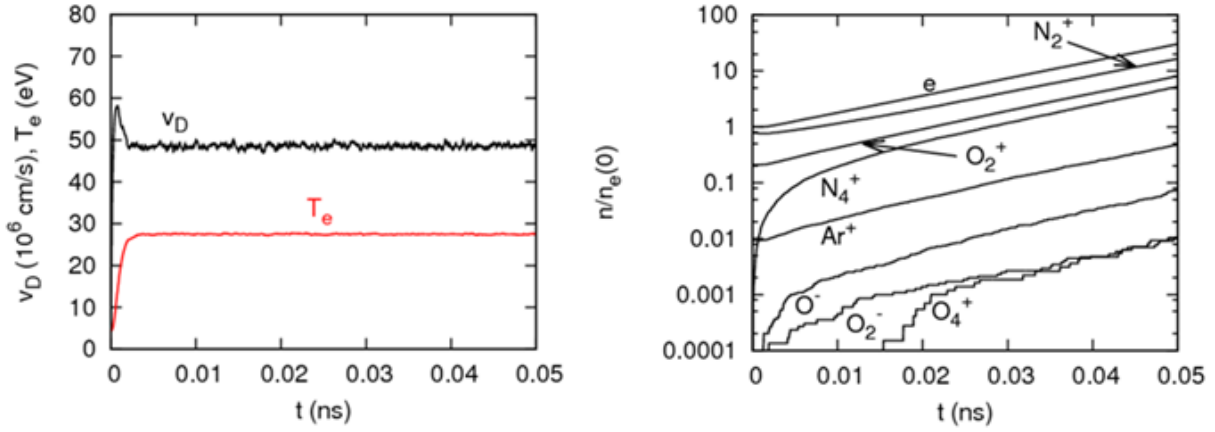


Figure 58. Results from LSP electron swarm simulation in air.

of swarm simulations for air at 1 atm in which the applied electric field is varied. Electron drift velocity and (normalized) ionization rate are shown as a function of E/n_n for air. The results from the simulations are found to be in good agreement with the swarm data compiled by Dutton [45]. We find that at 1 atm, air becomes attachment dominated when $E/n_n < 120$ Td. But we point out that the critical electric field does not scale linearly with n_n at low field strengths because an important electron attachment reaction is three-body [45], rather than two-body as in Eq. 26.

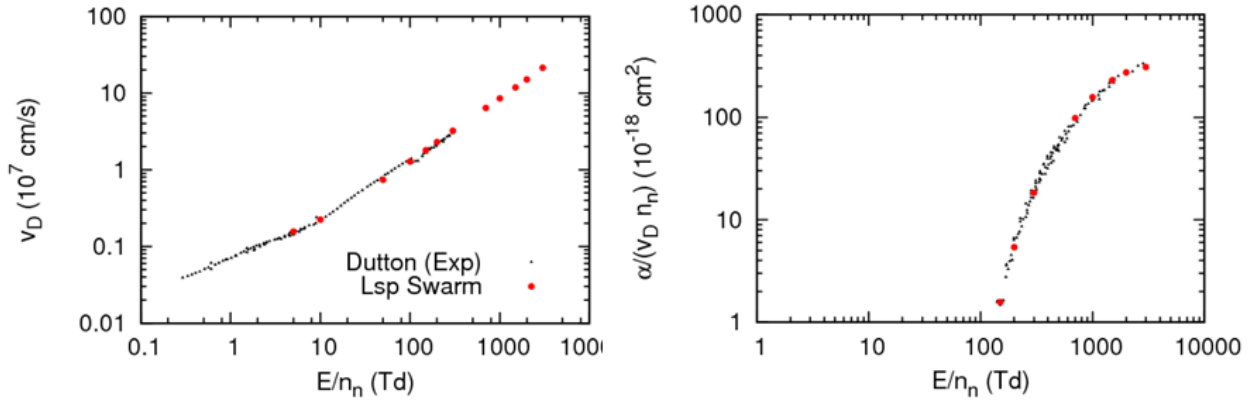


Figure 59. Electron drift velocity and normalized ionization rate as a function of E/n_n for electron swarms in air. LSP results are compared to experimental data.

6.4 Air Railgap in 2D

As with the SF₆/Ar mixture discussed in the previous section, the air simulations are to be performed with a voltage difference of 200 kV between the anode and cathode, with the trigger (roughly 1/3 of the distance between the electrodes) initially held at 70 kV above the cathode voltage. This leads again to a field magnitude on the order of 125 kV/cm between the anode and cathode. We must again determine an appropriate air density to use to avoid self-breakdown of the switch. To determine the density we perform simple one cell swarm simulations. We make use of the air chemistry model described in the previous section. For simplicity we neglect photon production and transport. Since the swarm simulations are performed at low density we neglect “second-order” reactions: that is reactions in which both reactants are themselves the products of a reaction. The rate constant for such reactions scales as n_p^2 , where n_p is the plasma density. Ion-ion recombination ($N_2^+ + O_2^- \rightarrow N_2 + O_2$) is an example of such a process. Of course, this approximation breaks when it is no longer true that $n_p \ll n_n$.

Since some of electron attachment channels for air are three body processes, for example $e + O_2 + M \rightarrow O_2^- + M$, where M is a third body (N_2 or O_2) required for momentum and energy conservation, the simple E/n_n scaling of the effective ionization rate breaks down. For this reason we perform the air swarm simulations for a fixed electric field and vary the neutral density. The results of these simulations are shown in Fig. 60. We show results for several timestep values. This is done to assess the effect of timestep on the transport parameters of the plasma, since we would like to use as large a timestep as possible in large 2D and 3D railgap simulations. We see that there is reasonable convergence of the effective ionization rate for $c\Delta t \leq 0.00085$ cm ($\Delta t \leq 2.8 \times 10^{-5}$ ns). At $c\Delta t = 0.00085$ cm dry air should be slightly attachment dominated in the railgap at $n_n = 1.5 \times 10^{20}$ cm⁻³ (≈ 5.8 atm). In the following we use this density and timestep.

Since the simulations with air have to be run at an even higher density than the SF₆/Ar mixture, we had considered ways to cut down on run-time. In one attempt a double trigger simulation with a trigger on both the left and right sides of the simulation space shown in Fig. 47 was considered. We then assumed that the electrodes were symmetric about $x = 0$ plane (x is the horizontal axis in Fig. 47). This allows us to use a symmetry boundary condition at $x = 0$. This would cut the simulation space in half. But this approach does not work in 2D. The thick black arrows in Fig. 47 show the direction of current flow when the switch is closed. The return current can only propagate along the right side of the simulation space. There is no current along the left edge because the trigger feeds and large resistors in the trigger circuit interrupt any current flow of the conducting wall on the left. So when using a symmetry plane (in 2D at least) there is no current path available for the switch. A similar problem can be circumvented in 3D (even with periodic boundaries in z) if one is careful to build in a return current path at some value of z .

We consider an initial 2D air simulation with $n_n = 1.5 \times 10^{20}$ cm⁻³ (78.084% N_2 , 20.927% O_2 , and 0.934% Ar, by number). We retain the uniform grid with 0.06 cm cells, and use the time step of $c\Delta t = 0.00085$ cm. For the start of the simulation we again neglect second-order reactions (we will see that is justified as the plasma density always remains much less than the gas density). But photon production and transport is included. Some snapshots of electron density are shown in Fig. 61. We see that for this simulation there is a secondary streamer which emerges from the

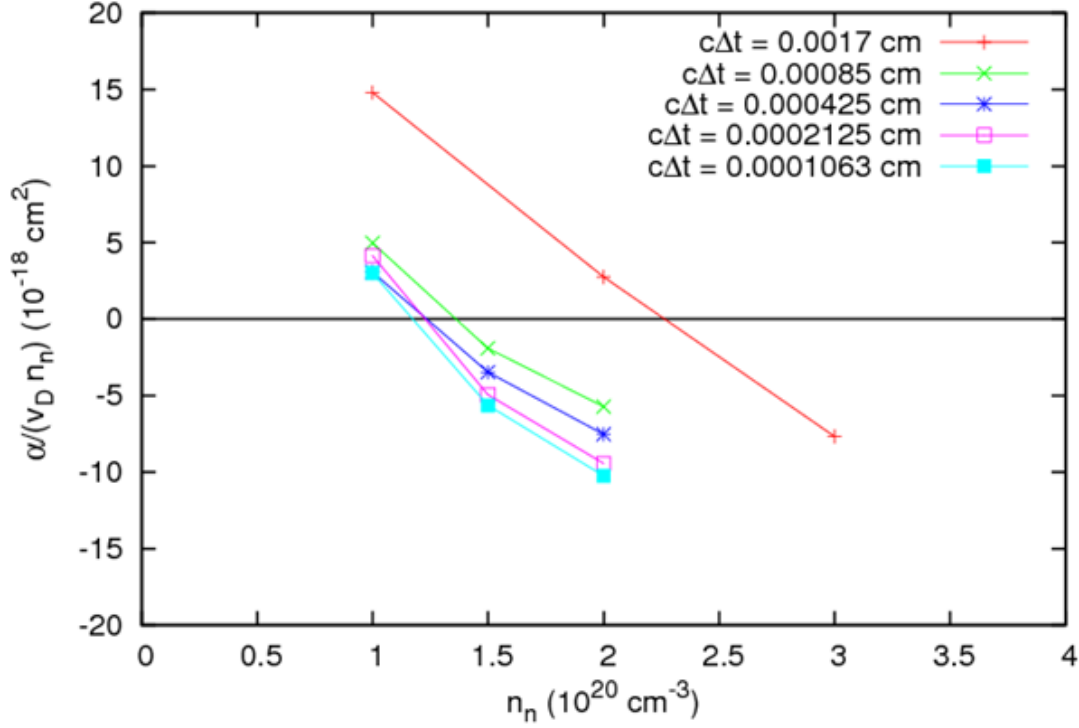


Figure 60. Normalized ionization rate for dry air as a function of n_n , for a fixed electric field of 125 kV/cm. Some variation with timestep is exhibited in the results.

right side of the cathode. Careful inspection reveals that this streamer emerges from a stair-stepped corner on the cathode conducting surface, where there is fairly strong field enhancement due to the rectilinear grid. We note that this streamer is able to propagate across the AK gap even if the trigger pulse is withheld. We allowed the simulation to proceed even with the secondary streamer present, to determine what kind of currents, voltages, and plasma densities would be obtained using the air chemistry model in this regime. A series of history plots for the run are shown in Fig. 62 which again shows the voltages, currents, resistance, and total electron charge as a function of time. The current reaches a peak value of $\approx 1.5 \text{ kA/cm}$ in $\approx 180 \text{ ns}$, at which time the electron charge has reached a steady-state value, which results in a minimum resistance of $\approx 5 \Omega$.

We attempted to use a subgrid model to reduce field enhancements due to the grid. But the subgrid model was found not to work robustly in concert with the implicit field solver and cloud-in-cell techniques needed to perform these simulations. It will require some more extensive testing to get the subgrid model to work robustly for such switch problems. To temporarily avoid difficulties with streamer generation from stair-stepped corners without using the sub-grid model, we have made some slight modifications to the cathode shape. The anode shape remains the same. The geometric modifications can be seen in Fig. 63. Note that the cathode (on the bottom) and anode formerly had mirror symmetry about the $y = 0$ plane. Essentially we have flattened out the top of the cathode and only allow emission from the flat surface. Emission is not allowed from the stair-stepped corners on both right and left. The emission region can be seen in Fig. 64. Another possible

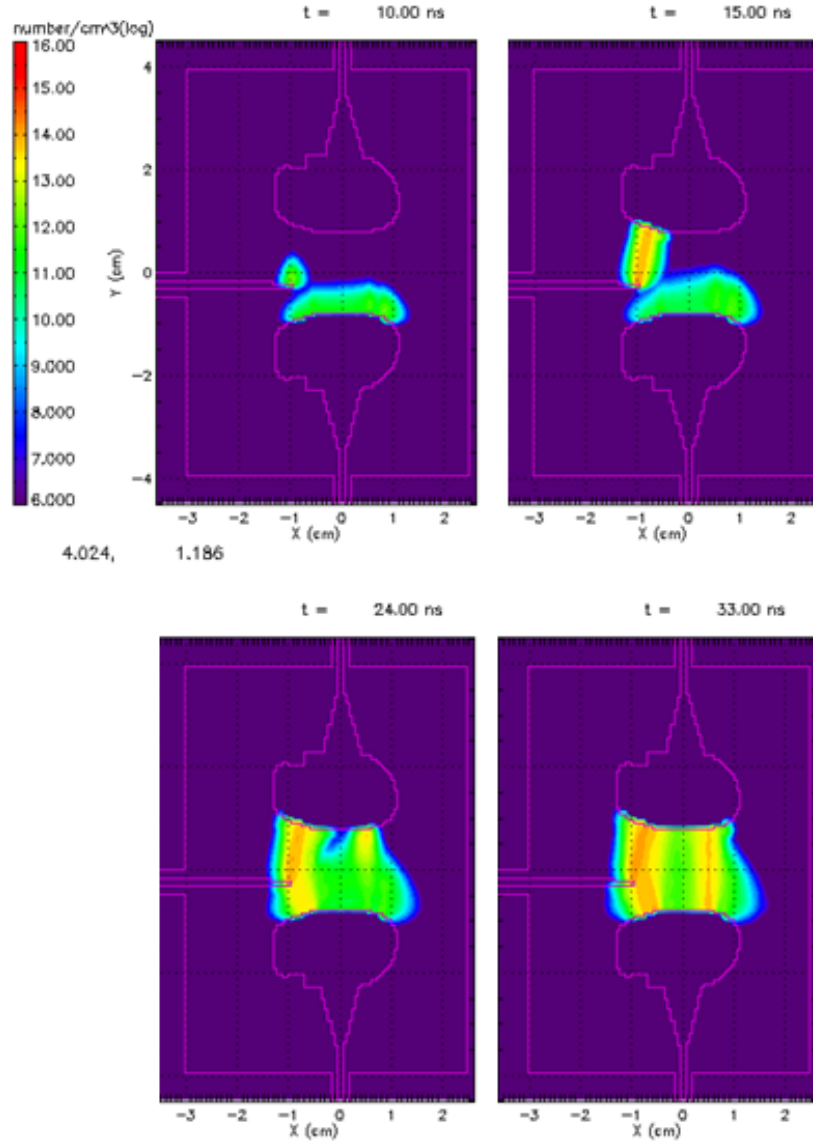


Figure 61. Electron density contours from initial 2D air railgap simulation. Note formation of spurious streamer from right hand side of cathode. This streamer was seeded by a numerical field enhancement due to a stair-stepped conducting boundary.

problem is that electrons emitted from the flat part of the cathode may still be transported to the corners and avalanche there, which may lead to propagating streamers. To remedy this possibility we suppress ionization in a small region around the cathode corners with enhanced field strengths (see Fig. 64). We have also gone to a more refined (but non-uniform) grid. In the vicinity of the AK gap, $\Delta x = \Delta y = 0.04 \text{ cm}$, but the grid in each coordinate direction becomes coarser as one approaches the simulation boundaries, where fine resolution is not required.

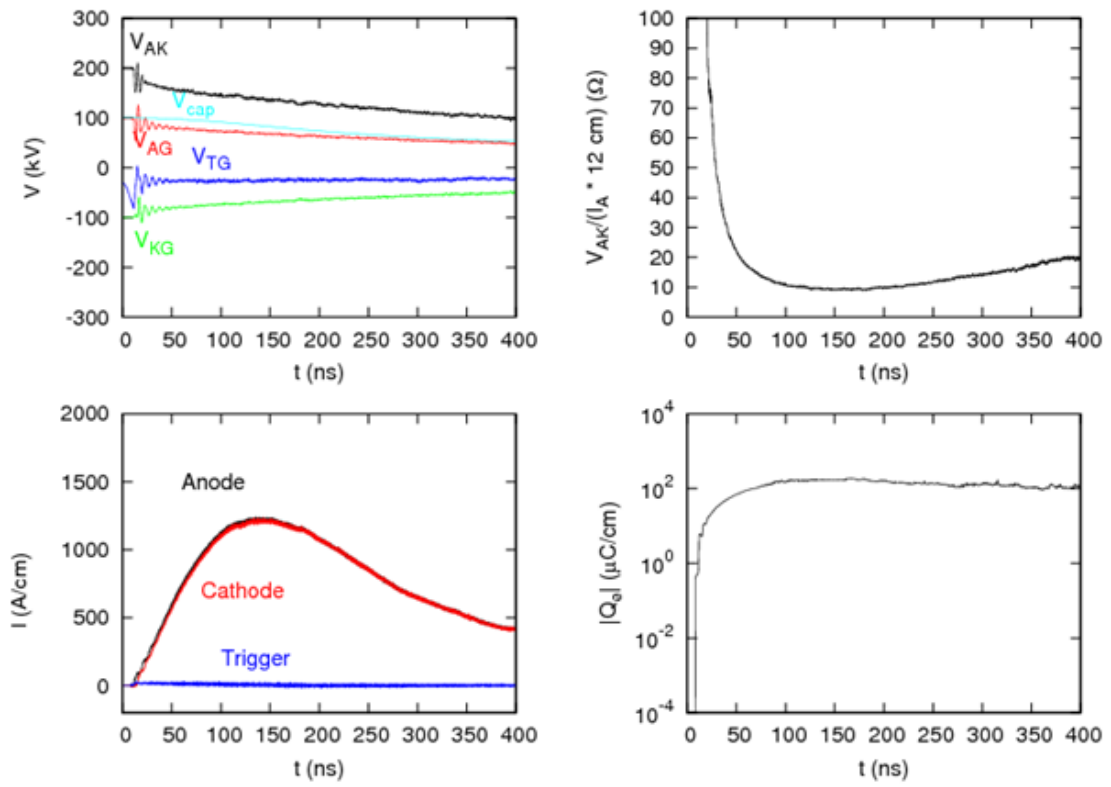


Figure 62. History plots for initial 2D air railgap simulation.

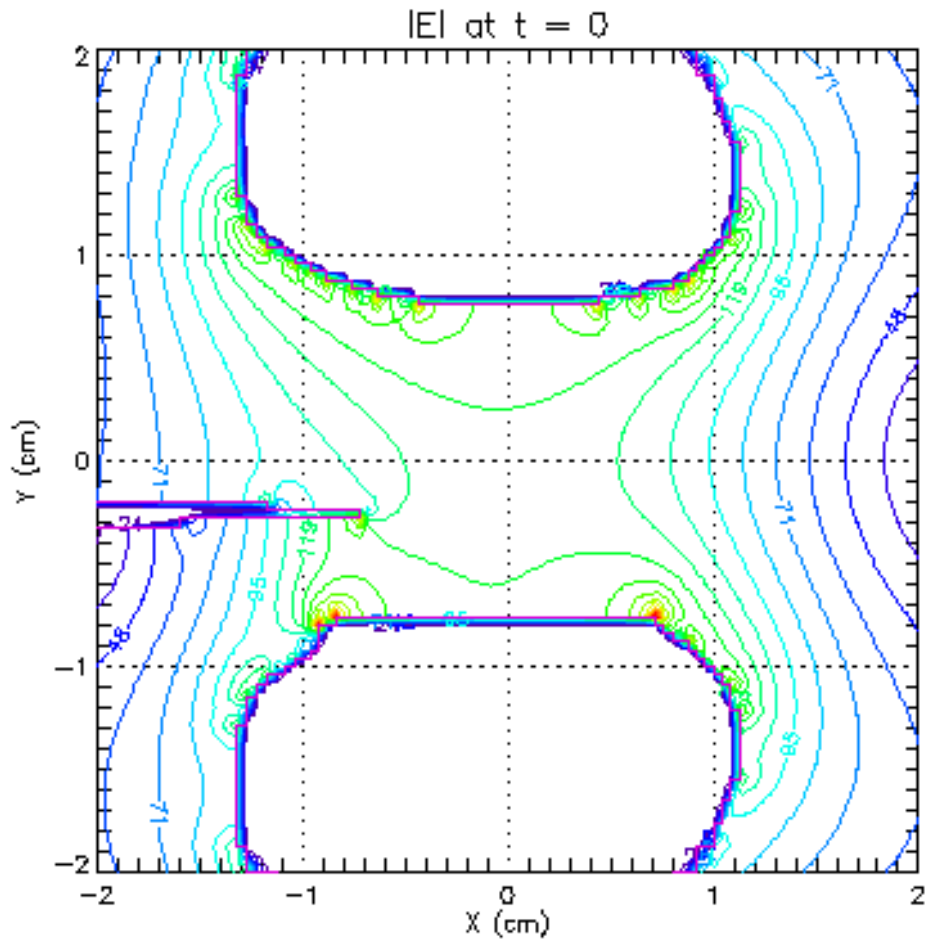


Figure 63. Slight modification of cathode geometry to avoid spurious streamer propagation from stair-stepped conducting corners. The anode shape is unaltered.

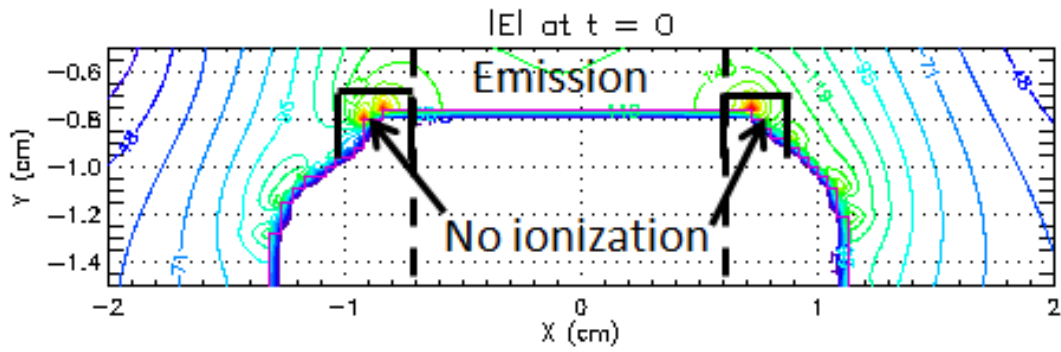


Figure 64. Restriction of ionization volume in modified railgap geometry for air.

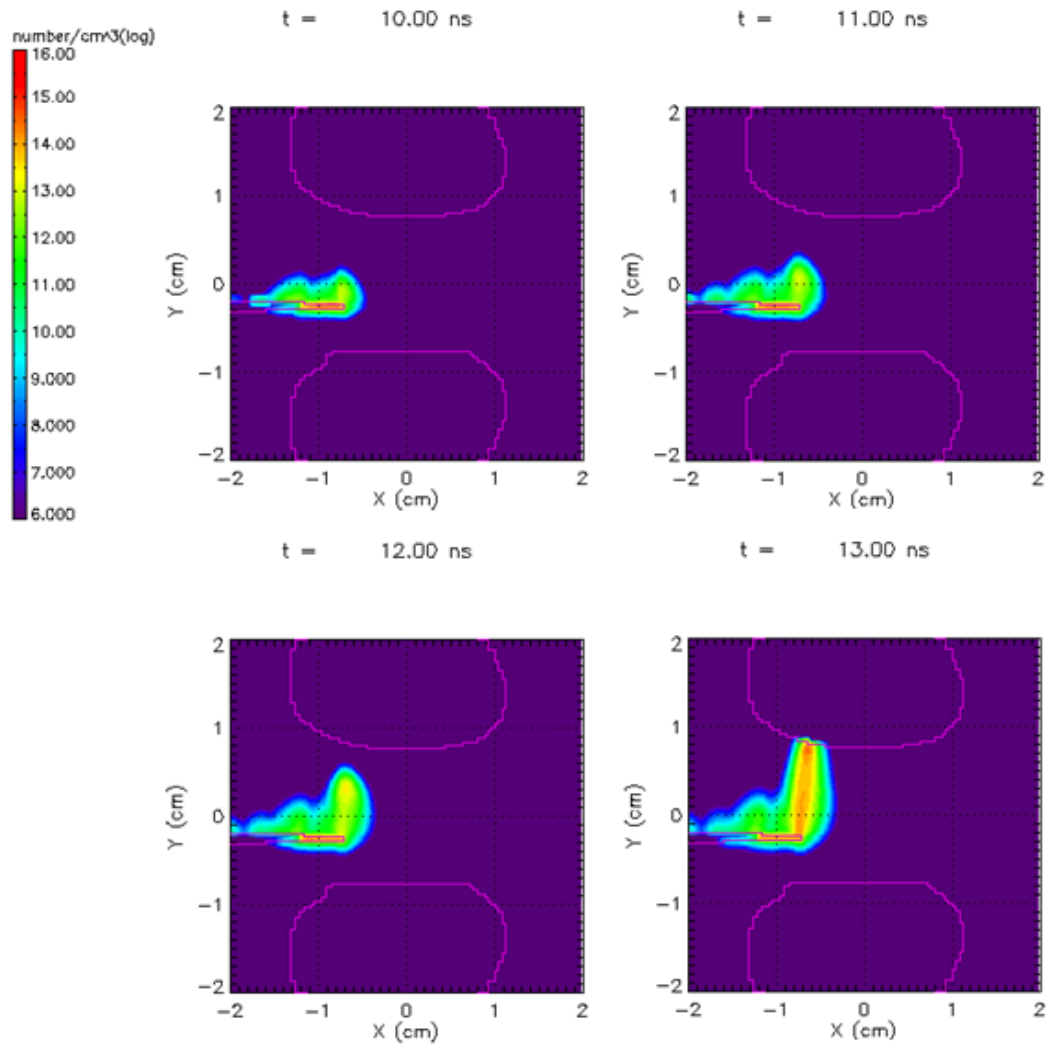


Figure 65. Snapshots of electron density 2D Air streamer simulation results. A streamer propagates from the trigger to the anode.

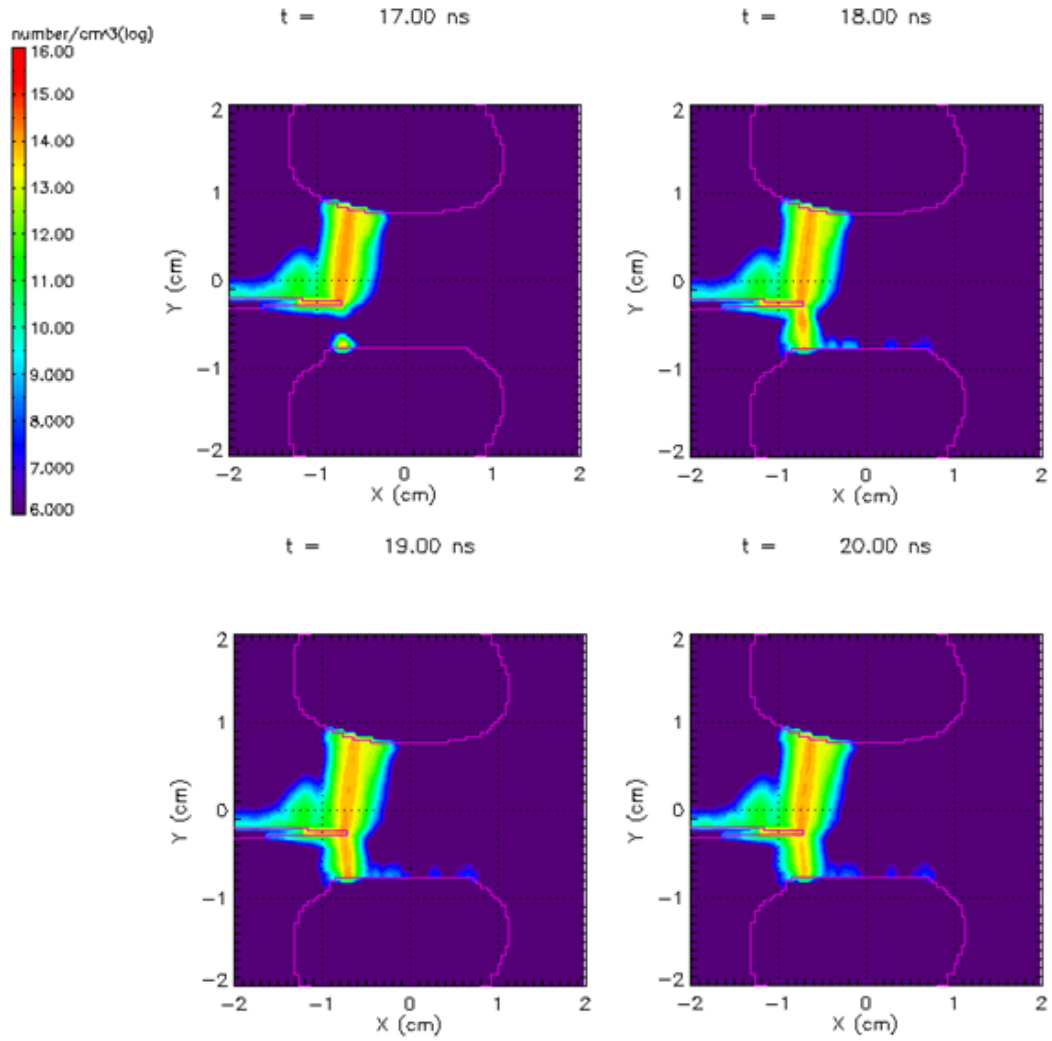


Figure 66. Snapshots of electron density for 2D Air streamer simulation. A streamer propagates from the cathode to the trigger to form a full current path from A to K.

Assessment of current channel thickness in 2D r-z simulations

In this section we consider the results of a 2D r-z switch test. The motivation for this test is two-fold. In the railgap simulations discussed above we never reached densities considerably above 10^{16} cm^{-3} in gas densities on the order of $10^{19} - 10^{20} \text{ cm}^{-3}$. This means that the gas remains relatively weakly-ionized throughout. But considerably higher plasma densities are expected in the railgap. So we were interested in determining under what conditions higher plasma densities can occur. We would also like to determine the natural width of the current channels in a 3D geometry in which pinching in all dimensions is allowed.

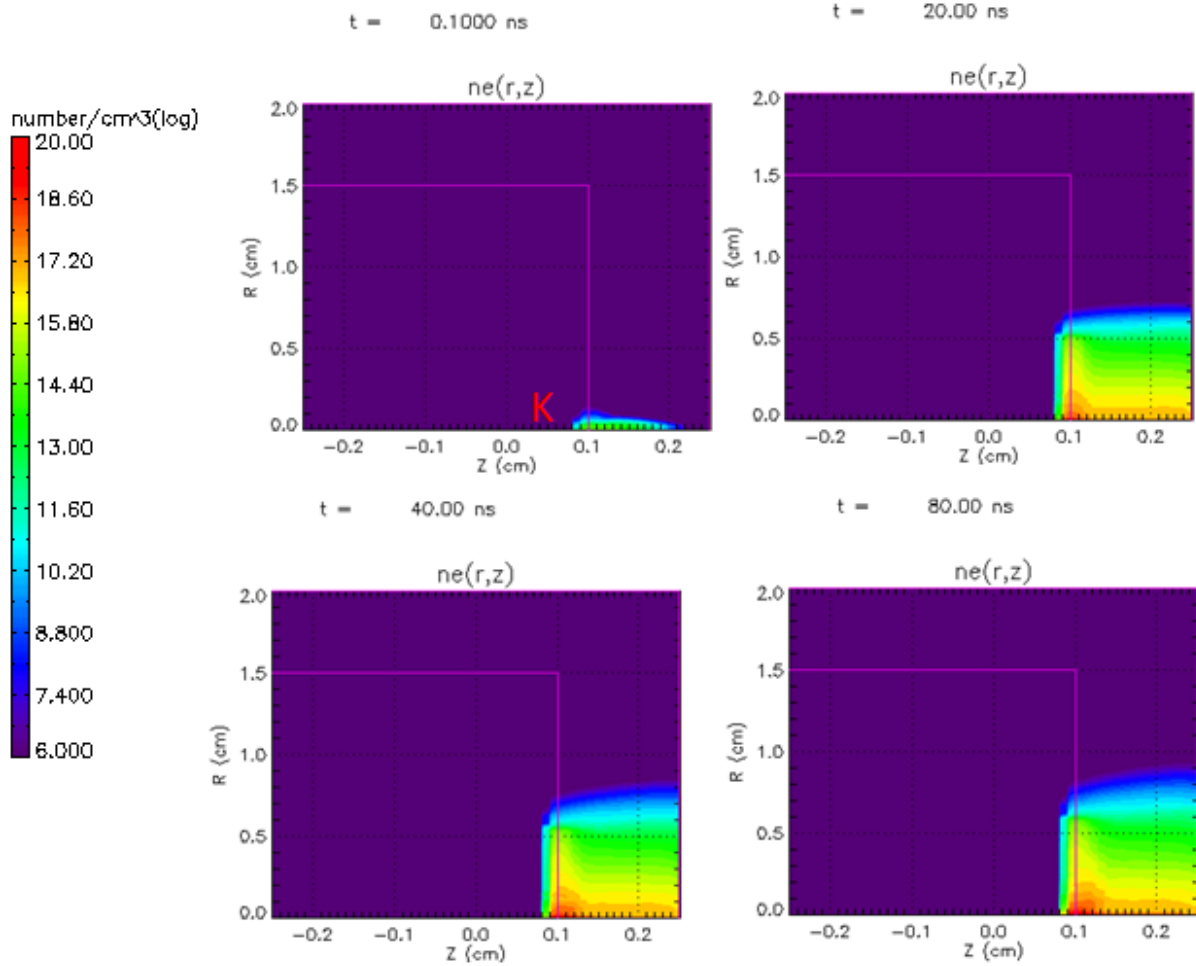


Figure 67. 2D-rz cylindrical switch simulation using pure N_2 at 1/2 atm. Snapshots of electron density contours.

The geometry of the switch can be seen in Fig. 67. Power is fed from the left at large radius. The AK gap is 0.15 cm at $r = 0$. The circuit model connected to the input port is shown in Fig. 68. The transmission line segments are electrically short and have impedances of $Z_{grid} = 17.25 \Omega$ (matched to the input port impedance), and $Z_0 = 0.5 \Omega$. The mismatch between the two transmission lines results in much more current (for a fixed voltage) running through the switch. The incoming

voltage wave, $V_{in} = 3.125$ kV, is independent of time (an initial static field solve is used to start the simulation). This results in a total short circuit of 6.25 kV. The switch is filled with pure N_2 at 0.5 atm. We use pure diatomic nitrogen, instead of air, to limit the number of included species (and therefore particle number). With this density, voltage, and gap distance we find $E/n_n \approx 320$ Td. This allows for strong avalanche ionization of the gas. So this is not a feasible switch since it would self-break from any initial seed plasma. But for this exercise we are not concerned with designing a switch. Instead we wish to generate a high density plasma and to assess the thickness of the current path.

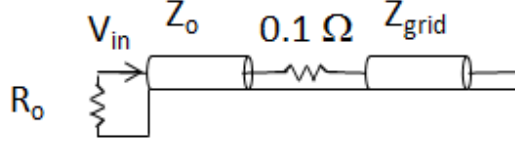


Figure 68. Driving circuit for cylindrical switch simulation. $Z_{grid} = 17.25 \Omega$, and $Z_0 = R_0 = 0.5 \Omega$ and $V_{in} = 3.125$ kV.

A seed plasma of density $3 \times 10^{14} \text{ cm}^{-3}$ is introduced into the simulation from $z = 0.1$ cm to 0.14 cm, from the axis out to a radius of 0.02 cm (see the top left of Fig. 67). This is analogous to a laser-triggered situation in which a seed plasma is created in the switch gap by ionization due to laser irradiation. Space charge limited emission of electrons is allowed out to a radius of 0.8 cm, and any ions (N_2^+) lost to the conducting walls are replaced by a new electron-ion pair. The cell size is $\Delta x = \Delta y = 0.02$ cm, and the time-step is chosen to resolve the electron-neutral collision time, for this reason we have chosen a relatively low gas density (compared to the railgap switch).

Snapshots of electron density at $t = 0.1, 20, 40$, and 80 ns are shown in Fig. 67 and history plots of voltage, current, resistance, and rms radius are shown in Fig. 69. From the two figures we see that by ≈ 20 ns, the simulation reaches a quasi-steady-state, in which the switch resistance drops to less than 0.2Ω . The electron density near the cathode approaches 10^{19} cm^{-3} , so in this regime we can get a reasonable ionization fraction, which we have yet to see in the full railgap simulations. In the bottom right of Fig. 69, we display the electron rms radius as a function of time in three different z -windows in the AK gap: $[0.1, 0.25]$ cm (black), $[0.15, 0.2]$ cm (red), and $[0.2, 0.25]$ cm (blue), there is still some slight variation with time after 20 ns, but all of the rms radii measurements roughly asymptote to 0.15 cm, which corresponds to 7 or 8 radial cells. So there appears to be a natural radius to which the current path seeks to evolve. A similar radius was found with dry air at 1 atm. Although without further testing it is difficult to generalize these results, based on this limited data, we seem to find current filaments which are on the order of 1 mm. This implies that cell sizes of a few hundred microns should suffice.

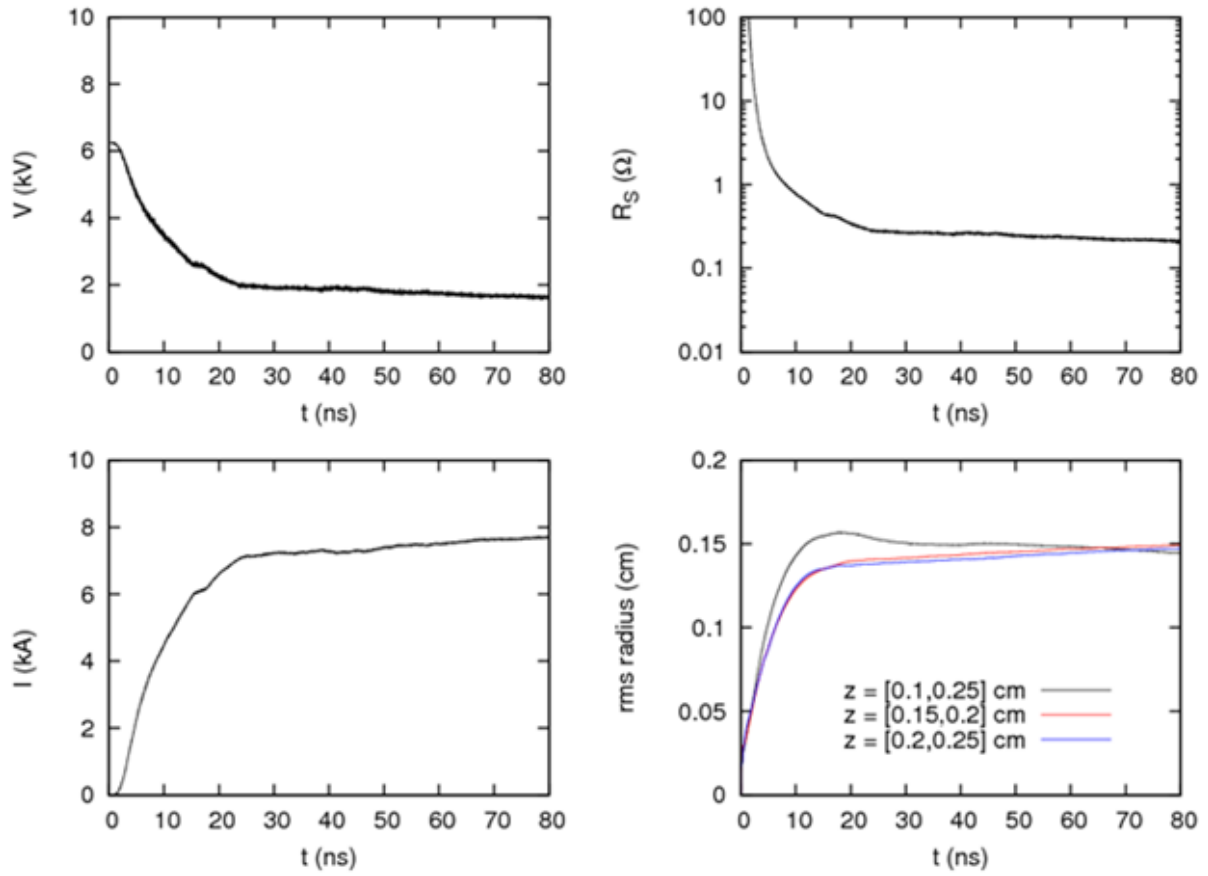


Figure 69. History plots of voltage, current, resistance, and rms radius for 2D-rz switch test.

6.5 Filamentation in 2D/3D Cartesian Switch Tests

In the previous section we considered a simple 2D-rz switch test problem to investigate the natural thickness of initially thin seeded plasma current channels. In this section we return to Cartesian coordinates for a simple “railgap-like” test problem in 2D and 3D to investigate the formation of filaments in the z -direction. The geometry for the test problem is shown in Fig. 70. The bottom electrode in the figure is the cathode and the left and right boundaries are both connected to the circuit model shown in Fig. 71. The switch gas is pure N_2 at 1 atm. A seed plasma density of 10^{14} cm^{-3} is placed between the cathode and anode (top left of Fig. 70). For the initial 2D Cartesian simulation we use a uniform cell size of 0.02 cm in both the x and y directions.

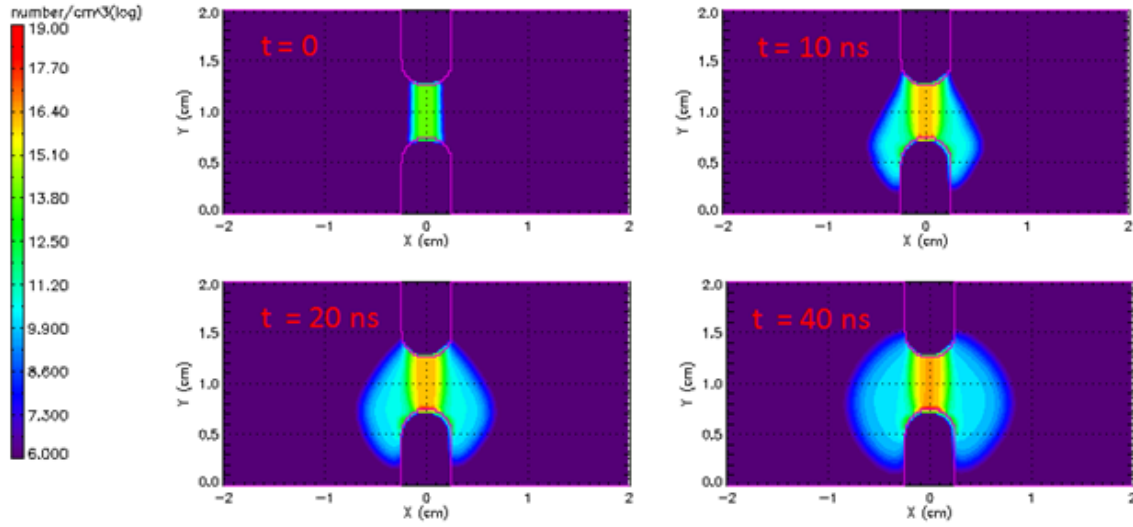


Figure 70. Snapshots of electron density contours for 2D Cartesian switch test with pure N_2 at 1 atm.

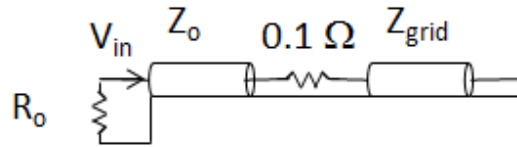


Figure 71. Driving circuit attached to both the left and right input ports of the simulation space shown in Fig. 70. $Z_{grid} = 732 \Omega$, and $Z_0 = R_0 = 5 \Omega$.

The incoming voltage wave, V_{in} , ramps linearly up to 25 kV in 2 ns. This leads to a maximum field of $\approx 100 \text{ kV/cm}$ between the electrodes when the switch is open. Such a field value leads to rapid avalanche breakdown in 1 atm N_2 . So, as in the test problem in the previous section, this test problem would self-break under the full voltage. History plots of voltage, current, resistance,

and total electron charge for the 2D test problem are shown in Fig. 72, and snapshots of electron density contours are shown in Fig. 70. From the history plot we see that the resistance of the switch drops to $\approx 0.1 \Omega$ in about 40 ns, and from Fig. 70, we see that plasma densities close to 10^{19} cm^{-3} occur along the cathode surface.

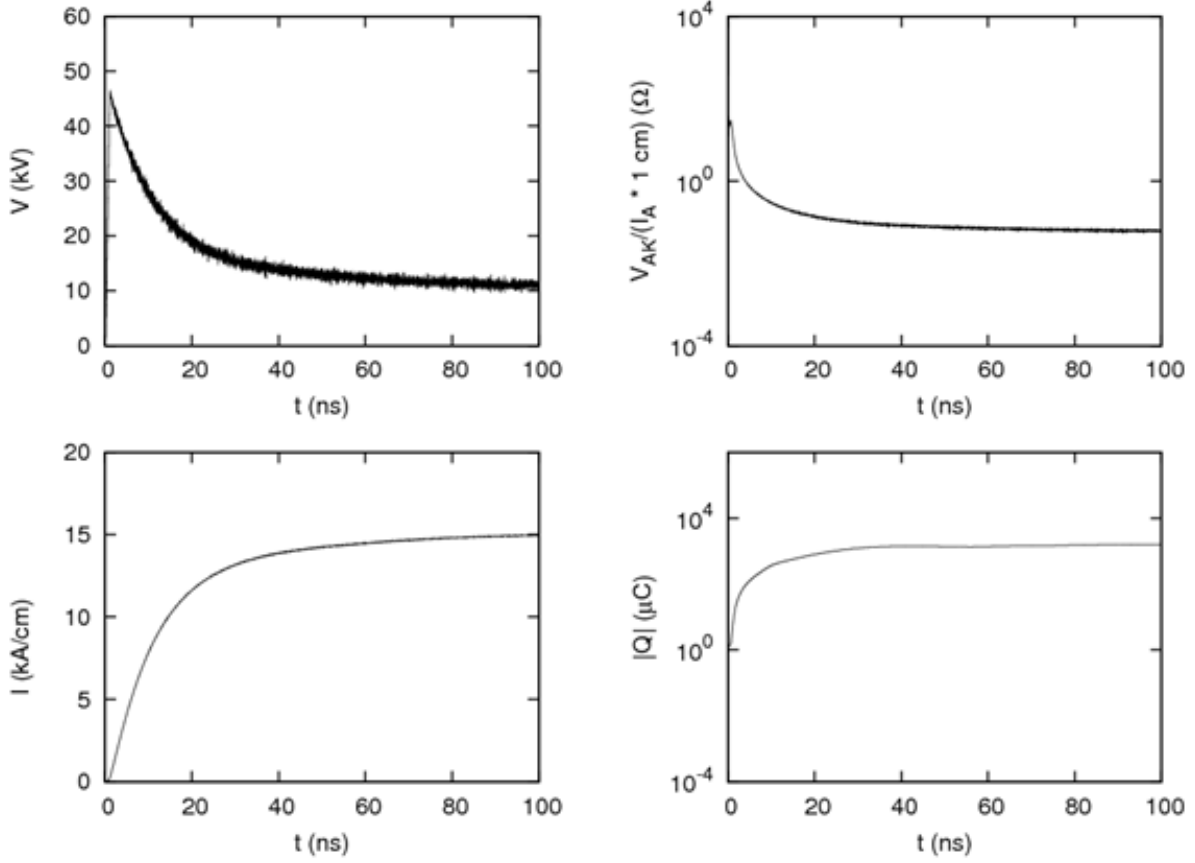


Figure 72. History plots of voltage, current, resistance, and total electron charge for 2D Cartesian switch test with pure N_2 at 1 atm.

We now consider the 3D version of the test problem in which the switch is modeled for a length of 1.5 cm in the z direction with periodic boundaries at $z = 0$ and 1.5 cm. Figure 73 shows the simulation geometry as well as the initial iso-contour of plasma density at 10^{14} cm^{-3} . To decrease the runtime, the 3D version is performed at the spatial resolution of the initial 2D version (results of which were shown in Fig. 70 and Fig. 72). We compare the history plots of voltage, current, resistance, and total electron charge of the 2D and 3D runs in Fig. 74. We see that there is little difference between the 2D and 3D results for the voltage, current per unit length, and resistance (normalized to a 1 cm length in the 3D case). The slight offset in total charge is primarily due to the 1.5 cm length of the 3D simulation, while the 2D simulation assumes a 1 cm length in the virtual direction. Although the voltage-current characteristics are very similar in 2D and 3D, we do see some formation of filamentary structures in the z direction. This can be seen in Fig. 75 which shows electron density contours in the $x = 0$ plane. We see the evolution of clumps of high electron

density along the cathode, with the clumps on the order of 1 mm wide. This is in rough agreement with the channel width found in the cylindrical test problem. However, there is very little density variation with z , close to the anode surface, so we don't seem to develop a full filament extending from anode to cathode. It was suggested that the filamentation in z would lead to enhanced current and reduced resistance in the 3D results (compared to 2D), but Fig. 74 does not show any indication of this effect.

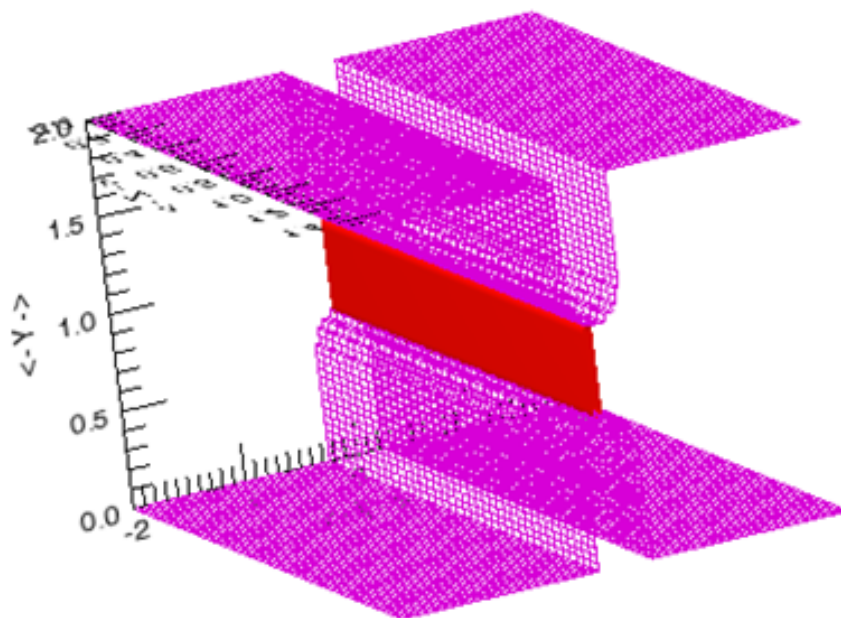


Figure 73. Initial electron density iso-contour of 10^{14} cm^{-3} for 3D Cartesian switch test in pure N_2 at 1 atm.

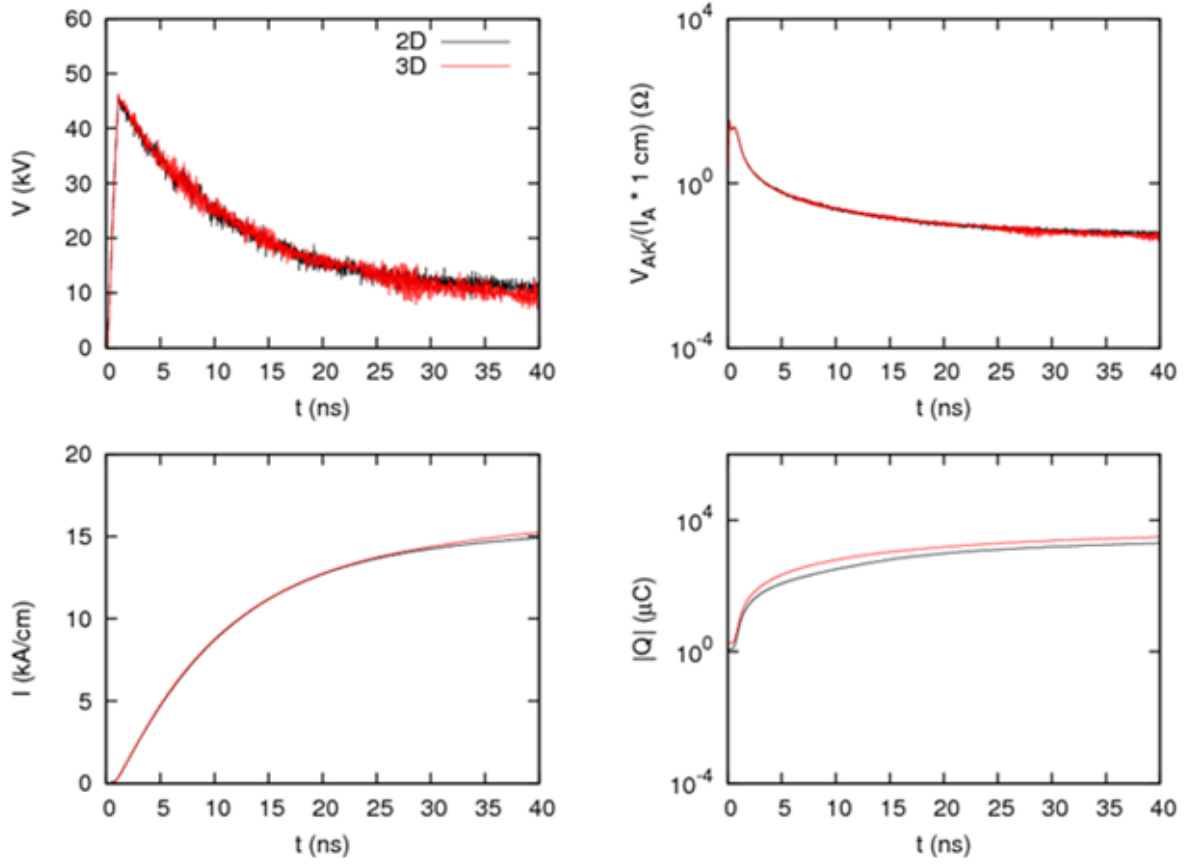


Figure 74. History plots of voltage, current, resistance, and total electron charge for 2D (black) and 3D (red) Cartesian switch test with pure N_2 at 1 atm.

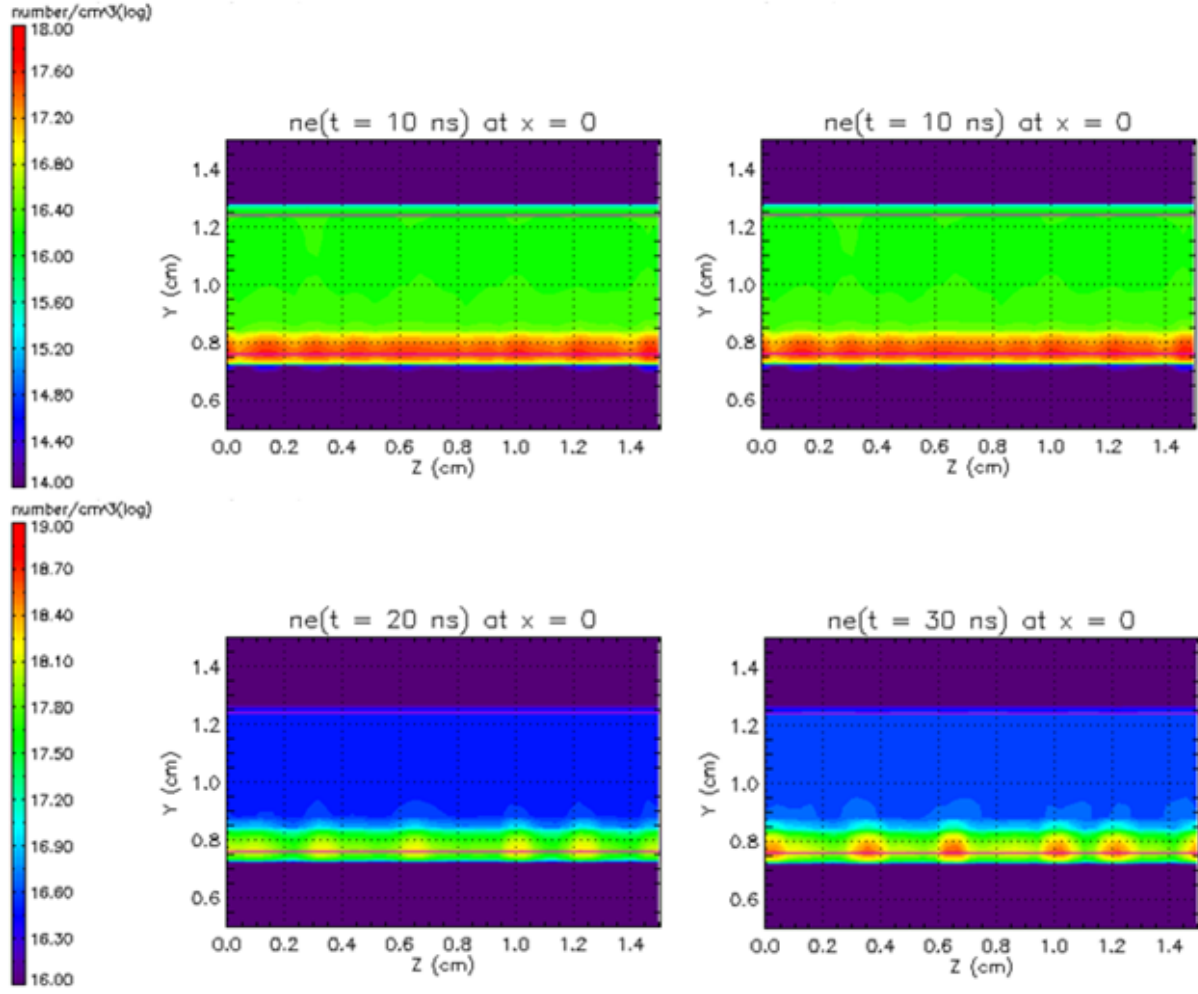


Figure 75. Electron density contours in the midplane of the switch for the 3D Cartesian simulation. The development of ≈ 1 mm wide filamentary structures along the cathode surface is observed.

6.6 Air railgap in 3D

Some notable results from the 2D simulation were that the maximum electron density in the switch only reached a value of 10^{16} cm^{-3} . A value 1 to 2 orders of magnitude larger was expected based upon prior experience with similar switches. The maximum switch resistance was found to be about 10Ω , a value 1 order of magnitude higher than expected. These results provided the motivation for a full 3D railgap simulation. In 3D we expect current filaments to form along the rails. Pinching of the filaments should produce higher current densities and more Joule heating, which should lead to more ionization, and presumably higher electron densities and lower switch resistance.

3D electrostatic field solution for full railgap switch

As in the 2D case, we first calculated a 3D electrostatic field solution of the full railgap switch in 3D Cartesian coordinates. The simulation space is shown in Fig. 76. We note that we have used the original cathode shape for this simulation, rather than the slightly modified cathode shape used for the switch simulations with air. The simulation extends from 0 to 12 cm in z , with a symmetry boundary located at the midpoint of the rails at $z = 0$. The electrodes extend from 0 to 6 cm, with the electrodes being abruptly stopped at the $z = 6 \text{ cm}$ plane. We did not make any efforts to smooth the ends of the electrodes to avoid field enhancements near $z = 6 \text{ cm}$. The cell size is $\Delta x = \Delta y = 0.03 \text{ cm}$, and $\Delta z = 0.09 \text{ cm}$. The simulation is run for only one time step, using the static field initialization described above. There are no particles included, so the switch is open.

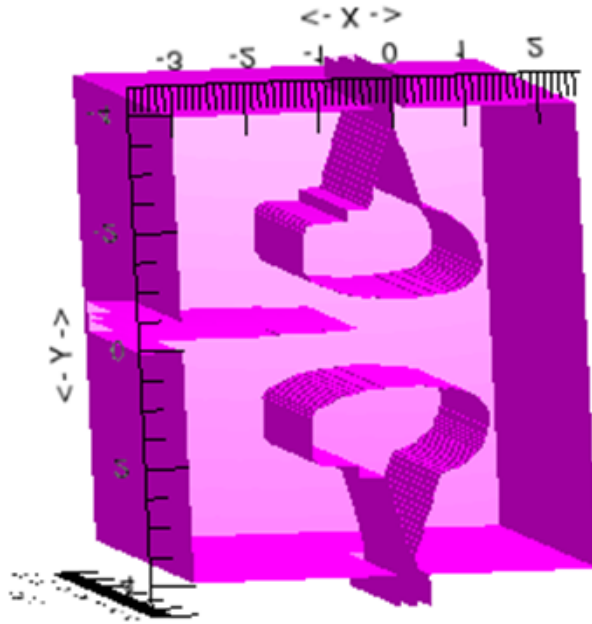


Figure 76. Geometry for full railgap switch field calculation.

In Fig. 77, we plot the electric field in the xy plane at several values of z (note that the color tables are different for each of the four plots). In the top row are the fields at $z = 0$ and $z = 5$ cm, where $z = 0$ corresponds to the middle of the rails and $z = 5$ cm is one cm in from the flat ends of the rails. We note that there is very little difference in the fields in the middle and one cm from the ends. We obtain a field value of ≈ 125 kV/cm at the center of the AK gap. This is the value that was used to calculate minimum gas densities for the railgap simulations above. The fields at the $z = 6$ cm plane show some field enhancements (on the order of a factor of two). But these enhancements could be considerably reduced by replacing the flat ends of the electrodes by some tapered shape. The plot at $z = 9$ cm, shows that just a few cm from the end of the rails the field has fallen by more than two orders of magnitude. Figure 78, which shows the electric field in the $x = 0$ plane again illustrates the field enhancement at the end of the rails.

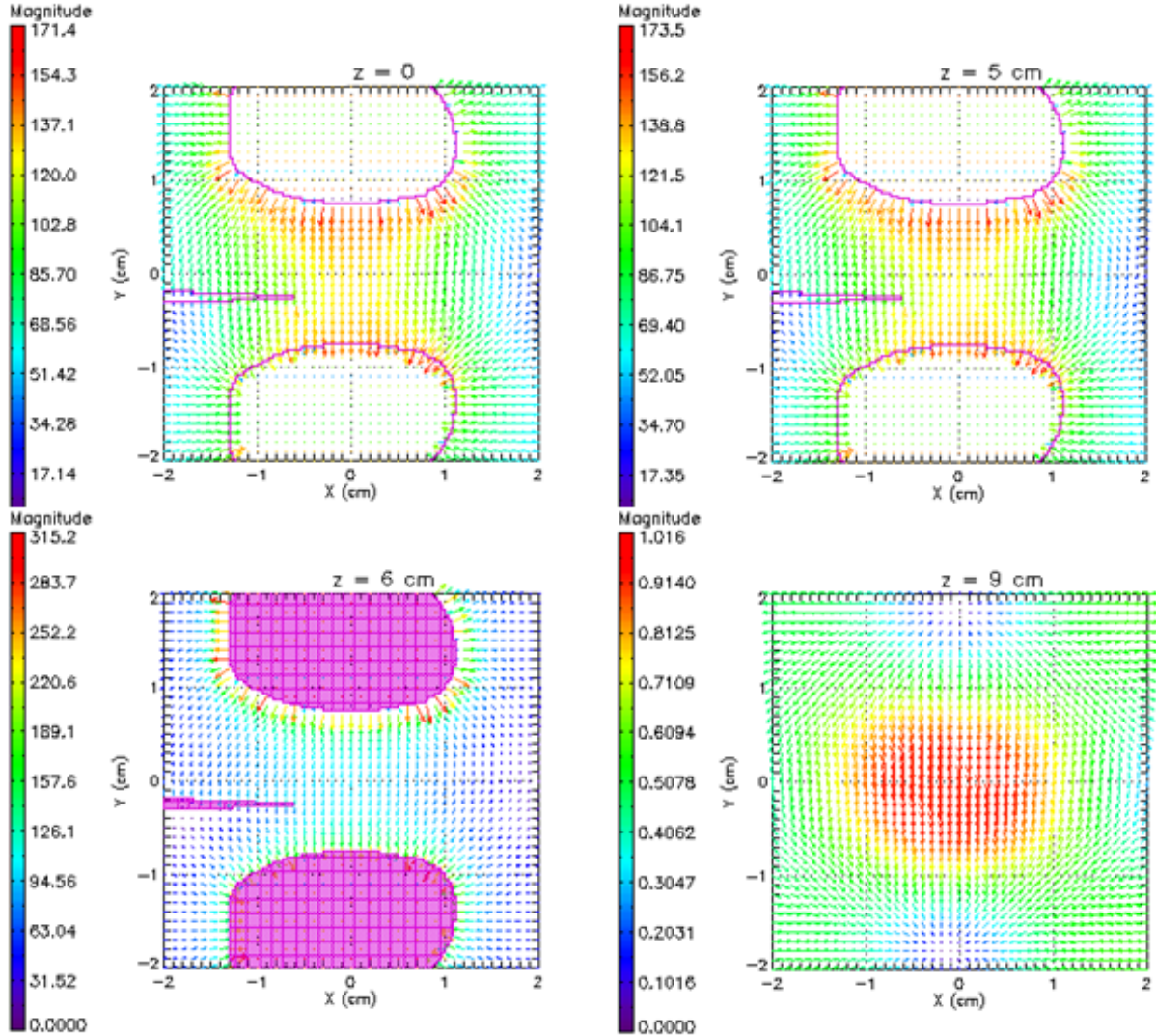


Figure 77. Vector plots of electric field from 3D railgap field solution in the xy plane at several fixed z positions. The color map shows the field magnitude in kV/cm.

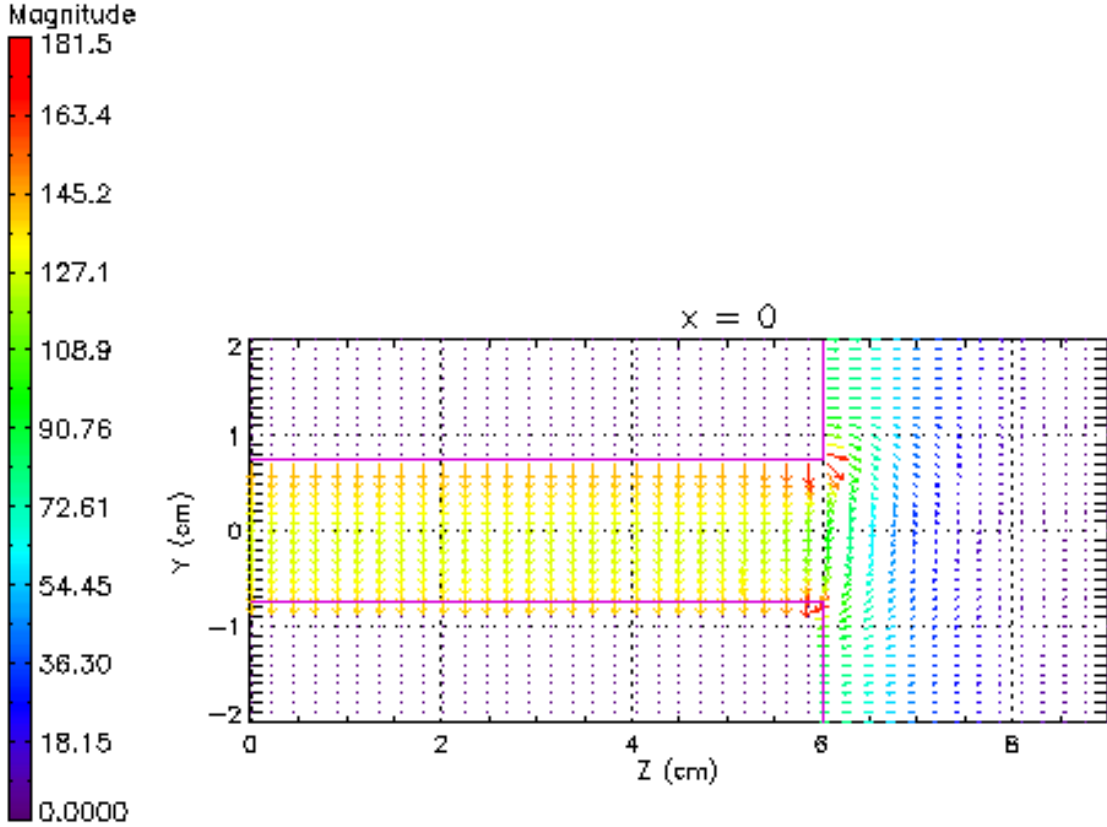


Figure 78. Vector plot of electric field from 3D railgap field solution in $x = 0$ plane. Some field enhancement is evident at the end of the railgap. Note: $z = 0$ is a symmetry plane. The color map shows the field magnitude in kV/cm.

Now, having a static field solution for the 3D case, we set it up exactly as the 2D analog but we now explicitly simulate a 1.5-cm segment in the z direction, and assume periodic boundaries. Edge effects are neglected. This simulation contains $\approx 10^6$ total cells, and $> 10^8$ particles, and must be run for millions of time steps. On several 100 processors the 3D simulation was run out to 50 ns in about 1 month. The small time step is the main bottleneck causing the long runtimes.

In Fig. 79 we show an electron density iso-contour ($n_e = 2.2 \times 10^{14} \text{ cm}^{-3}$) at $t = 16.2 \text{ ns}$, when both the TA and KT gaps have just closed. Filaments along the rails are seen both from anode and cathode to trigger. The same effect can be seen in Fig. 80, which shows electron density contours in planes along the rails in both the TA and KT gaps. The small squares on the right of Fig. 80 show the size of the cells in the xz plane ($400 \times 400 \mu\text{m}^2$). The filaments are only a few cells in width. But simulations with higher resolution in the xz plane give similar widths. Despite the presence of filamentary structure in 3D, we find the amount of charge and current per unit length are nearly the same as in the 2D simulation. So the LSP simulations do not predict higher currents in 3D due to stronger pinching at the higher dimensionality.

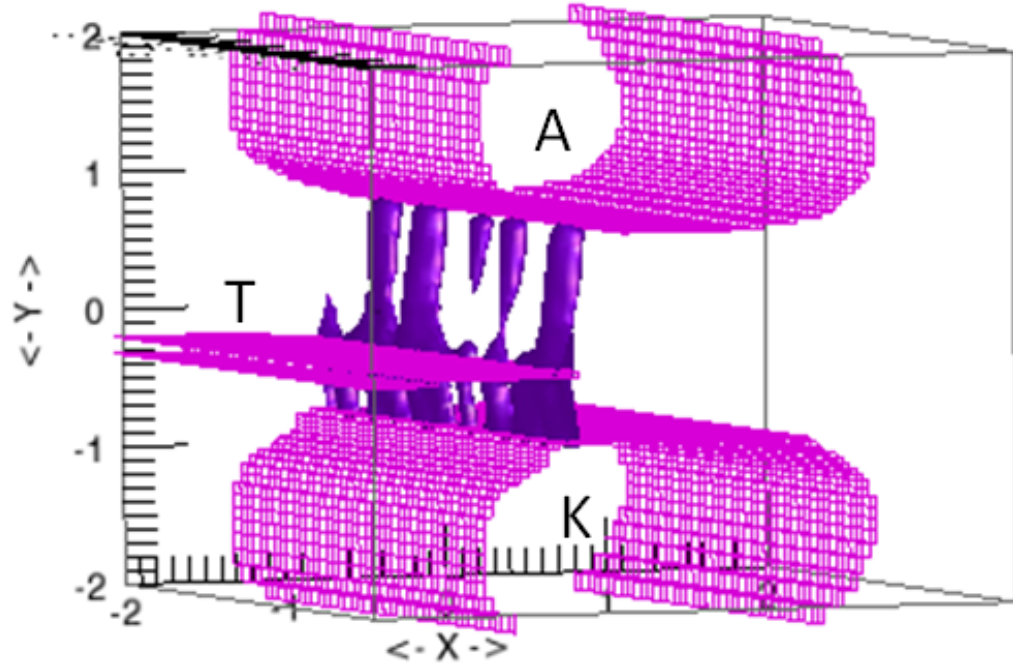


Figure 79. Electron density iso-contour ($n_e = 2.2 \times 10^{14} \text{ cm}^{-3}$) of 3D railgap simulation at $t = 16.2 \text{ ns}$.

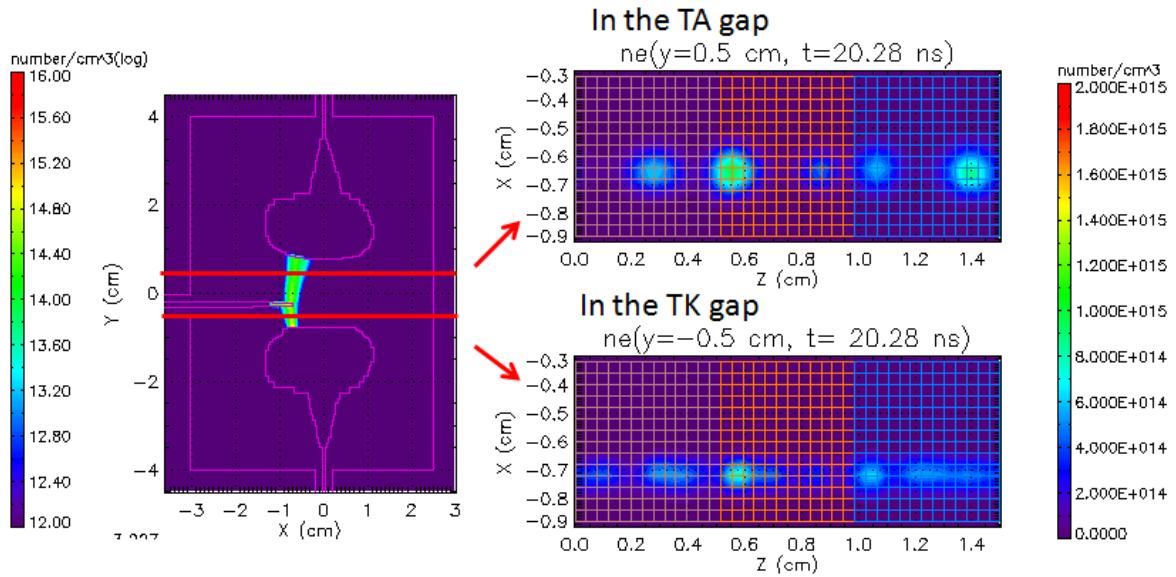


Figure 80. Electron density contours ($t = 21 \text{ ns}$) along the rails show filamentary structure.

6.7 Summary

We have performed 2D and 3D fully kinetic hybrid-PIC simulations of the three-electrode triggered railgap closing switch. An air density of 6.5 atm is required to hold off 200 kV across the 1.5 cm AK gap until the switch is closed by a pulse applied to the trigger electrode. 2D and 3D simulations predict a total current of ≈ 1.5 kA per unit length (along the rails). For a 12 cm length railgap this leads to a switch resistance on the order of $10\ \Omega$. The electron number density in both 2D and 3D reaches $\approx 10^{16}\text{ cm}^{-3}$. 3D simulations show the development of longitudinal current filaments of radius on the order of 1 mm with a spacing of a several mm. But there is no sign of enhanced current (or reduced switch resistance) due to three-dimensional pinching of filaments. These simulations qualitatively display closing switch behavior using a fully-kinetic PIC-based approach, but the electron densities are believed to be 1-2 orders of magnitude too small, and the switch resistance 1-2 orders of magnitude too large.

References

- [1] A. Napartovich. Eedf user's guide.
- [2] J. R. Woodworth, W. A. Stygar, L. F. Bennett, M. G. Mazarakis, H. D. Anderson, M. J. Harden, J. R. Blickem, F. R. Gruner, and R. White. New low inductance gas switches for linear transformer drivers. *Physical Review Special Topics-Accelerators and Beams*, 13(8):080401–080401 – 080409, 2010.
- [3] J. R. Woodworth, W. E. Fowler, B. S. Stoltzfus, W. A. Stygar, M. E. Sceiford, M. G. Mazarakis, H. D. Anderson, M. J. Harden, J. R. Blickem, R. White, and A. A. Kim. Compact 810 kA linear transformer driver cavity. *Physical Review Special Topics-Accelerators and Beams*, 14(4):040401–040401 – 040407, 2011.
- [4] G. R. Neil and R. S. Post. Multichannel, high energy rail-gap switch. *Review of Scientific Instruments*, 49(3):401–403, 1978.
- [5] R. S. Taylor and K. E. Leopold. UV radiation-triggered rail-gap switches. *Review of Scientific Instruments*, 55(1):52–63, 1984.
- [6] A. Endoh and S. Watanabe. Laser triggering of a 500-kV rail-gap switch. *Journal of Applied Physics*, 59(10):3561–3565, 1986.
- [7] G. Kovacs, S. Szatmari, and F. P. Schafer. Low jitter rail-gap switch triggered by subpicosecond KrF laser-pulses. *Measurement Science & Technology*, 3(1):112–119, 1992.
- [8] E. A. Lopez, G. A. Bennett, R. R. Bartsch, J. C. Cochrane, J. R. Griego, R. D. Hicks, W. B. Hinckley, K. W. Hosack, R. J. Kasik, A. Marquez, W. M. Parsons, W. A. Reass, M. C. Thompson, and D. Casper. Rail-gap switch modifications and test data for the atlas capacitor bank. *11th IEEE International Pulsed Power Conference - Digest of Technical Papers, Vols. 1 & 2*, pages 881–886, 1997.
- [9] K. Masugata, H. Tsuchida, H. Saitou, and K. Yatsui. Studies and performance of decreased rail gap switch inductance by enhancing multichanneling via gas mixture. *IEEE Transactions on Plasma Science*, 25(1):0093–3813/0097–0099, 1997.
- [10] H. C. Harjes, J. M. Elizondo, R. Chavez, and Z. Wallace. Low inductance gas switching, 2007.
- [11] W. A. Stygar, M. E. Cuneo, D. I. Headley, H. C. Ives, R. J. Leeper, M. G. Mazarakis, C. L. Olson, J. L. Porter, T. C. Wagoner, and J. R. Woodworth. Architecture of petawatt-class z-pinch accelerators. *Physical Review Special Topics - Accelerators and Beams*, 10(3):030401, 2007.
- [12] M. Gilmore, B. Stoltzfus, M. E. Savage, and W. T. Clarke. Measurement of the effective length of laser-plasma channels in a laser triggered gas switch by guided microwave backscattering in sf6 and n2/sf6. *2009 IEEE Pulsed Power Conference, Vols 1 and 2*, pages 595–600, 2009.

- [13] A. Robledo-Martinez, H. Sobral, and M. Villagr n-Muniz. Dipolar field and plasma expansion at the onset of laser-induced breakdown in a uniform dc field. *Journal of Physics D: Applied Physics*, 37(20):2819, 2004.
- [14] R. W. Crompton and M. T. Elford. The drift velocity of electrons in oxygen at 293 K. *Australian Journal of Physics*, 26(6):771–782, 1973.
- [15] Russell A. Nielsen. Absolute values of the electron drift velocity in nitrogen, helium, neon and argon. *Physical Review*, 50(10):950–954, 1936.
- [16] T. Brabec and F. Krausz. Intense few-cycle laser fields: Frontiers of nonlinear optics. *Reviews of Modern Physics*, 72(2):545 – 91, April 2000.
- [17] Thomas Brabec and Ferenc Krausz. Nonlinear optical pulse propagation in the single-cycle regime. *Phys. Rev. Lett.*, 78(17):3283–3285, April 1997.
- [18] A. Coua ron and A. Mysyrowicz. Femtosecond filamentation in transparent media. *Physics Reports*, 441(2-4):47 – 189, 2007.
- [19] Alexander L. Gaeta. Nonlinear propagation and continuum generation in microstructured optical fibers. *Opt. Lett.*, 27(11):924–926, June 2002.
- [20] N. Ak zбек, A. Iwasaki, A. Becker, M. Scalora, S.L. Chin, and C.M. Bowden. Third-harmonic generation and self-channeling in air using high-power femtosecond laser pulses. *Physical Review Letters*, 89(14):143901/1 – 4, September 2002.
- [21] G. Fibich. Self-focusing in the damped nonlinear Schr dinger equation. *SIAM J. Appl. Math.*, 61(5):1680 – 1705, 2001.
- [22] M. Mlejnek, M. Kolesik, E.M. Wright, and J.V. Moloney. Recurrent femtosecond pulse collapse in air due to plasma generation: numerical results. *Mathematics and Computers in Simulation*, 56(6):563 – 70, July 2001.
- [23] L. Berg , S. Skupin, R. Nuter, J. Kasperian, and J-P Wolf. Ultrashort filaments of light in weakly ionized, optically transparent media. *Rep. Prog. Phys.*, 70:1633–1713, 2007.
- [24] A.A. Zozulya, S.A. Diddams, A.G. Van Engen, and T.S. Clement. Propagation dynamics of intense femtosecond pulses: multiple splittings coalescence and continuum generation. *Physical Review Letters*, 82(7):1430 – 3, February 1999.
- [25] Todd A. Pitts, Mark R. Laine, Jens Schwarz, Patrick K. Rambo, Brenna M. Hautzenroeder, and David B. Karelitz. Numerical modeling considerations for an applied nonlinear schr dinger equation. *Applied Optics*, In preparation.
- [26] G. Strang. On the construction and comparison of difference schemes. *SIAM J. Numer. Anal.*, 5(3):506 – 517, September 1968.
- [27] Patrick K. Rambo, Briggs Atherton, Jens Schwarz, Todd A. Pitts, and Mark R. Laine. High energy laser switching. Technical report, Sandia National Laboratories, 2012.

- [28] Amnon Yariv. *Optical Electronics*. Oxford University Press, 4th edition, 1990.
- [29] Anthony E. Siegman. *Lasers*. University Science Books, May 1986.
- [30] Jean-Claude Diels and Wolfgang Rudolph. *Ultrashort Laser Pulse Phenomena: fundamentals, techniques, and applications on a femtosecond time scale*. Optics and Photonics. Academic Press, San Diego, first edition, 1996.
- [31] J. H. Marburger. Self-focusing: Theory. *Prog. Quant. Electr.*, 4:35–110, 1975.
- [32] M. Mlejnek, E. M. Wright, and J. V. Moloney. Femtosecond pulse propagation in Argon: A pressure dependence study. *Phys. Rev. E*, 58(4):4903–4910, Oct 1998.
- [33] Alex A. Zozulya, Scott A. Diddams, and Tracy S. Clement. Investigations of nonlinear femtosecond pulse propagation with the inclusion of Raman, shock, and third-order phase effects. *Phys. Rev. A*, 58(4):3303–3310, October 1998.
- [34] LSP was developed by ATK Mission Research Corporation with initial support from the Department of Energy SBIR program.
- [35] D. V. Rose, D. R. Welch, R. E. Clark, C. Thoma, W. R. Zimmerman, N. Bruner, P. K. Rambo, and B. W. Atherton. Towards a fully kinetic 3D electromagnetic particle-in-cell model of streamer formation and dynamics in high-pressure electronegative gases. *Physics of Plasmas (1994-present)*, 18(9):–, 2011.
- [36] K. Yoshida and H. Tagashira. Computer simulation of a nitrogen discharge at high overvoltages. *Journal of Physics D: Applied Physics*, 9(3):491, 1976.
- [37] S. H. Lin and H. Eyring. Calculation of the reaction cross section from a rate constant by the method of steepest-descent. *Proceedings of the National Academy of Sciences*, 68(2):402–405, 1971.
- [38] Donald Rapp and Donald D. Briglia. Total cross sections for ionization and attachment in gases by electron impact. II. Negative Ion formation. *The Journal of Chemical Physics*, 43(5):1480–1489, 1965.
- [39] M. M. Campbell. Iprop user’s manual: Postprocessor version. Technical report, 1991.
- [40] M. N. Shneider, A. M. Zheltikov, and R. B. Miles. *Tailoring the air plasma with a double laser pulse*, volume 18. AIP, 2011.
- [41] M. Danilov. Composition of a non-self-sustained discharge plasma in an N₂: O₂: H₂O mixture at atmospheric pressure. *Technical Physics*, 45(10):1251–1257, 2000.
- [42] I. A. Kossyi, A. Yu Kostinsky, A. A. Matveyev, and V. P. Silakov. Kinetic scheme of the non-equilibrium discharge in nitrogen-oxygen mixtures. *Plasma Sources Science and Technology*, 1(3):207, 1992.
- [43] C. K. Birdsall. Particle-in-cell charged-particle simulations, plus monte carlo collisions with neutral atoms, PIC-MCC. *Plasma Science, IEEE Transactions on*, 19(2):65–85, 1991.

- [44] K. Nanbu. Theory of cumulative small-angle collisions in plasmas. *Physical Review E*, 55(4):4642–4652, 1997.
- [45] J. Dutton. A survey of electron swarm data. *Journal of Physical and Chemical Reference Data*, 4(3):577–856, 1975.

DISTRIBUTION:

1 MS 0661	Brenna Hautzenroeder (electronic copy), 2623
1 MS 0968	Mark Laine (electronic copy), 5773
1 MS 0980	Todd Pitts (electronic copy), 5773
1 MS 1178	Deanna Jaramillo (electronic copy), 1657
1 MS 1178	Diego Lucero (electronic copy), 1657
1 MS 1178	Randall McKee (electronic copy), 1657
1 MS 1178	Kelly Seals (electronic copy), 1657
1 MS 1189	Dawn Flicker (electronic copy), 1640
1 MS 1191	John Porter (electronic copy), 1682
1 MS 1193	Daniel Sinars (electronic copy), 1680
1 MS 1194	Mark Savage (electronic copy), 1651
1 MS 1195	Gordon Leifeste (electronic copy), 1647
1 MS 1195	Randy Hickman (electronic copy), 1647
1 MS 1196	William Stygar (electronic copy), 1651
1 MS 1197	Jens Schwarz (electronic copy), 1682
1 MS 1218	Briggs Atherton (electronic copy), 5944
1 MS 0899	Technical Library, 9536 (electronic copy)

